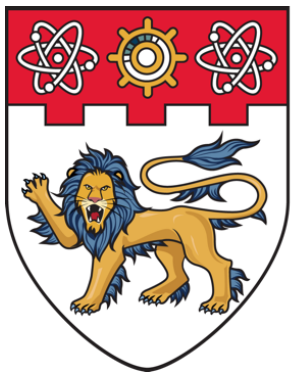

NANYANG TECHNOLOGICAL UNIVERSITY
SINGAPORE

CONFORMAL SKIN BIOELECTRODES

LI WENLONG

NTU INSTITUTE FOR HEALTH TECHNOLOGIES
INTERDISCIPLINARY GRADUATE PROGRAME

2021

CONFORMAL SKIN BIOELECTRODES

LI WENLONG

NTU INSTITUTE FOR HEALTH TECHNOLOGIES
INTERDISCIPLINARY GRADUATE PROGRAME

A thesis submitted to the Nanyang Technological University
in partial fulfilment of the requirement for the degree of
Doctor of Philosophy

2021

Statement of Originality

I hereby certify that the work embodied in this thesis is the result of original research, is free of plagiarised materials, and has not been submitted for a higher degree to any other University or Institution.

11 Aug 2021

. . . . . .
Date

Li Wenlong

. . . . . .
Li Wenlong

Supervisor Declaration Statement

I have reviewed the content and presentation style of this thesis and declare it is free of plagiarism and of sufficient grammatical clarity to be examined. To the best of my knowledge, the research and writing are those of the candidate except as acknowledged in the Author Attribution Statement. I confirm that the investigations were conducted in accord with the ethics policies and integrity standards of Nanyang Technological University and that the research data are presented honestly and without prejudice.

11 Aug 2021

. . . . . .

Date

. . . . . .

Prof. Chen Xiaodong

Authorship Attribution Statement

This thesis contains material from 1 paper published in the following peer-reviewed journal where I was the first author.

Chapter 6 is published as W. Li, N. Matsuhisa, Z. Liu, M. Wang, Y. Luo, P. Cai, G. Chen, F. Zhang, C. Li, Z. Liu, Z. Lv, W. Zhang, X. Chen. An on-demand plant-based actuator created using conformable electrodes. *Nature Electronics* **4**, 134-142 (2021). DOI: https://doi.org/10.1038/s41928-020-00530-4

The contributions of the co-authors are as follows:

- Prof Xiaodong Chen designed and supervised the project and revised the manuscript.
- I co-designed the project, conducted the experiments, and wrote the manuscript.
- Dr. Naoji Matsuhisa co-designed the project and co-wrote the manuscript.
- Dr. Zhiyuan Liu assisted with the conformable electrode design, fabrication, and characterization.
- Dr. Ming Wang and I synthesized and characterized the adhesive hydrogel.
- Ms. Yifei Luo and I prepared the cross-section of the plant and hydrogel for the optical microscope.
- Dr. Pingqiang Cai assisted with the fabrication of the conformable electrode.
- Dr. Geng Chen and I designed and performed the adhesive strength measurement of the electrode.
- Dr. Zhihua Liu designed and manufactured the LabVIEW-controlled motorized device.

- Dr. Zhisheng Lv and I fabricated the stretchable conductors.
- Dr. Wei Zhang performed the transmission electron microscopy investigation.

11 Aug 2021

. . . . . .

Date

Li Wenlong

. . . . . .

Li Wenlong

Abstract

Human beings leverage electrical signals to modulate their physiological activities. The electrical signals generated from neural cells, skeletal and cardiac muscle fibers can be transmitted through the human body and summed up as biopotential changes which can be measured from the skin. Depending on the generation source, the biopotential signals can be classified as the electrocardiogram (ECG, from the heart), electromyogram (EMG, from skeletal muscle), electroencephalogram (EEG, from brain neural activity), etc. The measurement of such biopotential signals presents a vital diagnostic tool in clinical practices.

The on-skin detection of biopotential signals depends on skin electrodes that transduce ionic current in human tissue into electronic current for external amplifier pickup. The commercial skin electrodes used in clinics are Ag/AgCl bulk metal electrodes with adhesive gel pasted on them. The Ag/AgCl-gel electrodes are fixed by medical tape on the skin. Such commercial skin electrodes present some critical shortcomings. One is that the bulky electrode cannot be stretched to accommodate the easily deformed skin, resulting in artifacts and hindrance of body movements during the measurement. The other is that the electrode relies on medical tape for fixation, which would cause discomfort or even skin trauma when peeling off the tape. In this regard, skin electrodes that are stretchable, soft, and comfortably adhesive are needed.

This thesis explores the novel skin bioelectrode solutions from a materials design perspective. Adhesive hydrogels that are highly stretchable (strain >300%), soft (Young's modulus < 100 kPa), and conductive are fabricated as skin-contacting layers for electrodes application. The optical, mechanical, and electrical properties can be further enriched by ionic additives. In addition, antimicrobial properties can be introduced into the hydrogel materials by a novel co-assembly of silk fibroin with Fmoc-protected amino acids. The antimicrobial hydrogel material for skin electrodes can effectively prevent skin inflammation and biofilm formation. Furthermore, ultrathin Au nanomesh material as an electronic conductor is chemically synthesized to transduce the ionic current in hydrogel

into the electronic current. The Au nanomesh, formed from intertwined Au nanowires, is electronically conductive and optically transparent. It can be transfer-printed on stretchable substrates and adhered to hydrogel to form skin electrodes. Lastly, to overcome the fast-drying issue of hydrogels as soft skin adhesive, a universal adhesive coating technique based on pressure-sensitive adhesive is also introduced for long-term comfort skin adhesion. Such a coating technique can be applied to most of the non-adhesive stretchable electrodes without deteriorating their electronic conductivity. These conformal skin electrodes allow high fidelity biopotential signal measurement from the skin without causing skin discomfort.

Lay Summary

Human skin is a fragile yet powerful organ. It can serve as a barrier between the human body with the harsh environment. Moreover, important physiological information can be transmitted from the skin and picked up by external electronic devices. Such physiological information can help doctors to diagnose a wide range of diseases. One of the information that can be vastly picked up from the skin is electrical signals. The electrical signals, generated from inside the human body, such as the heart, muscle, brain, can be transmitted to the skin because human tissue is ionically conductive. By listening to different electrical signals from different parts of the skin, the status of the heart, muscle, brain, and other physiological activity can be understood without any invasive implantable devices.

To pick up the electrical signals from the skin, skin electrodes are needed. As human tissue is ionically conductive, the current flown inside the human body is based on ionic current, while the external electronic devices are based on electronic conduction. Skin electrodes are a type of device that can transduce ionic current underneath the skin into an electronic current in external measuring electronic devices. Current skin electrodes used in the hospital are based on Ag/AgCl button plate with a gel paste on the plate. A circular medical tape is covered on the Ag/AgCl to fix it on the skin. These commercial electrodes have some drawbacks. The Ag/AgCl button plate is not stretchable, any deformation of skin would cause noise in the signal, as such, patients need to be static during the measurement. Moreover, peeling off the medical tape after the measurement is painful, sometimes even causes injury to the skin. For these reasons, novel skin electrodes that are thin and lightweight can be conformally adhered to and peeled off from skin are needed.

This thesis solves the issues in skin electrodes from materials innovation. Adhesive hydrogels, a polymer network that contains more than 90% of water, are chemically synthesized. This adhesive hydrogel is soft, stretchable, and gently adhesive. It can be attached to and peeled off from the skin easily. The hydrogel is also ionically conductive, it can sense electrical signals from the skin. To transduce the ionic current in the hydrogel,

an ultrathin Au nanomesh is synthesized and transferred to a stretchable substrate. The Au nanomesh is transparent and electronic conductive, when adhered to hydrogel, it can work with the adhesive hydrogel as a skin electrode to measure electrical signals from the skin. Moreover, when a patch is attached to the skin for a long time, bacteria colonies can appear, causing skin inflammation. An antimicrobial hydrogel is further synthesized to prevent skin inflammation and disrupt biofilm formation on the skin. Lastly, to make sure many other non-adhesive stretchable electrodes can directly adhere to the skin, a pressure-sensitive adhesive coating technique is invented. The adhesive coating is convenient and can be applied on many different electrode material surfaces. These adhesive and stretchable materials allow the fabrication of conformal skin electrodes and the measurement of high-quality signals.

Acknowledgements

This dissertation would not have been possible without funding from NTU Institute for Health Technologies, Interdisciplinary Graduate Program, National Research Foundation, and Singapore Ministry of Education for research grants.

Special thanks are conveyed to my research project supervisors Professor Chen Xiaodong for their continual guidance and support. I also appreciate the valuable advice from my Thesis Advisory Committee (TAC) members, my co-supervisor Prof Chen Peng, and my mentor Prof Theodoros Kofidis.

This thesis relied on assistance from Dr. Liu Zhiyuan, Dr. Naoji Matsuhisa, Dr. Wang Ming, Dr. Luo Yifei, Dr. Cai Pingqiang, Dr. Gen Geng, Dr. Zhang Feilong, Dr. Li Chengcheng, Dr. Liu Zhihua, Dr. Lv Zhisheng, Dr. Zhang Wei. I was also fortunate for the opportunity to cooperate with Professor Chua Nam Hai in Temasek Life Sciences Laboratory, and his research fellows Dr. Ohama Naohiko and Dr. Huang Chung Hao.

I am thankful to Mr. Gan Zi Li, Mr. Wilson Lim, Mr. Patrick Lai, and all the technicians in MSE labs, who provided numerous help for facilities training.

I was fortunate to be accompanied by supportive group members in Prof Chen's group. Special thanks are conveyed to Dr. Tang Yuxin, Dr. Zhang Yanyan, Dr. Liu Zhiyuan, Dr. Jiang Ying, Dr. Zhang Feilong, Ms. Yi Junqi, Dr. Wang Ming, Dr. Wan Changjin.

Lastly, I am very grateful to my family and friends for their accompany and encouragement during my Ph.D. study.

Table of Contents

Table Captions

Figure Captions

Figure 1.1 The biological origin of biopotential in the human body. (a) Muscular cells (including skeletal muscle, smooth muscle, and cardiac muscle) and neurons are excitable cells that can generate AP. (b) The cell membrane structure that excitable for AP generation. The membrane potential is maintained by the active transport of sodium and potassium pumps. A concentration gradient of sodium and potassium between the extracellular and intracellular space defines the resting potential. Upon a stimulus exceeding the threshold, the permeability of the ion channels dramatically changes, altering the membrane potential, forming AP. (c) The waveform of AP. AP starts from its resting potential (around -70 mV), with depolarization and subsequent repolarization. The depolarization is due to increased inflow Na^+ permeability and repolarization is due to increased outflow K^+ permeability. (d) Hodgkin-Huxley model to simulate the AP waveform. The cell membrane is treated as an equal circuit of membrane capacitance, variable Na^+ current, K^+ current, and leakage current.

Figure 2.2 Electrical signals from different parts of the heart and the resultant ECG signal. ECG signal usually includes a preceding P wave, a QRS complex wave, and a T wave. The amplitude of the ECG signal is usually around 1 – 3 mV.

Figure 2.3 The surface biopotential of ECG. Left, Schematic of surface ECG measurement using a 3-lead method. Electrodes can be placed on the right arm, left arm, and left leg of the human body, the potential difference between these three electrodes can be measured. Right, Equivalent circuit diagram of the ECG measurement. The heart can be regarded as an equivalent cardiac generator. R1 and R2 represent the tissue resistance from the heart to the measuring point A and B. Φ_A and Φ_B represent the potential at measuring point A and B. Φ_{AB} represents the potential difference between the two points.

Figure 2.4 Electrical activities of the brain. (a) The brain's electrical activity is a multilevel process at different time and space scales. The single neuron at the microscopic scale generates synaptic currents and spike potentials. The local network of thousands of neurons working together generates local field potentials (LFPs). When millions of neurons

work at a synchronized pace, the EEG signal is formed by the summation of the millions of neurons. (b) Different wavebands of EEG signals. The main EEG signal waves classified at different frequencies include delta, theta, alpha, beta, and gamma waves.

Figure 2.5 Motor unit structure and EMG signal of skeletal muscle. Skeletal muscle is composed of muscle fibers that can be stretched or rested. The muscle fibers are controlled by Central Nervous System (CNS) in the spinal cord. Motor neurons connect with muscle fiber through the motor unit. Each motor unit connects with several interspersed muscle fibers. During the muscle activation, motor neurons will fire excitation AP to transmit through the motor unit to muscle fibers. The muscle fibers, when activated, will contract. Activated muscle fibers also emit local field AP. Each muscle fiber AP acts as distributed current source, surrounded by a volume conductor. When measuring potential change on the surface of volume conductor (skin), surface EMG is measured which is the summation of many muscle fibers.

Figure 2.6 Different amplifier circuits for biopotential measurement. (a) An op-amp amplifier with non-inverting and inverting inputs and an output. (b) An inverting amplifier with negative feedback and non-inverting input grounded. (c) A voltage follower amplifier with negative feedback and grounded non-inverting input. (d) An instrumentation amplifier (three-op-amp differential amplifier) with high input impedance and high CMRR.

Figure 2.7 Mechanism of electric field coupling of the power line on ECG measurement. There are three ways that the power line (230V and 50 Hz) can interfere with ECG measurement. First, the electric field of the power line can capacitively couple with the human body, inducing a capacitive current flow (i_{db}) in the human body. The current can flow into the measured loop, causing signal noises. Similarly, the power line can also capacitively couple with the lead wires, adding more currents (i_{d1} and i_{d2}) into the measured loop.

Figure 2.8 The skin anatomy and structure. Skin is a multilayer protective barrier with glands and hair appendages.

Figure 2.9 Equivalent circuit of electrode and skin interface. Electrode and electrolyte gel is placed on the skin. Two interfaces are important, one is the electrode-electrolyte interface, and the other is the electrolyte-epidermis interface. The electrode-electrolyte interface can be modeled as a DC battery (E_{dc}) and a capacitor (C_d) and resistor (R_d) in parallel. E_{dc} is due to the polarization of the electrode, around 10 mV. C_d is due to the double layer capacitor and absorption capacitor, and R_d is due to the charge transfer resistance. The parallel C_d and R_d represent electrode impedance, which is usually around 1 kΩ. The gel itself has an Ohmic resistance R_s. The interface between the electrolyte and epidermis forms another DC battery (E_{se}). This is because the stratum corneum acts as a semipermeable membrane separating different ion concentrations. Sweat glands and ducts may also contribute extra components. The electrolyte-skin interface contributes the highest impedance in the system (around 300 kΩ). The skin tissue beneath the stratum corneum can be simplified as a passive resistor with a value around 100 Ω.

Figure 2.10 The desired on-skin electrodes properties for biopotential signal measurements. The electrodes need to be conductive for signal transduction, stretchable for skin deformation, soft for skin modulus match, adhesive for intact skin attachment, breathable for skin gas exchange, and biocompatible without skin damage.

Figure 2.11 Structures for stretchable conductors. The state-of-the-art structural design can be classified as serpentine structure, mesh structure, and microcrack nanofilm structure.

Figure 2.12 Materials design of stretchable, conductive, and soft on-skin bioelectrodes. Hydrogel, a crosslinked polymer containing more than 90% of water, is a widely used ionic conductor in contact with the skin. Metal nanofilms that are stretchable can also be directly applied to the skin as bioelectrodes. Protein-based materials (silk fibroin) crosslinked by ions can work as a biocompatible ionic conductor for on-skin bioelectrodes.

Figure 2.13 Electrode array technologies. The array technologies include active-matrix array or passive matrix. Active-matrix array requires one transistor as a switch for each electrode, it reduces the number of wirings. Passive-matrix requires one wire for each electrode, it is easier to develop but the number of wiring increases with electrode numbers.

Figure 2.14 Flexible electrode array devices. The active-matrix device can have more than one transistor for more complicated control over each electrode. Due to complexity, the electrode is only flexible and difficult to make stretchable. The passive-matrix device requires a conductive pattern and can be made very soft and stretchable.

Figure 3.1 Schematic of a hydrogel and its network structure. Hydrogels can be prepared in a bulk or thin-film form. It is composed of 3D interconnected polymer chains. The polymer chains are hydrophilic in that they can contain a large amount of water (more than 90% of its weight). The polymer chains are connected by chemical crosslinking (covalent bond) or physically crosslinking (non-covalent bond).

Figure 3.2 Chemical recipes used in the synthesizing of the adhesive polyacrylic acid hydrogel. Acrylic acid is a monomer that will undergo free radical polymerization to form polymers. Potassium persulfate is a thermal initiator to initiate free radical polymerization. N,N'-Methylenebis(acrylamide) is the cross-linker that forms covalent bonds with polyacrylic acid polymer chains. N,N,N',N'-Tetramethylethylenediamine is the accelerator to increase the reaction rate of the polymerization. The final polyacrylic acid hydrogel is an interconnected polyacrylic acid polymer network.

Figure 3.3 Schematic of Au nanomesh synthesis. Au nanoparticles are firstly obtained in an aqueous solution by reducing $HAuCl_4$ using $NaBH_4$. Then adding toluene and vigorous agitation result in the formation of Au nanowires and a layer of mesh on the toluene-water interface.

Figure 3.4 Working principle of electrochemical impedance spectroscopy (EIS). (a) Setup of an electrochemical system. The measurement needs three electrodes: working electrode (WE), reference electrode (RE), and counter electrode (CE). A current stimulus is given between CE and RE, while the potential signal is measured between RE and WE. (b) Schematic of a perturbation signal. It can be a current signal or a voltage signal. It is a continuous sine waveform with changing frequencies. (c) Schematic of a relationship between perturbation voltage signal and response current signal. The perturbation signal needs to be located at a linear region. (d) Nyquist plot and Bode plot of the measured EIS result. (e) equivalent circuit model to interpret the resultant Nyquist plot or Bode plot.

Figure 3.5 Three configurations of skin bioelectrode characterization in EIS system. The measurement is conducted in a two-electrode system. The electronic conductive of an Au-PDMS electrode can be characterized by measuring impedance from its two ends (top left). The Au-PDMS electrode with hydrogel interface can be characterized by a sandwich structure (top right), where each end of the electrode is connected to the electrochemical system. The electrode-skin interface can be characterized by measuring the impedance of two electrodes on the skin (bottom).

Figure 3.6 Photograph of mechanical tests of hydrogels. The elastic hydrogel can be characterized by a stress-strain test (left). The adhesiveness of the hydrogel can be characterized by a 90-degree peeling test. It is noted that due to the risk of directly measuring on the skin under a mechanical tester, the study surface can be replaced by a leaf surface.

Figure 3.7 Schematic of the working principle of UV-vis spectrophotometry. The spectrophotometry includes a light source to emit light from UV to visible range, a wavelength selector to allow selecting light in different wavelengths. The selected light is emitted on the sample. The transmitted light to captured by the detector and the signal is further processed and visualized in a computer.

Figure 3.8 Schematic showing the electrical measurement of a thin film sheet resistance. Two measuring electrodes are needed. The measured surface width should be equal to its length to eliminate the effect of sample geometry.

Figure 3.9 Schematic of the mechanical and electrical characterization of the Au nanomesh. The Au nanomesh conductor is not a freestanding film, it needs to be transferred onto a PDMS elastomer substrate to allow stretching under a mechanical tester. The stretch is given at a constant strain rate. The resistance of the Au nanomesh is measured by a digital multimeter at the same time.

Figure 3.10 Schematic of the working principle of SEM and TEM. Each piece of equipment requires an electron gun and a series of electromagnetic lenses to focus and

control the electron beam. A series of detectors are placed near the sample to collect different signals such as secondary electrons or X-rays.

Figure 3.11 Schematic showing the 12-lead ECG system. The 12 leads form two planes of the heart. One is a vertical plane including 6 leads: Lead I, Lead II, Lead III, aVR, aVL, aVF. The other is a horizontal plane, including 6 leads: V1, V2, V3, V4, V5, and V6.

Figure 3.12 The three-electrode system to measure the 12-lead ECG results. This system relies on an Analog Devices chip AD8232 with a right leg driver (RLD). This three-electrode system can minimize the measurement electrodes and make it easier to get 12-lead ECG results.

Figure 3.13 The schematic and photo of the customized flexible PCB for measuring biopotential signals. The flexible PCB includes an amplifier and a Bluetooth microcontroller. The flexible PCB is miniaturized (as small as 1.8 cm) and is wireless. It can be used to measure ECG and EMG.

Figure 4.1 Schematic of the fabrication process of PAA hydrogel on PDMS substrate. The PDMS substrate is first coated with acrylic acid monomer to increase bonding between the hydrogel and PDMS. The PAA hydrogel is fabricated inside a PDMS mold on the PDMS substrate.

Figure 4.2 Contact angle of PDMS surface after coated by AA monomer. The contact angle decreased from 112 – 119 degrees to 61 – 69 degrees after the AA coating, indicating the hydrophilic effect of the AA coating.

Figure 4.3 The PAA hydrogel on PDMS substrate. (a) Schematic of the PAA hydrogel on PDMS substrate. (b) Photograph of the hydrogel-PDMS under stretching. (c) Photograph of the hydrogel-PDMS attached on a plant leaf, showing its transparency and conformability.

Figure 4.4 Impedance of the PAA hydrogel with different ionic additives. (a) Nyquist plot of the hydrogel with different ionic additives. (b) Bode plot of the hydrogel with different ionic additives. (c) Capacitive and resistive impedance comparison of the hydrogel with different ionic additives. (d) Schematic of the impedance measurement. The

hydrogel sample has a dimension of 30 x 10 x 1.5 mm. The ionic additive concentration is 0.5 M. The EIS has a perturbation voltage of 30 mV from 1 Hz to 1 MHz. Each ionic additive was measured with 4 repeated samples.

Figure 4.5 Optical transmittance of the hydrogel with different ionic additives. (a) The UV-vis transmittance spectroscopy of the hydrogel with different ionic additives. (b) The transmittance at 440 nm and 660 nm of the hydrogel with different ionic additives. The hydrogel electrode dimension is 40 mm x 15 mm x 2 mm, and the ionic concentration of hydrogel precursor solution is 0.5 M. Student's t-test: n.s., not significant, * $p < 0.05$, ** $p < 0.005$ ($n = 3$).

Figure 4.6 Adhesive strength of the hydrogel with different ionic additives. (a) the adhesive strength measured from a mechanical tester. (b) the adhesive strength of hydrogel with different ionic additives. The hydrogel electrode dimension is 40 mm x 15 mm x 2 mm and ionic concentration is 0.5 M, 3M VHB tape is used as hard baking, healthy fresh leaf of lipstick vine as the surface. Student's t-test: * $p < 0.01$, ** $p < 0.001$, *** $p < 0.0005$, $n = 4$.

Figure 4.7 Impedance measurement of the hydrogel with KCl additive at different concentrations. (a) The Nyquist plot. (b) The Bode plot. The hydrogel electrode dimension is 30 mm x 10 mm x 1.5 mm.

Figure 4.8 Optical transmittance of the hydrogel with KCl additive at different concentrations. (a) The UV-vis spectroscopy of the hydrogel. (b) The transmittance at 440 nm and 660 nm of the hydrogel with different KCl concentrations. Hydrogel electrode area: 40 x 15 x 2 mm. Student's t-test: n.s. not significant, * $p < 0.05$, $n = 3$.

Figure 4.9 Adhesive strength of the hydrogel with KCl additive at different concentrations. (a) the adhesive strength measured from a mechanical tester. (b) the adhesive strength of hydrogel with different ionic additives. Hydrogel electrode area is 40 x 15 x 2 mm, KCl concentration in precursor solution is 0.5 M, 1 M, 2 M. The peeling off rate is 1 mm/s. Student's t-test: n.s. not significant, * $p < 0.005$, $n = 4$.

Figure 4.10 Mechanical stress-strain test of the hydrogel. The hydrogel is prepared in a film form with a dimension of 40 mm x 15 mm x 2 mm. KCl concentration used is 1 M. The stress-strain curve is measured in a mechanical tester MTS C42 with a 50 N load cell. The strain rate is set to 0.2 mm s^{-1}.

Figure 4.11 The synthesis scheme of Au nanomesh. Au nanomesh was synthesized from a wet-chemistry method. $NaBH_4$ as a reductant was added to the $HAuCl_4$ precursor solution. Au nanoparticle was formed by the drop-by-drop adding of $NaBH_4$. Toluene was added to create a water-toluene interface for the Au nanoparticle assembly. After stirring, Au nanoparticle self-assembled into Au nanomesh, forming a thin layer of film at the water-toluene interface. After careful removal of Au nanomesh by a pipette, the Au nanomesh film was ready for transfer printing. A homemade PDMS stamp was used to transfer the Au nanomesh. By carefully attaching PDMS film onto Au nanomesh film for around 30 s, Au nanomesh could be transferred onto the PDMS film.

Figure 4.12 UV-vis spectrum of Au nanomesh solution. The Au nanoparticle solution shows a strong surface plasmon resonance (SPR) peak at 529 nm. SPR is the transverse oscillations of particle surface electrons on interaction with the light of a suitable wavelength. Gold colloids usually have an absorption peak in the visible light range. Here, the SPR peak of 529 nm indicates Au nanoparticle size of 15 nm.9 Inset: photograph of Au nanoparticle solution in Corning tube showing red-wine color.

Figure 4.13 SEM image of Au nanomesh synthesized by different precursor ratios. The mesh-like nanostructure was maintained in different ratios. The nanowires interconnect for high electrical conductivity, while the hollow areas allow high transparency and gas exchange. Due to its best optical and electrical properties, 4.5 mg/mg was selected as the synthesis condition for all the applications. Scale bars, 100 nm.

Figure 4.14 Optimization of the Au nanomesh film under different HAuCl4/NaBH4 weight ratio conditions. 4.5 mg/mg shows the highest transmittance and smallest square resistance.

Figure 4.15 A simulation of the electrical potential distribution in an Au nanomesh film. The distribution is uniform in the Au nanomesh despite its irregular hollow structure, indicating the minimized effects of the hollow structure on its electrical property uniformity. The simulation was conducted in Comsol 5.5.

Figure 4.16 TEM characterization of Au nanomesh. (a) Au nanomesh as lifted from the water-toluene interface. The Au nanomesh is formed by interconnected tortuous nanowire fragments. The interconnected nanowires show a diameter of around 15 - 20 nm, agreeing with UV-vis results. (b) A high-resolution TEM image shows the grain boundary between Au nanoparticle junctions. The coalescence of Au nanoparticles is the primary mechanism of Au nanomesh formation7. (c) The crystal lattice interplanar spacing of Au nanomesh shows a d-spacing equal to 0.236 nm, corresponding to the interspacing distance of Au face-centered cubic (111) plane10, 11. (d) SAED (selected area electron diffraction) image of the Au nanomesh, showing diffraction rings corresponding to (111), (200), (220), (311) of face-centered cubic Au polycrystalline nanocrystals.

Figure 4.17 Transparency of Au nanomesh-PDMS film. (a) Photograph of Au nanomesh on PDMS film (2 cm x 2 cm) showing its transparency. The Au nanomesh-PDMS film is indicated by a white dashed box. (b) UV-vis spectrum of the Au nanomesh-PDMS film. Plants are responsive to blue (~450 nm) and red (~650 nm) light for photoactivity. The film shows 69% transmittance at the 450-nm wavelength and 71% transmittance at the 650-nm wavelength, indicating the film is transparent enough for light absorption of plants. (c) FESEM image of the Au nanomesh on PDMS film reflects the origin of its transparency from a nanostructure perspective. The porous area of the nanomesh allows effective light transmittance of the film. In addition, the conductivity of the film comes from its intertwined 2D network. The tortuous Au nanowires provide the film with superior stretchability.

Figure 4.18 Electrical characteristics of Au nanomesh-PDMS film. (a) Cycling test of the Au nanomesh-PDMS film. The film was cycled at a 50% strain for 200 cycles, showing that the electrode is mechanically and electrically stable during the cycling test. It is also noted that during cycling the highest resistance at maximum strain is reduced. This

phenomenon is commonly seen in stretchable Au electrodes, which is possibly due to the cold-welding effect of Au during mechanical strain. (b) Stretchability test of Au nanomesh-PDMS film. The film shows good electrical insensitivity upon stretching. R/R_0 keeps at 10 at a strain of 120%, and the film keeps conductive until 135%.

Figure 4.19 Interfacial current conduction between the adhesive hydrogel and Au nanomesh interface measured by EIS. As a comparison, CNT, AgNW, and Al foil were also tested as control experiments. All the sizes of electrode films were kept at 2 cm x 1 cm, the size of hydrogel was kept at 1 cm x 1 cm. The device was configured into an electrode-hydrogel-electrode symmetric sandwich structure (as shown in the top schematic). In such a configuration, the total conductance of such a sandwich structure comes from the conductance of two electrode film layers, one hydrogel layer, and two electrode-hydrogel interfaces. To make sure only the conductance of the electrode-hydrogel interface is comparable between different electrode materials, the conductance of different electrode films was kept the same (right y-axis). Au nanomesh film shows the highest admittance with adhesive hydrogel compared with CNT, AgNW, and Al foil (left y-axis), which is due to its nanomesh-like structure and relatively large contacting area with hydrogel. Top: Schematic of device configuration.

Figure 5.1 Fabrication process of silk fibroin solution. The process roughly includes three steps: the first step is degumming to remove the surface sericin layer of silk fiber and the second step is to dissolve silk firoin core fiber into LiBr aqueous solution, and the last step is dialysis to remove excessive ions from the silk fibroin solution.

Figure 5.2 Preparation scheme of the co-assembly of silk fibroin and Fmoc-protected amino acids.

Figure 5.3 Agar spreading plate method to count bacteria colony-forming units in ImageJ.

Figure 5.4 Chemical structures of the 12 types of Fmoc-protected amino acids.

Figure 5.5 Photograph images of assembled silk hydrogel by Fmoc-protected amino acids. Each vial tube was filled with 500 μL silk solution and 10 mg Fmoc-protected amino

acids. (a) A series of vial inversion methods to verify the gelation of silk with different types of Fmoc-protected amino acids. From 1 to 12, 1: Fmoc-Ile-OH, 2: Fmoc-Phe-OH, 3: Fmoc-Lys(Boc)-OH, 4: Fmoc-Thr(tBu)-OH, 5: Fmoc-Asp(OtBu)-OH, 6: Fmoc-Leu-OH, 7: Fmoc-Glu(OtBu)-OH, 8: Fmoc-Met-OH, 9: Fmoc-Thr(tBu)-OH, 10: Fmoc-Gly-OH, 11: Fmoc-Ala-OH, 12: Fmoc-Ser(tBu)-OH. (b) Vial inversion method to verify the gelation of silk by Fmoc-Leu-OH with different weights. 2 mg of Fmoc-Leu-OH would not be able to promote the formation of silk, while a weight of 5 mg to 40 mg can promote the formation of silk. (c) Assembled silk hydrogel from 1 mL silk solution in a 30 mm petri dish, the thin layer of hydrogel has a transparent appearance.

Figure 5.6 UV-vis spectrum of assembled hydrogel prepared inside a petri dish. As the weight ratio of Fmoc-Leu-OH over silk fibroin increases, its transparency decreases. The silk fibroin hydrogel was prepared from a 1 mL silk fibroin solution.

Figure 5.7 SEM images of silk fibroin hydrogel prepared from different Fmoc-Leu-OH weight ratios. The hydrogel samples were first lyophilized, and vacuum sputtered a gold layer for SEM imaging. Only Silk and Silk-Fmoc-L (8%) cannot form a hydrogel, Silk-Fmoc-L (40%) formed the most robust structure. Silk-Fmoc-L (80%), Silk-Fmoc-L (120%), Silk-Fmoc-L (180%) showed crushed hydrogel fragments.

Figure 5.8 FTIR-ATR spectrum of Silk-Fmoc-L samples from different silk and Fmoc-L weight ratios. Specifically, three peak structures were analyzed in detail. These three peak structures include Amide I C=O stretching (1630 – 1650 cm^{-1}), Amide II secondary N-H bending (1540 – 1520 cm^{-1}), and Amide III C-N stretching (1270 – 1230 cm^{-1}). As the Fmoc-L weight ratio increases, the β-sheet conformation is also increased, and random coil conformation is decreased.

Figure 5.9 Agar plate spreading method to verify the bacteria-killing efficiency of Silk-Fmoc-L hydrogel. B. subtilis was used as a model bacterium in this experiment. Bacteria solutions were first treated with Silk-Fmoc-L hydrogel and then incubated on agar plate, the colony-forming units (CFU) are counted. Compared with control bacteria which is incubated without hydrogel, the hydrogel treated bacteria agar plate showed a very clean surface, without any observable bacteria colonies, the control plate showed rather plenty

of bacteria colonies, corresponding to a live bacterial concentration of 8.13 x 10^8 CFU mL^{-1}.

Figure 5.10 LIVE/DEAD bacteria staining of bacteria before and after hydrogel treatment. SYTO 9 staining has a green fluorescence while PI staining has a red-yellow fluorescence. SYTO 9 stains both live and dead bacteria and PI stains only dead bacteria. The bacteria after hydrogel treatment showed almost all dead fluorescence while control bacteria showed almost all live fluorescence, indicating that the hydrogel is very effective in killing bacteria.

Figure 5.11 Chemical structure of the reagents and products during the hydrogel synthesis. Acrylamide was used as the monomer to undergo polymerization, potassium persulfate was added as thermal initiator, N,N,N',N'-tetremethylethylenediamine was added as crosslinker. The formed PAAm is a 3D network that can withstand more than 90% of water.

Figure 5.12 Photograph images of the obtained Silk-PAAm hydrogel. The weight ratio of silk to water is 5% while the weight ratio of AAm to water is 20%. The hydrogel showed good mechanical properties as reflected by stretching. It is also wearable on skin with moderate adhesiveness. After water treatment, the hydrogel has a semi-transparent appearance.

Figure 5.13 Light microscope images Silk-AAm hydrogel with different AAm weight ratios at 5X, 10X, and 20X. Other preparation parameters of the hydrogels were kept the same. Very interestingly, a hydrogel with 13% AAm monomer showed a smooth surface feature without any crack formation, indicating the formation infiltration of polyacrylamide network and silk fibroin network. However, Silk-AAm hydrogel with 20% AAm monomer and 27% monomer showed dense surface crack, which is formed due to a separated rigid silk layer on the top of the hydrogel.

Figure 5.14 Light microscope images of control hydrogel made of pure AAm. With the variation of AAm weight ratio, there is no surface crack formation, this indicates that the crack formed in Silk-AAm is due to the presence of silk fibroin.

Figure 5.15 Mechanical stress-strain cure (a) and Young's modulus (b) of hydrogels made from different AAm weight ratios. The break elongation Silk-AAm is smaller compared to that without silk, while Young's modulus of Silk-AAm hydrogel is larger than that without silk. This indicates that there is an obvious hardening effect of the hydrogel by the silk.

Figure 5.16 FTIR-ATR spectrum of Silk-AAm with different comparing samples. There is an obvious presence of β-sheet conformation in the Silk-AAm hydrogel, indicating that a physical crosslink of β-sheet of silk fibroin was formed in the Silk-AAm hydrogel.

Figure 5.17 Fluorescence spectrum of Silk-AAm hydrogel when loaded with Fmoc-L. The emission peak of 328 nm is due to the fluorenyl group in Fmoc-L, while the peak at 371 nm is due to the excimer emission. This indicates that the Fmoc-L was integrated with Silk-AAm hydrogel.

Figure 5.18 SEM images of Silk-AAm (top) and Silk-AAm-Fmoc-L (bottom). In Silk-AAm there showed a typical porous structure of hydrogel. Interestingly, in Silk-AAm-Fmoc-L there showed a layer of nanorods grown on the surface of the hydrogel structure. These nanorods are probably due to the precipitation of Fmoc-L. The formation mechanism requires further study to justify.

Figure 6.1 Photograph of PSA coated Au nanofilm on PDMS attached on human skin. No-PSA-coated Au nanofilm shows difficulties in covering hairy skin, while PSA-coated film can conformably cover hair skin. Skin wrinkles and fingerprints can form on the Au nanofilm.

Figure 6.2 Impedance measurement of Au nanofilm-SEBS electrodes on the skin. (a) The Bode plot of the commercial Ag/AgCl-gel electrodes, tape-fixed Au nanofilm-SEBS electrodes, and PSA-coated Au nanofilm-SEBS electrodes. (b) The phase angle of the commercial Ag/AgCl-gel electrodes, tape-fixed Au nanofilm-SEBS electrodes, and PSA-coated Au nanofilm-SEBS electrodes.

Figure 6.3 Impedance measurement of Au nanofilm-PDMS electrodes on the skin. (a) The Bode plot of the commercial Ag/AgCl-gel electrodes, tape-fixed Au nanofilm-PDMS

Abbreviations

AA	Acrylic acid
AAm	acrylamide
ADC	Analog-to-digital converter
AgNW	Silver nanowire
AP	Action potential
ATR	Attenuated Total Reflection
AV	atrioventricular
aVF	augmented Vector Feet
aVL	augmented Vector Left
aVR	augmented Vector Right
CE	Counter electrode
CFU	Colony forming unit
CMRR	Common Mode Rejection Ratio
CNS	Central nervous system
DC	Direct current
ECG	Electrocardiogram
EEG	Electroencephalogram
EIS	Electrochemical impedance spectroscopy
EMG	Electromyogram
LA	Left arm
LB	Luria-Bertani
LFP	Local field potential
LL	Left leg
Op-amp	Operational amplifier
PDMS	Polydimethylsiloxane
PAA	Polyacrylic acid
PAAm	Polyacrylamide
PCB	Printed circuit board
PET	Polyethylene terephthalate

PSA	Pressure sensitive adhesive
PVA	polyvinyl alcohol
RA	Right arm
RE	Reference electrode
RL	Right leg
RLD	Right leg driver
SA	Sinoatrial
SEBS	Styrene-ethylene-butylene-styrene
SEM	Scanning electron microscopy
SoC	System on Chip
SPR	Surface plasmon resonance
TEM	Transmission electron microscopy
WCT	Wilson’s Central Terminal
WE	Working electrode

Chapter 1

Introduction

This chapter contextualizes the thesis by giving a brief background in the biopotential signals of the human body and the application of on-skin bioelectrodes for the measurement of biopotentials. The research hypothesis is to develop skin conformal materials and stretchable conductors as skin electrodes. This chapter also illustrates the overview of the projects conducted in this thesis. The outcome of this thesis is also provided.

1.1 Hypothesis/Problem Statement

The biopotential vital signals, including electrocardiogram (ECG), electromyogram (EMG), electroencephalogram (EEG), etc. are important parameters in clinical diagnosis of the human body[1]. Due to the volume conductor property of the human body, the biopotential vital signals can be measured on the skin[2], providing a non-invasive and convenient way for clinical and personal healthcare application. However, the on-skin detection of biopotential relies on the skin electrodes[3], which presents some challenges from materials perspectives.

Conventional electrodes for on-skin biopotential signal measurement depend on an Ag/AgCl bulk metal electrode and an adhesive gel paste covered by a medical tape as a fixation on the skin[4]. Such commercial electrodes have some disadvantages. One is that the skin is stretchable, but the electrode is not stretchable, which would hinder the free deformation of the skin with the electrodes on it. The other is that the medical tape has a strong adhesion on the skin, which would cause discomfort or even skin trauma when peeling of the electrode[5]. In this regard, some conformal and stretchable thin-film skin electrodes have been developed for better skin contact while ensuring good signal measurement[6]. Such conformal and stretchable electrodes are usually made of a stretchable conductor on a stretchable elastomer substrate. However, such electrodes and not intrinsically adhesive on the skin. To apply on skin, medical tapes are still needed for the fixation.

The hypothesis in this thesis is to develop adhesive and conductive skin interfacial layer for stretchable and conformal skin electrodes. The first strategy is to develop adhesive hydrogel with modulable conductivity, transparency, and adhesiveness properties. Further efforts are also made to realize the antimicrobial property of the hydrogel material to avoid inflammation or biofilm formation on the skin. The second strategy is to develop a non-conductive but adhesive coating technique, such non-conductive adhesive when coated very thin, only occupies some sparse areas on the electrode for adhesion, while the unoccupied areas can be used for signal transduction. Some stretchable conductors are

developed in this thesis, including transparent chemically synthesized Au nanomesh conductor, Au nanofilm on PDMS (polydimethylsiloxane) substrate, Au nanofilm on SEBS (styrene-ethylene-butylene-styrene) substrate, and silver nanowire (AgNW) on PDMS substrate. Such adhesive and conductive materials strategies are expected to realize conformal skin bioelectrodes that can be directly applied in the biopotential signal measurement.

1.2 Objectives and Scope

In testing the hypotheses stated above, the following objectives are to be accomplished by the end of the study:

1. To design and fabricate adhesive hydrogels material for skin interface layer, with tunable adhesive, conductive, optical, and mechanical properties.

2. To further design novel antimicrobial properties of the adhesive hydrogels which can be used to avoid skin inflammation and biofilm formation.

3. To design and fabricate stretchable conductors with tunable thickness, conductivity, stretchability.

4. To integrate the developed materials for on-skin conformal electrodes, and further integrate with wearable and wireless electronics to realize conformal on-skin biopotential measurement.

To achieve these objectives, the following experiments and analyses were conducted:

1. Synthesis of adhesive hydrogel, characterization, and optimization of the adhesive hydrogel with tunable mechanical and electrical properties for on-skin electrode applications.

2. Fabrication of stretchable conductors as electronic transduction layer with the hydrogel, including chemically synthesized Au nanomesh-PDMS conductor, Au-PDMS conductor, Au-SEBS conductor, and AgNW-PDMS conductor.

3. Characterization of stretchable conductors with the understanding of microscopic, electrical, and mechanical properties.

4. Develop a coating protocol for an ultrathin coating of pressure-sensitive adhesive (PSA) on different stretchable conductors.

5. Development of miniaturized, wirelessly, and flexible biopotential signal measurement platform.

6. Verification of the adhesive and conformal electrodes to measure ECG and EMG signals.

1.3 Dissertation Overview

The thesis consists of the following 7 chapters:

Chapter 1 provides a rationale for the research and outlines the goals and scope. The thesis describes and validates the design and fabrication of comprehensive skin bioelectrode materials systems for conformal biopotential signal measurement.

Chapter 2 reviews the literature concerning the fundamentals of biopotential signals in the human body, the measuring techniques related to the biopotential signal measurement, the status in the electrode development for on-skin application, including both commercially available ones and in the research field, and the background of the material related to skin electrodes such as hydrogels and stretchable conductors.

Chapter 3 discusses the principles underlying the synthesis and characterization of the materials. The rationale for the selection of the material and method are discussed.

Principles of main characterization techniques are also elaborated.

Chapter 4 elaborates the design, fabrication, optimization, and characterization of skin bioelectrode materials. The adhesive hydrogels and the Au nanomesh conductor are chemically synthesized. Their electrical, optical, mechanical, and morphological information is characterized, and its fabrication process is optimized.

Chapter 5 elaborates the details of the design, fabrication, optimization, and characterization of silk-based hydrogel materials with antimicrobial properties. The hydrogel is made from the co-assembly of silk fibroin and Fmoc-protected amino acids. Fmoc-Leu-OH presents gram-positive antimicrobial property for the hydrogel. The assembled hydrogel showed promising killing efficiency against gram-positive B. subtilis. In addition, a tough, wearable, conformal, and antimicrobial hydrogel with silk fibroin and the chemical hydrogel is also presented.

Chapter 6 elaborates on the applications of skin bioelectrodes in the measurement of biopotential signals from human skin. Two types of biopotential signals (ECG and EMG) are measured. A novel PSA-coated technique to endure all the conductive film adhesive to the skin is presented. This technique allows all non-adhesive electrode surfaces, irrespective of their conductive materials or substrate materials adhesive to the skin. This can greatly solve the conformal issue related to most of the skin bioelectrodes.

Chapter 7 elaborates the reflections on the results of the thesis. The hypotheses proposed at the beginning of the thesis are tested and reviewed. Implications of the work conducted in this thesis include the development of adhesive hydrogel materials with high mechanical, electrical, and antimicrobial properties as skin bioelectrode materials, as well as a versatile coating technique that endows non-adhesive stretchable electrodes with high conductivity and adhesiveness.

1.4 Findings and Outcomes/Originality

This research led to several novel outcomes by:

1. Developing an adhesive hydrogel system with optimized properties for on-skin bioelectrode applications.

2. Chemically functionalization of hydrogels with antimicrobial properties for preventing biofilm formation.

3. Inventing a universal adhesive coating technique that allows most of the non-adhesive electrodes conformally attached to the skin.

4. Integrating a wearable system for wireless biopotential signal measurement.

References

[1] Y. Wang, W. Pei, K. Guo, Q. Gui, X. Li, H. Chen, J. Yang, Science China Information Sciences 2011, 54, 2435; G. Acar, O. Ozturk, A. J. Golparvar, T. A. Elboshra, K. Böhringer, M. K. Yapici, Electronics 2019, 8, 479; R. F. Yazicioglu, T. Torfs, P. Merken, J. Penders, V. Leonov, R. Puers, B. Gyselinckx, C. Van Hoof, Microelectronics Journal 2009, 40, 1313; M. A. Yokus, J. S. Jur, IEEE Transactions on Biomedical Engineering 2016, 63, 423; Y. M. Chi, T. Jung, G. Cauwenberghs, IEEE Reviews in Biomedical Engineering 2010, 3, 106.

[2] J. G. Webster, *Medical Instrumentation: Application and Design*, WILEY, 2010.

[3] Ø. G. M. Sverre Grimnes, *Bioimpedance and Bioelectricity Basics, 3rd Edition*, Elsevier, 2015.

[4] L. Pan, P. Cai, L. Mei, Y. Cheng, Y. Zeng, M. Wang, T. Wang, Y. Jiang, B. Ji, D. Li, X. Chen, Advanced Materials 2020, 32, 2003723; Z. Liu, D. Qi, G. Hu, H. Wang, Y. Jiang, G. Chen, Y. Luo, X. J. Loh, B. Liedberg, X. Chen, Advanced Materials 2018, 30, 1704229.

[5] C. Konya, H. Sanada, J. Sugama, M. Okuwa, Y. Kamatani, G. Nakagami, K. Sakaki, Journal of Clinical Nursing 2010, 19, 1236; S. Fumarola, R. Allaway, R. Callaghan, M. Collier, F. Downie, J. Geraghty, S. Kiernan, F. Spratt, J. Bianchi, E. Bethell, A. Downe, J. Griffin, M. Hughes, B. King, K. LeBlanc, L. Savine, N. Stubbs, D. Voegeli, Journal of Wound Care 2020, 29, S1.

[6] A. Miyamoto, S. Lee, N. F. Cooray, S. Lee, M. Mori, N. Matsuhisa, H. Jin, L. Yoda, T. Yokota, A. Itoh, M. Sekino, H. Kawasaki, T. Ebihara, M. Amagai, T. Someya, Nature Nanotechnology 2017, 12, 907.

Chapter 2

Literature Review

This chapter reviews the background of biopotential signals (ECG, EMG, and EEG) measured from human skin. Human skin is briefly introduced with an emphasis on its complicated microstructure. The measurement processes require skin bioelectrodes as an interface with skin and external amplifier devices. The amplifier electronics are introduced specifically designed for human biopotential measurement. Skin bioelectrodes are a key part of this chapter. Two types of electrodes, wet electrodes, and dry electrodes are introduced. Wet electrodes usually have a structure of the hydrogel-metal nanofilm-elastomer substrate, while dry electrodes only have metal nanofilm-elastomer substrate. Techniques to make electrode arrays including active matrix and passive matrix are also briefly introduced.

2.1 Biopotentials of human body

The human body is a complex system that requires fast signal transmission to coordinate different parts. It constantly generates electrical signals in response to different stimuli, to transmit information for sensing and actuation[1]. The electricity in the human body is generated and transmitted through excitable cells or tissues, including nerve cells and muscle cells[2] (Figure 2.1a). Nervous cells need electrical signals for fast response to an external stimulus or sending instant commands to peripheral organs. Muscular cells need electrical signals for cardiac muscle pumping and skeletal or smooth muscle contraction and stretching. The excitable cells have a resting membrane potential (Figure 2.1b). Under proper stimulation, it can be excited as action potential (AP). The AP can transmit with an "all or none" rule along the cell membrane. Cell excitation is an ionic flux process on the cell membrane. An excitable cell maintains a stable resting potential difference (-40 to -90 mV) between the inside cell membrane (intracellular) and outside cell membrane (extracellular) due to the ion concentration differences of Na^+, K^+, and Cl^- as well as the membrane structure. The resting potential (or equilibrium potential) due to these ions can be determined by the Nernst equation,

$$E = \frac{RT}{F} ln\{\frac{P_K[K]_o + P_{Na}[Na]_o + P_{Cl}[Cl]_o}{P_K[K]_i + P_{Na}[Na]_i + P_{Cl}[Cl]_i}\}$$

Where E represents resting (equilibrium) potential, P_K, P_{Na}, and P_{Cl} represent the permeability coefficients of the ions which can be determined by Goldman-Hodgkin-Katz (GHK) formulation. Maintaining such resting potential requires the active transport of Na^+ and K^+ ions by the sodium-potassium pump.

When an adequate stimulus presents on the excitable membrane that changes the transmembrane potential exceeding a threshold. AP will be elicited as a fast depolarization and repolarization (Figure 2.1c). The magnitude of the polarization is around 120 mV with a duration of around 1 ms. In this duration period, another AP cannot generate, this "cooling down" period is called the refractory period. One prominent characteristic of this AP is the

"All or none" rule, which means when the stimulus is below the threshold, no AP will generate, once it is above the threshold, the AP with fixed amplitude and duration will generate. The reason of AP generation by the adequate stimulus lies in the voltage and time-dependent ion channel (Na^+, K^+, and Cl^-) membrane permeabilities (also called membrane conductance). The combined and successive change of membrane permeabilities allows the inflow of Na^+ (depolarization), and outflow of K^+ and Cl^- (repolarization). The waveform of AP with consideration of ion channel permeability can be calculated by the Hodgkin-Huxley model[3] (Figure 2.1d).

$$C_m \frac{dV_m}{dt} = g_K(V_K - V_m) + g_{Na}(V_{Na} - V_m) + g_l(V_m - V_l) + i_{stim}$$

Where g_K, g_{Na}, and g_l are the permeabilities of K^+, Na^+, and leakage current, i_{stim} is the stimulation current.

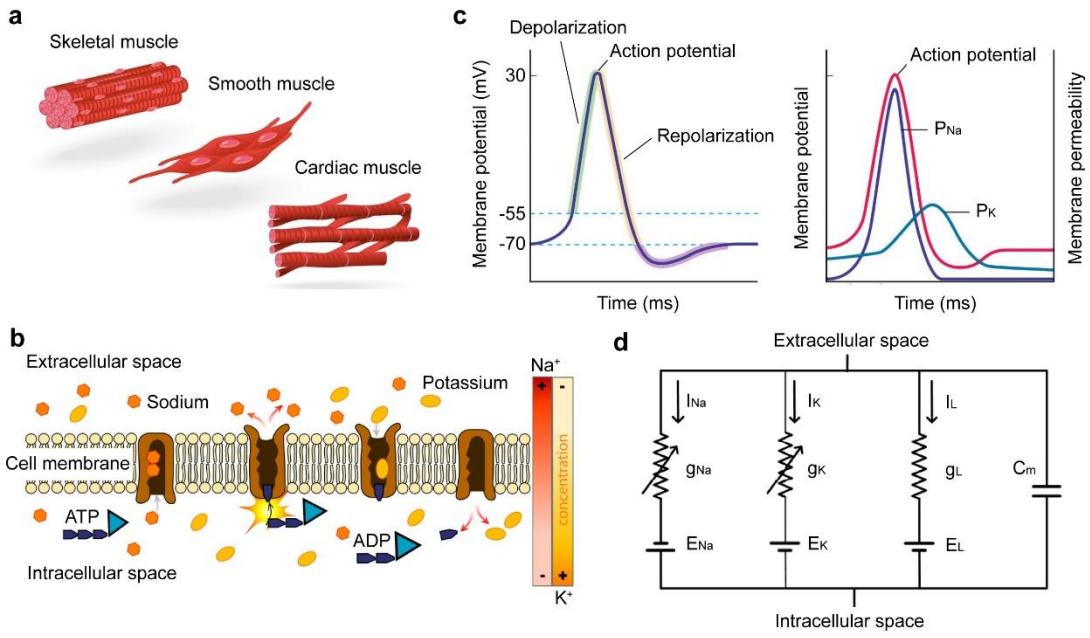

Figure 2.1 The biological origin of biopotential in the human body. (a) Muscular cells (including skeletal muscle, smooth muscle, and cardiac muscle) and neurons are excitable cells that can generate AP. Figure reproduced from Ref[4]. (b) The cell membrane structure that excitable for AP generation. The membrane potential is maintained by the active transport of sodium and potassium pumps. A concentration gradient of sodium and potassium between the extracellular and

intracellular space defines the resting potential. Upon a stimulus exceeding the threshold, the permeability of the ion channels dramatically changes, altering the membrane potential, forming AP. Figure reproduced from Ref[5]. (c) The waveform of AP. AP starts from its resting potential (around -70 mV), with depolarization and subsequent repolarization. The depolarization is due to increased inflow Na^+ permeability and repolarization is due to increased outflow K^+ permeability. Figure reproduced from Ref[6]. (d) Hodgkin-Huxley model to simulate the AP waveform. The cell membrane is treated as an equal circuit of membrane capacitance, variable Na^+ current, K^+ current, and leakage current. Figure reproduced from Ref[7].

The AP signal along the cell membrane is the basic form of bioelectricity inside the human body. However, the measurement of AP requires the instrumentation (patch clamp) at the cellular level. Moreover, in the human body, there are huge amounts of cells firing electrical signals at the same time. The collective effect of excitable cells reflects the physiological meaning. Therefore, the measurement of potential change away from (biopotential) the signal source (the cell membrane) is important. In the human body, the excitable tissue can be treated as a current source and passive tissue can be regarded as a volume conductor (with specific resistivity ρ). In this case, the extracellular electrical signal can be measured. This allows us to measure the biopotential signal outside the excitable cells, even on the human skin. Measuring biopotential signals on skin has become an important clinical diagnosis method due to its non-invasiveness, convenience, well-established theory, high accuracy. For example, ECG, EEG, and EMG based on surface biopotential measurements have been developed.

2.2 ECG, EMG, and EEG

The heart is the key organ for the circulatory system in the human body, pumping oxygen-rich blood and recycling oxygen-poor blood throughout the human body. The cardiac muscle rhythmically contracts and relaxes for blood pumping and refilling, well-coordinated by a series of electrical signals propagating through the heart. The electrically excitable cells of the heart include a SA (sinoatrial) node, AV (atrioventricular) node, atrial muscle, His fiber, Purkinje fiber, ventricular muscle (Figure 2.2). Different cell exhibits different types of characteristic action potentials. During an electrical signal cycle in the

heart, the electrical signal impulse initiates at the SA node, propagating into the atrial muscle, activating the contraction of the atrium. The electrical impulse then experiences a little delay at the AV node, then enters His bundle and Purkinje fiber, and then spread into ventricular muscle, activating the contraction of the ventricle. The combined action potential signals result in an ECG waveform composing P wave, QRS complex, and T wave. The ECG waveform includes rich information about the heart activity of the atrium and ventricles. P wave reflects atrial depolarization, the QRS complex is from ventricular depolarization, and the T wave is due to ventricular repolarization. The atrial repolarization is usually buried in the QRS complex. The P-R and S-T periods are the zero-value baselines. The P-R interval is the delay period of the AV node. The S-T interval is caused by the ventricular cells. Heart rate can also be obtained by calculating the reciprocal of R peak intervals.

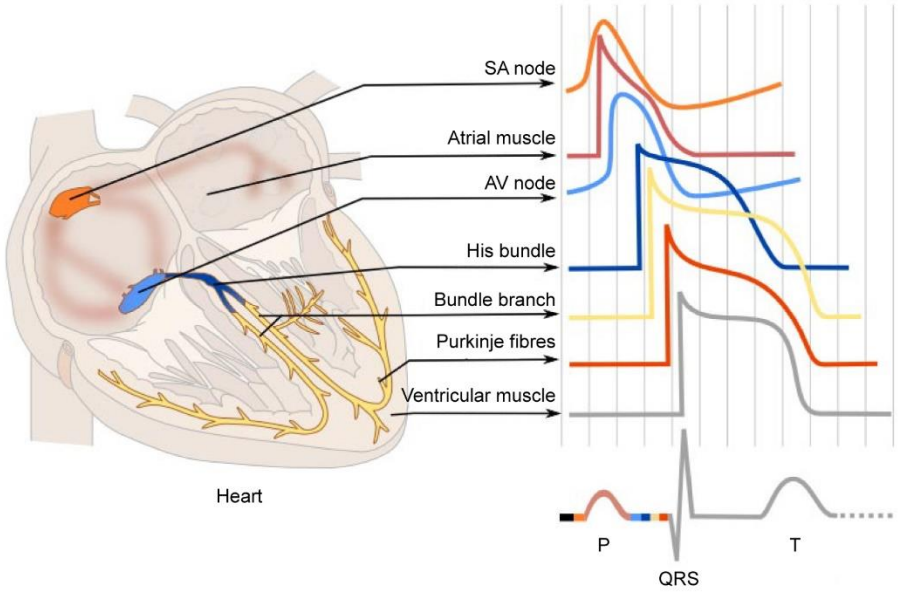

Figure 2.2 Electrical signals from different parts of the heart and the resultant ECG signal. ECG signal usually includes a preceding P wave, a QRS complex wave, and a T wave. The amplitude of the ECG signal is usually around 1 – 3 mV. Figure reproduced from Ref[8].

The electrical impulse-activated heart rhythm results in a current flow in the thoracic volume conductor (a passive conductive tissue with specific resistivity ρ). This current flow in the bulk volume conductor, initiated by a heart electrical impulse, results in a

surface potential change at the surface human body, which can be measured from the so-called ECG. The most signal measurement of ECG is the 3-lead method, which places three electrodes on the right arm, left arm, and left leg, respectively (Figure 2.3a). Three surface potential vectors can be obtained from the right arm to the left arm, from the left arm to the left leg, and from the right arm to the left leg. These three surface potential vectors represent different electrical activity orientations of the heart. When connecting the electrodes on the human body with measurement instrumentation, the human body can be simplified as an equivalent circuit diagram (Figure 2.3b). The heart, which generates electrical impulses, can be regarded as a constant current generator. The current flows into torso tissue, which is a volume conductor, with resistances represented by R1 and R2. Considering two measuring electrodes placed at A and B, the potential difference (Φ_A - Φ_B) can be obtained as an ECG waveform. The ECG waveform depends on the location of electrodes. In clinic application, there is a standard 12-lead ECG measurement. Six leads are placed on a limb and another six leads are placed on the torso (precordial), which are called limb lead I, II, III, aVL (augmented Voltage Left), aVR (augmented Voltage Right), and aVF (augmented Voltage Feet). The schematic in Figure 2.3a shows the limb lead I, II, and III. The six precordial leads are called V1, V2, V3, V4, V5, and V6. The 12-lead ECG gives 12 traces of heart electrical signals, which are helpful to diagnose more than 100 types of heart problems[9, 10].

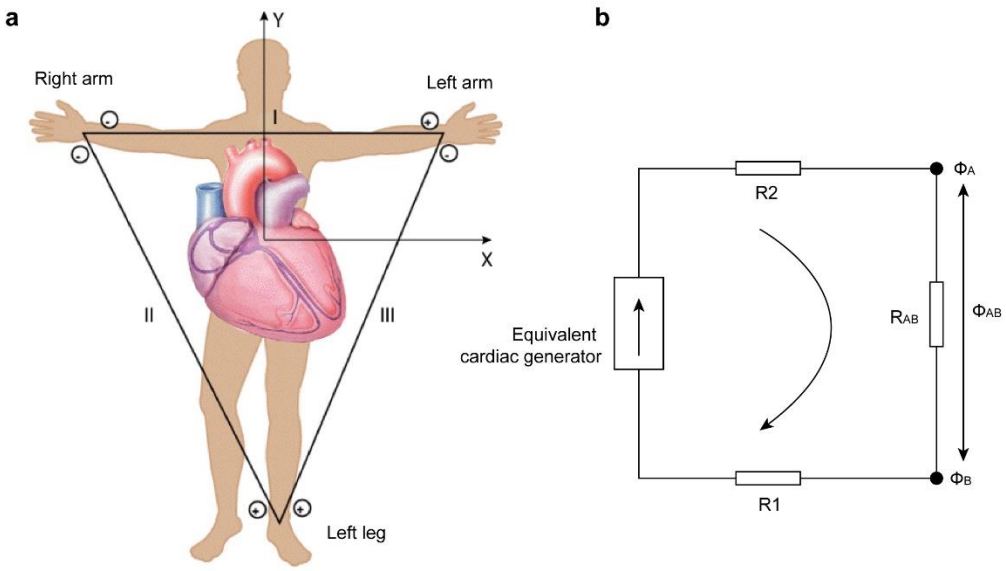

Figure 2.3 The surface biopotential of ECG. Left, Schematic of surface ECG measurement using a 3-lead method. Electrodes can be placed on the right arm, left arm, and left leg of the human body, the potential difference between these three electrodes can be measured. Figure reproduced from Ref[9]. Right, Equivalent circuit diagram of the ECG measurement. The heart can be regarded as an equivalent cardiac generator. R1 and R2 represent the tissue resistance from the heart to the measuring point A and B. Φ_A and Φ_B represent the potential at measuring point A and B. Φ_{AB} represents the potential difference between the two points. Figure reproduced from Ref[9].

The human brain is a complex organ with powerful memory and computing capability. Brain activity is supported by millions of neuronal activities. The neuronal activities generate current flowing along the excitable membranes. As the excitable neurons were embedded in passive conductive tissues, which can be regarded as a volume conductor, electrical neuronal activity can be measured from the surface of the volume conductor (the surface of the brain)[11]. The individual neuronal activity is reflected as synaptic current and spike potential at a microscopic scale (Figure 2.4a). When a local network of thousands of neurons fire electrical signals, the local field potential (LFP) is formed. At the macroscopic scale, concurrent electrical activities of millions of neurons ultimately contribute to the brain's electrical activity, which is known as the EEG[12, 13]. EEG has become a powerful diagnostic method to evaluate neurological diseases, such as seizures, epilepsy, etc. It is also widely used to study mental status. EEG signals are classified,

depending on their frequency band, as the alpha wave, beta wave, delta wave, theta wave, and gamma wave (Figure 2.4b). Gamma wave is in a frequency range of 30 – 120 Hz, it reflects hyper brain activity. Beta wave is in a frequency range of 13 – 30 Hz, it is related to the subject concentrating, alert, and anxious status. Alpha wave is in a frequency range of 7 – 13 Hz, it is related to relaxed status. Theta wave is in a frequency range of 3 – 7 Hz, it is related to drowsy and falling to sleep status. Delta wave is in a frequency range of 0.5 – 3 Hz, it is related to sleeping status. As such, the EEG waves contain rich information about a subject's mental status. EEG signals are usually in the amplitude range of tens of microvolts (μV), the measurement of which requires a high precision amplifier. EEG signals are usually measured from a surface electrode array all over the scalp. As the signal amplitudes are very small, conductive gels are usually applied to the scalp to ensure high signal fidelity.

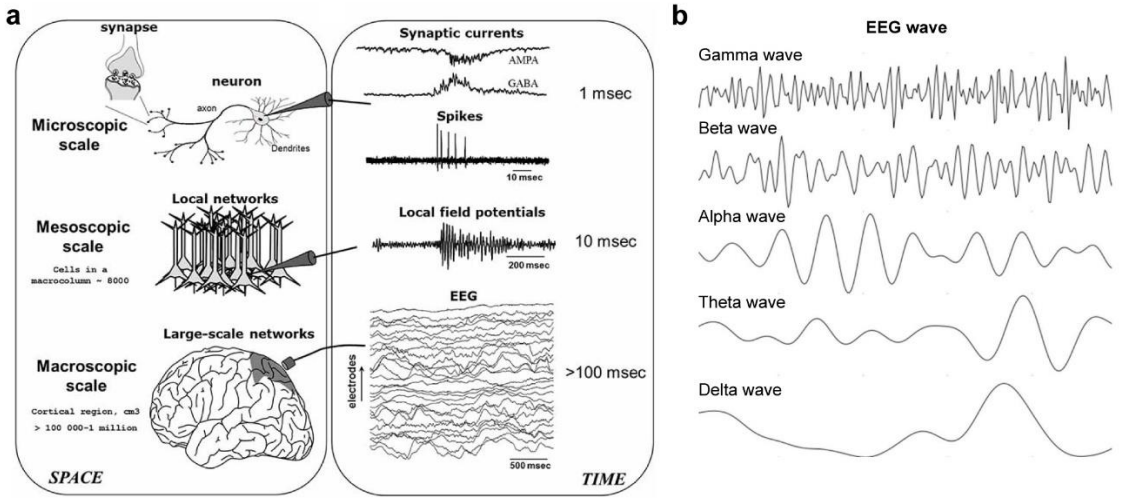

Figure 2.4 Electrical activities of the brain. (a) The brain's electrical activity is a multilevel process at different time and space scales. The single neuron at the microscopic scale generates synaptic currents and spike potentials. The local network of thousands of neurons working together generates local field potentials (LFPs). When millions of neurons work at a synchronized pace, an EEG signal is formed by the summation of the millions of neurons. Figure reproduced from Ref[13, 14]. **(b)** Different wavebands of EEG signals. The main EEG signal waves classified at different frequencies include delta, theta, alpha, beta, and gamma waves. Figure reproduced from Ref[15].

The muscle is the main tissue that functions as actuation of the human body. Muscles can be classified as skeletal muscle, smooth muscle, and cardiac muscle. Skeletal muscle is attached to bones, controlled by the central nervous system (CNS), and responsible for skeletal movement. The skeletal muscle is composed of muscle fibers. Smooth muscle is in the wall of internal organs such as the gastrointestinal tract, bladder, and blood vessels. Smooth muscle is controlled by the autonomic nervous system and not voluntarily controlled by CNS. Cardiac muscle is in the walls of the heart, also controlled by the autonomic nervous system. The movement of cardiac muscle is controlled by ECG signals. The EMG signal is from skeletal muscle. Skeletal muscle is organized as muscle fibers. Each bundle of muscle fibers is controlled by CNS from the spinal cord. Motor units connect the spinal cord nerves and muscle fibers, joining muscle fibers by ending plates (Figure 2.5 left). During the activation of the muscle fibers. Neurons first fire excitation AP. The excitation AP propagates through the motor unit to the endplate, activating all muscle fibers connecting with the muscle unit. The activated muscle fibers, when contracting, also emit AP which is called muscle fiber AP[16] (Figure 2.5 right). Each muscle fiber AP has an amplitude of 20 – 2000 μV and a duration of 3 – 30 ms, depending on the size of the motor unit. Considering each muscle fiber AP is a current source of bioelectricity, as one motor unit may connect with different interspersed muscle fibers, a single motor unit includes distributed current sources. When measuring surface EMG from the skin, it measures the biopotential field of a volume conductor (the connective tissue around the muscle). EMG signal is the summation of many motor units firing APs. To extract the single motor unit or motor neuron information, surface EMG signals need to be decomposed. EMG signals can be used to assess the health of muscles and motor neurons, reveal nerve and muscle dysfunction. Today EMG signals are also widely used for gesture recognition and human-computer interface.

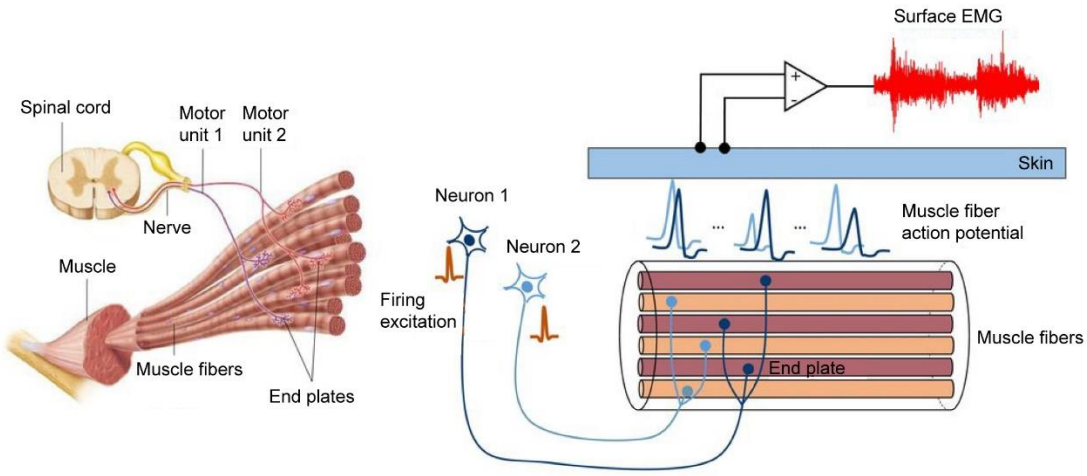

Figure 2.5 Motor unit structure and EMG signal of skeletal muscle. Skeletal muscle is composed of muscle fibers that can be stretched or rested. The muscle fibers are controlled by Central Nervous System (CNS) in the spinal cord. Motor neurons connect with muscle fiber through the motor unit. Each motor unit connects with several interspersed muscle fibers. During the muscle activation, motor neurons will fire excitation AP to transmit through the motor unit to muscle fibers. The muscle fibers, when activated, will contract. Activated muscle fibers also emit local field AP. Each muscle fiber AP acts as distributed current source, surrounded by a volume conductor. When measuring potential change on the surface of volume conductor (skin), surface EMG is measured which is the summation of many muscle fibers. Figure reproduced from Ref[17].

2.3 Electronic circuits for on-skin biopotential measurement

The biopotential signals are usually very small (from 10 µV to 3 mV), requiring amplification to be reliably measured. The amplifier is mostly used with interfacing sensors for reliable data acquisition. The understanding of amplifier circuits can greatly improve the signal quality, remove noises, and find different suitable circuits for different usages. The operational amplifier (op-amp) is the basic of amplifier circuit design. The understanding of op-amp is the key in designing electronic circuits for biopotential measurement.

The classic symbol of an op-amp is shown in Figure 2.6a. An op-amp has two inputs, one is inverting input (V-) and another one is non-inverting input (V+). The output is Vout =

V+ - V- when the amplifier is in a linear range. The properties of the op-amp are usually described ideally as: 1) gain is infinity, 2) input impedance is infinity, 3) output impedance is zero, 4) bandwidth is infinity, and no phase shift. This gives two basic rules about ideal op-amp: 1) When the op-amp output is in the linear range, the two inputs are at the same voltage. This is because the gain of an ideal op-amp is infinity, any small difference between the two inputs will be amplified to infinity. The limitation of op-amp voltage is determined by its supply voltage, which is usually ±15 V. Nowadays amplifiers with a small voltage supply (3V) are available. 2) no current flows into either input of the op-amp. This is because the input impedance of the ideal op-amp is infinity. No current can flow through an infinite resistance. Due to its infinite gain and zero linear range, an op-amp is not ideal to use. Instead, op-amp needs to be modified for practical uses. An inverting amplifier is more commonly used in instrumentation (Figure 2.6b). A part of the output voltage is fed back into the negative input, called negative feedback. It increases bandwidth and lowers output impedance. Most importantly, the gain is not infinity anymore. Vout can be expressed as Vout = -Vin*Rf/Ri, which is negatively proportional to Vin. Another commonly seen amplifier is voltage follower (Figure 2.6c). In this case, Vout can be expressed as Vout = Vin*(Rf+Ri)/Ri, which is positively proportional to Vin. In biopotential signal measurements, a potential difference between two electrodes on the human body usually needs to be measured. This differential input format requires the installation of an instrumentation amplifier, which is composed of three op-amps (Figure 2.6d). The first two op-amp works as a voltage follower, which greatly increases the input impedance of each terminal. To reject the common-mode noises, 2 R2 and 1 R1 were arranged in such an order that eliminates the two op-amp's connections to the ground. The common-mode rejection ratio (CMRR) in this case is G = (2R2+R1)/R1. The third op-amp along with R3 and R4 works as a differential amplifier to subtract the two inputs from op-amp 1 and op-amp 2. The instrumentation amplifier configured in such a 3-op-amp structure is widely used in biomedical engineering. It has some significant benefits, such as high input impedance, high CMRR, an adjustable gain that is controlled by R1.

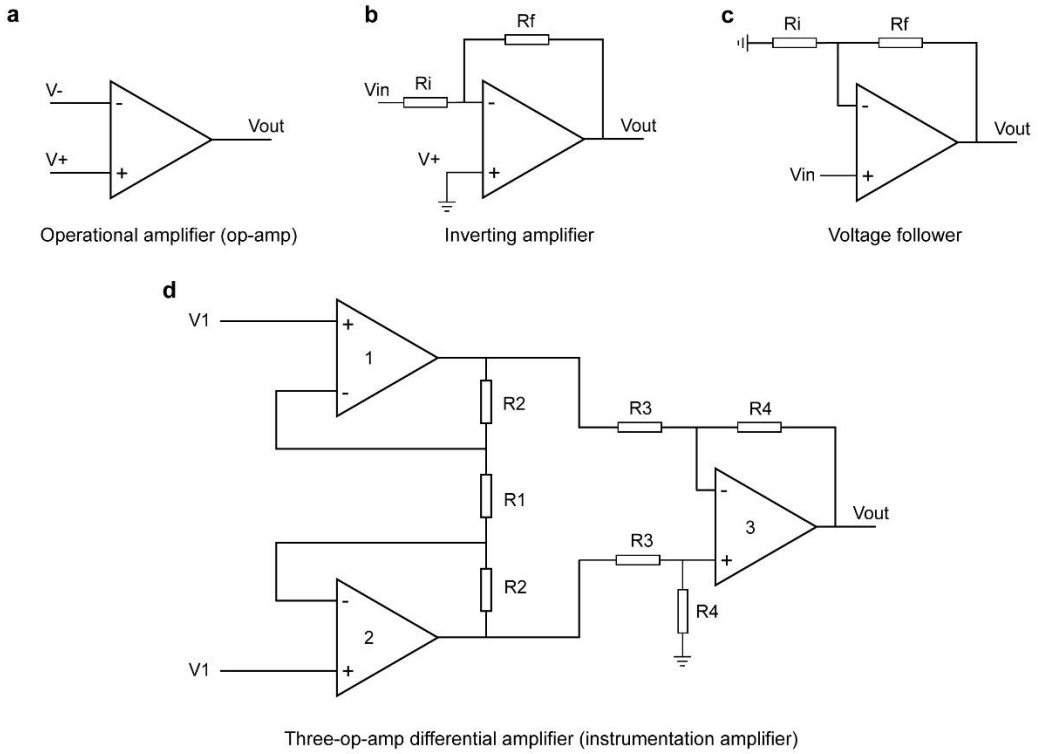

Figure 2.6 Different amplifier circuits for biopotential measurement. (a) An op-amp amplifier with non-inverting and inverting inputs and an output. (b) An inverting amplifier with negative feedback and non-inverting input grounded. (c) A voltage follower amplifier with negative feedback and grounded non-inverting input. (d) An instrumentation amplifier (three-op-amp differential amplifier) with high input impedance and high CMRR.

With the advancement of amplifier technologies, especially the instrumentation amplifier, biopotential signals with different frequencies (from 0.1 Hz to 1000 Hz) and different amplitudes (from 10 μV to 10 mV) can be measured. However, in the practical measurement of biopotential signals, various problems may be encountered. As such, many other factors need to be considered when designing biopotential amplifiers. For example, frequency distortion can happen in ECG signals when the frequency-response standard is not met. The sharp QRS complex may be rounded off in a high-frequency distortion. The baseline may be no longer horizontal in low-frequency distortion. DC offset in the electrodes may also improperly amplify the signal to a saturation or cutoff region that is the QRS complex may be cut off. In other cases, the amplifier may be disconnected from the electrodes. High drifting potentials may be induced in the open-wire due to electrical

fields from the power lines or machines in the vicinity. To prevent the open wire problem, a firm connection between electrodes and amplifiers should be confirmed before measurement. The most significant problem during biopotential measurement is the interference from the electric power system. This interference can come from power lines in the walls, floors, and ceiling, also nearby machines, or appliances. This 50-Hz interference is a result of electric-field coupling between the power lines and the ECG wires or the human body.

As illustrated in Figure 2.7, the power line can capacitively couple with the human body (represented by C_b). This displacement current (i_{db}) flows through the body to the ground, creating a common-mode voltage. Assuming the i_{db} to be 0.2 μA and a ground impedance to be 50 kΩ, such common-mode voltage can be 10 mV, even larger than the ECG amplitude (1 – 2 mV). For a perfect biopotential amplifier with high input impedance and CMRR, this common-mode voltage is not a problem. However, it is recommended to use an amplifier with high input impedance as well as minimize the skin-electrode impedance. The power line also induces a capacitive current in the lead wires, which is a more severe problem in the ECG measurement. As shown in Figure 2.7, C_1 and C_2 represent the capacitance between the power line and the leads. The displacement currents (i_{d1} and i_{d2}) do not flow into the amplifier due to its high input impedance but flow into the skin-electrode impedance and the subject being measured to ground, causing a signal noise as measured by the two leads. Such noise voltage can be estimated as 120 μV, which is an objectionable level compared with ECG, EMG, and EEG. To minimize the noise, shielding of the lead and grounding of the shielding is an engineering practice. More importantly, skin-electrode impedance should be kept as low as possible.

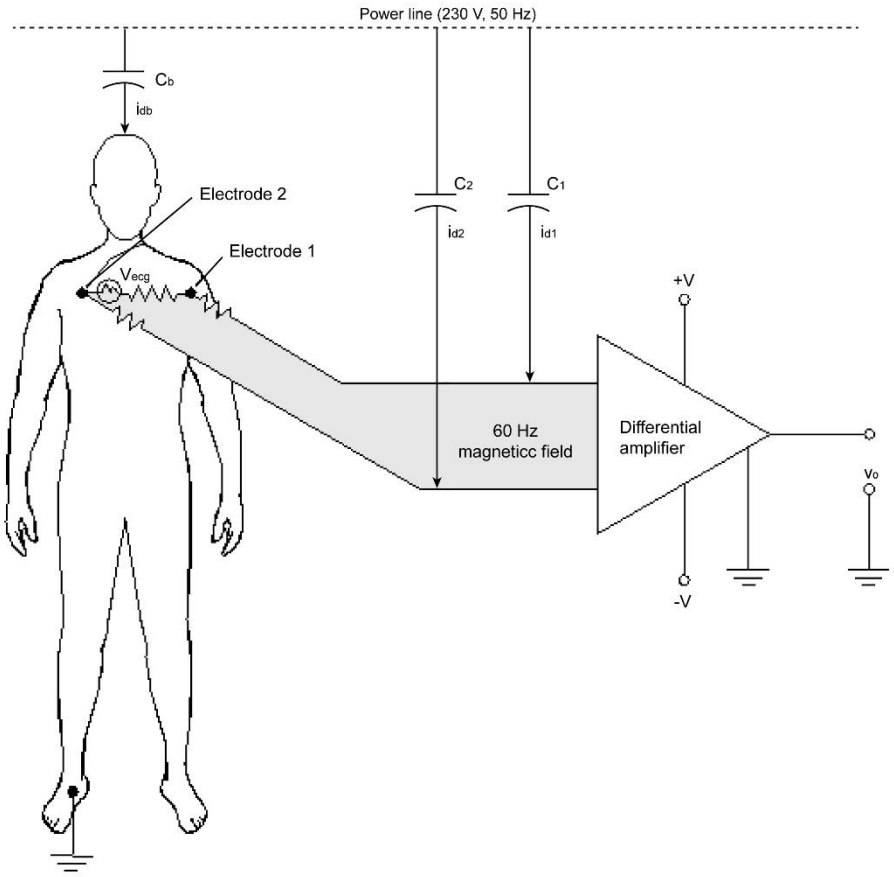

Figure 2.7 Mechanism of electric field coupling of the power line on ECG measurement. There are three ways that the power line (230V and 50 Hz) can interfere with ECG measurement. First, the electric field of the power line can capacitively couple with the human body, inducing a capacitive current flow (i_{db}) in the human body. The current can flow into the measured loop, causing signal noises. Similarly, the power line can also capacitively couple with the lead wires, adding more currents (i_{d1} and i_{d2}) into the measured loop. Figure reproduced from Ref[18].

2.4 Human skin

The biopotential signals can be measured from the skin due to signal transmission from the signal source (heart, muscle, nerves) to the volume conductor (other passive conductive tissues of the body). The skin biopotential measurement provides a non-invasive and convenient way in a wide range of clinical diagnoses. To develop skin-based bioelectrodes, the understanding of skin is important. Skin and its related appendages are the largest organs of the human body, covering an area of 2 m^2 and weighing 15% of body weight.

The skin is a multilayer structure (Figure 2.8). The outmost layer is mainly keratinocytes. Between the epidermis and dermis is the basement membrane, which connects the two layers. The layer below the dermis is called hypodermis, which is mostly fat. The epidermis layer, which is in direct contact with the bioelectrodes, is most important in understanding the skin-electrode interface. The primary function of the epidermis is a physical and biological barrier to the external environment, preventing penetration by irritants and allergens. It also prevents water loss and maintains internal homeostasis. The epidermis is mostly stratified squamous epithelium, which is composed of keratinocytes in progressive stages of differentiation. Keratinocytes produce protein keratin as the major building blocks of the epidermis. The skin contains hairs and various microstructures on its surface. It also excretes sweat and oily substances from its glands. All these geometric and chemical characteristics add to the challenges of applying bioelectrodes onto human skin.

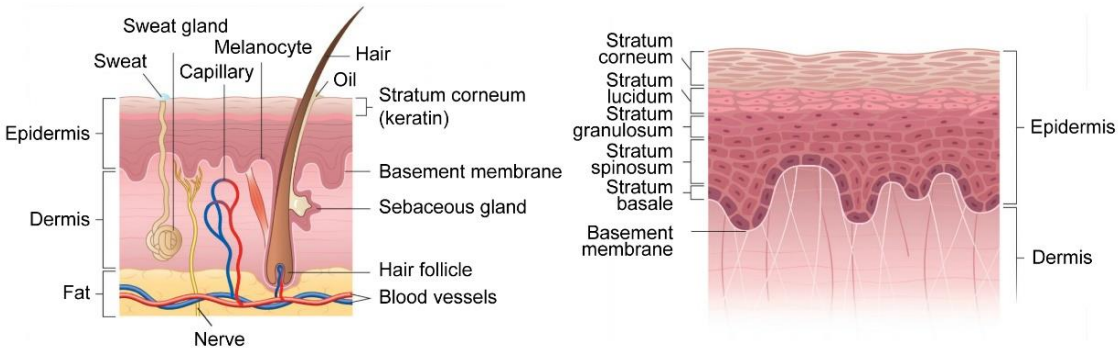

Figure 2.8 The skin anatomy and structure. Skin is a multilayer protective barrier with glands and hair appendages. Figures reproduced from Ref[19].

2.5 Electrode for biopotential measurement

The measurement of biopotential signals (such as ECG, EEG, and EMG) requires bioelectrodes on the skin. The first requirement on bioelectrodes is that they should be biocompatible to the skin (no irritation, inflammation, or toxic chemicals released into the skin). Apart from biocompatibility, the bioelectrodes should also be able to effectively transduce weak biopotential signals inside the body into measurable electrical signals in

the amplifier. This requires a delicate design of bioelectrodes from materials, structural, and electrochemical perspectives.

Bioelectrodes can be classified as current carry electrodes (for electrostimulation) and potential pick-up electrodes (for measuring biopotential difference)[20]. The current-carry electrodes require the desired amount of current flow between the electrodes, while the pick-up electrodes have negligible current flows. The biopotential measured is endogenic from a body organ. A most typical electrode system is Ag/AgCl or metal plate with electrolytes (Figure 2.9). For Ag/AgCl electrode, the Ag is coated with a layer of AgCl. The AgCl layer is in contact with electrolyte gel, which further contacts the skin stratum corneum. Electrochemical reaction forms at the AgCl-electrolyte interface. For metal electrodes, the metal surface (Au, Pt, stainless steel, carbon) is in direct contact with an electrolyte gel. Electric double-layer forms at the metal-electrolyte interface.

Apart from materials type, bioelectrodes can be classified as polarizable or nonpolarizable electrodes. For polarizable electrodes, their interface resistance with electrolytes is characterized by a parallel polarizing resistance R_{pol} and polarizing capacitance C_{pol}. Highly polarizable electrodes are determined by a large C_{pol}, making the electrode like a capacitor, if it is charged, there is no more current flow, and the output voltage is 0. Ag, Au, and stainless steel are highly polarizable electrodes. Ag/AgCl is a nonpolarizable electrode as it has a well-defined DC potential not very dependent on DC flow. It is useful for measuring DC potentials and suitable as reference electrodes. However, Ag and AgCl are toxic and the contact with living tissue remains a biocompatible issue. When working as a cathode, the AgCl layer can dissolve away, significantly changing the electrode property.

The electrolyte gel in contact with electrode and skin is an ionic conductor. The electrolyte gel plays an important role in the bioelectrode system as it 1) serves as a high-conductance salt bridge from the metal to the skin, 2) enable the metal-electrolyte interface to be kept at a distance from the skin, 3) maintain a small junction potential, 4) fill out voids and air gaps between electrode metal and skin, 5) and wet the poorly conducting skin stratum

corneum. The interface between electrode and electrolyte is called electrode area, while the interface between electrolyte and skin is called effective electrode area. Skin bioelectrodes usually have an effective electrode area larger than the electrode area. A larger electrode area can decrease electrode polarization impedance, a larger effective electrode area can reduce noises, but increase the signal-averaging effect, and lose spatial resolution. Another effect of electrolyte gel is its penetration into skin and sweat ducts and wetting of the stratum corneum. As the skin impedance is usually much higher than electrode polarization impedance, the wetting of the skin stratum corneum by electrolyte can greatly reduce the impedance. High concentration electrolytes can penetrate the skin in less than 10 min. However, skin irritation may occur due to electrolyte penetration. NaCl is more mild electrolytes to human skin than other electrolytes. Different from the electrolyte in liquid format, the hydrogel is a solid crosslinked polymer material containing more than 90% water. Hydrogel as the electrolyte to contact skin and electrode has a higher capacitance, indicating that it will attenuate low-frequency signals and is more proper in high-frequency signals.

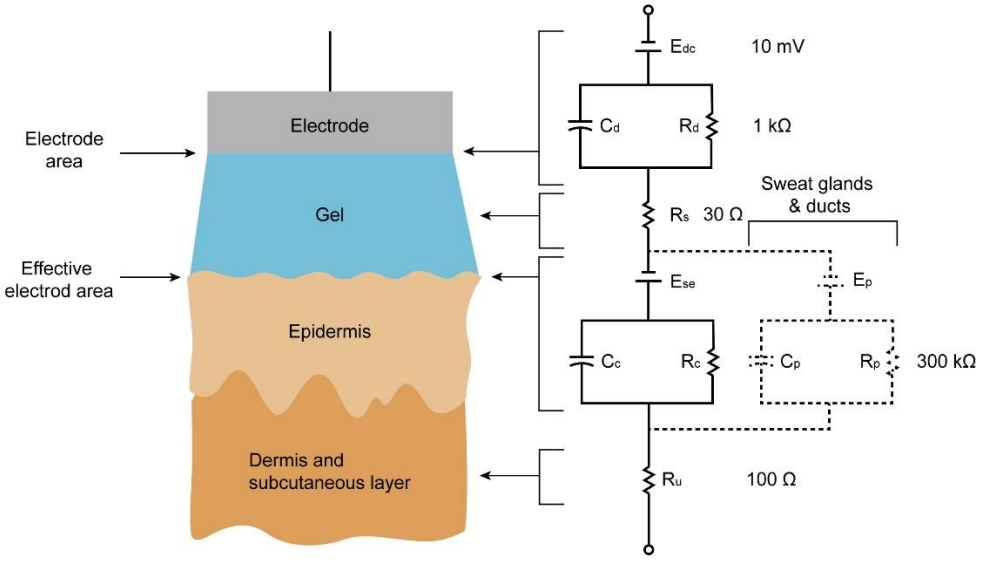

Figure 2.9 Equivalent circuit of electrode and skin interface. Electrode and electrolyte gel is placed on the skin. Two interfaces are important, one is the electrode-electrolyte interface, and the other is the electrolyte-epidermis interface. The electrode-electrolyte interface can be modeled as a DC battery (E_{dc}) and a capacitor (C_d) and resistor (R_d) in parallel. E_{dc} is due to the polarization of

the electrode, around 10 mV. C_d is due to the double layer capacitor and absorption capacitor, and R_d is due to the charge transfer resistance. The parallel C_d and R_d represent electrode impedance, which is usually around 1 kΩ. The gel itself has an Ohmic resistance R_s. The interface between the electrolyte and epidermis forms another DC battery (E_{se}). This is because the stratum corneum acts as a semipermeable membrane separating different ion concentrations. Sweat glands and ducts may also contribute extra components. The electrolyte-skin interface contributes the highest impedance in the system (around 300 kΩ). The skin tissue beneath the stratum corneum can be simplified as a passive resistor with a value around 100 Ω.

2.6 Materials design of conformal bioelectrodes

The measurement of biopotential signals (ECG, EEG, EMG, etc.) requires on-skin bioelectrodes. To obtain the high-quality signal, some desired properties of the electrode need to be considered (Figure 2.10). Firstly, skin is a soft (Young's modulus around 0.5 MPa) and stretchable (maximum 70% strain) organ[21], it is easily stretched or contacted under body movement. Bioelectrodes in the rigid metal plate format can cause relative motion during skin stretching or contacting thus causing motion artifacts in the signal. As such, the novel skin bioelectrodes need to be soft the match Young's modulus of the skin, otherwise, the electrode will constrain the skin movement. It also needs to be stretchable to accommodate skin stretching. Secondly, the outmost layer of skin is a stratum corneum with excreted oily substances and hairs. The bioelectrodes on the skin can easily detach during skin movement. As such, the bioelectrodes need some degree of adhesiveness towards the stratum corneum despite its oily substances or hairs. Thirdly, the skin as a barrier organ needs to constantly expel excretes (sweat, oily substance, water, etc.) to the environment, blocking of the skin excreting ability can cause dysfunction of skin physiology. As such, the electrode needs to be breathable to allow substance exchange between the skin and the environment. Fourthly, despite the dry stratum corneum coverage, the skin is a relatively fragile organ, the leakage and diffusion of toxic chemicals into the skin can cause skin inflammation, irritation, or even damage of skin tissue. As such, the skin needs to be biocompatible, without toxic leakage to the skin. Lastly but most

importantly, as a device to transduce ionic current to electrical current or vice versa, the electrode needs to be highly conductive to reduce the signal loss in the electrodes[22].

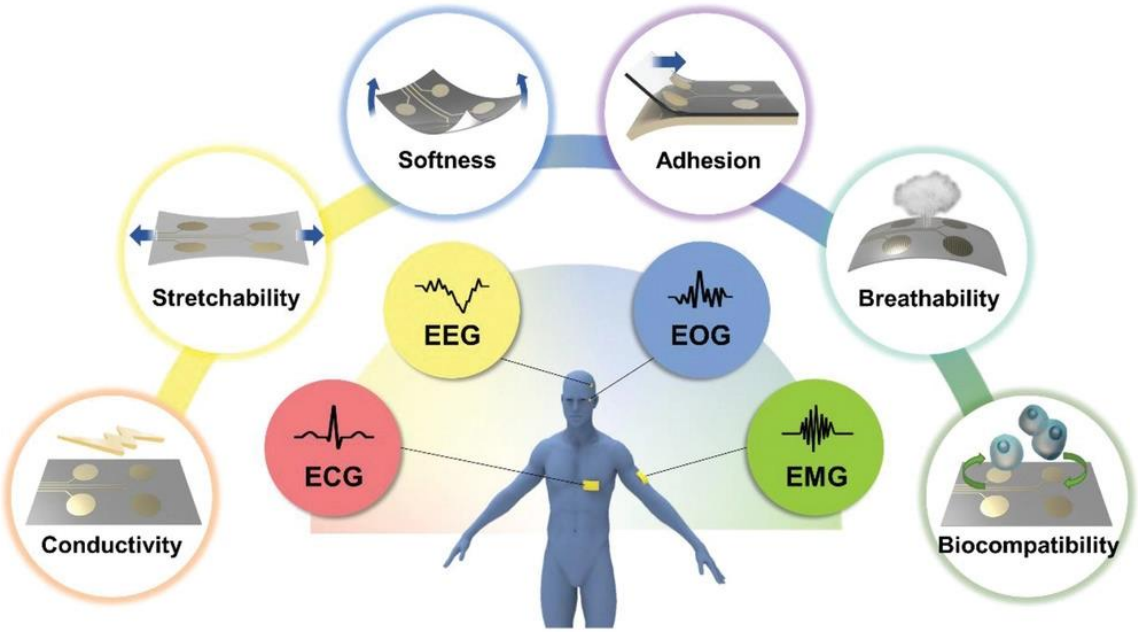

Figure 2.10 The desired on-skin electrodes properties for biopotential signal measurements. The electrodes need to be conductive for signal transduction, stretchable for skin deformation, soft for skin modulus match, adhesive for intact skin attachment, breathable for skin gas exchange, and biocompatible without skin damage. Figures reproduced from Ref[22].

In the design of the conformal skin bioelectrodes, stretchability is the most important parameter[23]. Stretchability defines the ability of the material to deform while keeping its conductivity. Rational structural design can realize high stretchability which is not intrinsically stretchable. Several representative structures have developed as highly stretchable conductors. The principles of these designs are also applicable to stretchable bioelectrodes. The first type of stretchable structure is the serpentine structure[24, 25]. The serpentine structure is made from a high amplitude in-plane sinusoidal wave of conductive traces (Figure 2.11 top). When stretched, it will undergo an out-of-plane deformation. Strains are mostly accommodated by the out-of-plane flattening of sine waves. As such, it is much more stretchable than the straight line. The materials to make the serpentine structure are usually copper and polyimide substrate, but other conductive materials are

also applicable. The serpentine structure can achieve very high stretchability (>1600%). However, it faces a series of problems. The adhesion between serpentine structure and substrate elastomer may limit the out-of-plane deformation. In addition, the out-of-plane deformation may also limit the skin conformability. The second stretchable structure is the mesh structure[26, 27]. This structure is inspired by a stretchable Kirigami structure that exceeds 1100%. A stretchable mesh structure can be fabricated by electrospinning of polyvinyl alcohol (PVA) (Figure 2.11 middle). By thermal evaporating Au onto PVA fibers then dissolving PVA fiber, Au mesh conductor can be fabricated. This mesh conductor can be very conductive on the skin and can work as skin bioelectrodes to measure EMG signals. Most importantly, it is breathable and causes no inflammation to the skin, which is a superior choice for bioelectrodes. The third most important stretchable conductor is the Au microcrack structure[28]. Microcrack is formed by stretching Au and PDMS elastomer, due to the mismatch between PDMS and Au Young's modulus, Au nanofilm will crack perpendicular to the direction of stretching. The microcrack will contribute to the stretchability of the Au nanofilm but the interconnection still exists, enduring its conductivity. Increasing the rate of Au evaporation can boost the stretchability of the Au nanofilm conductor (Figure 2.11 bottom). The sheet resistance of a 40 nm Au nanofilm on PDMS is as low as 11.8 Ω $Sq.^{-1}$ at 0% strain and only increased to 33.3 Ω $Sq.^{-1}$ at 120% strain. The stretchability of Au nanofilm on PDMS can be further increased by pre-stretching the PDMS substrate.

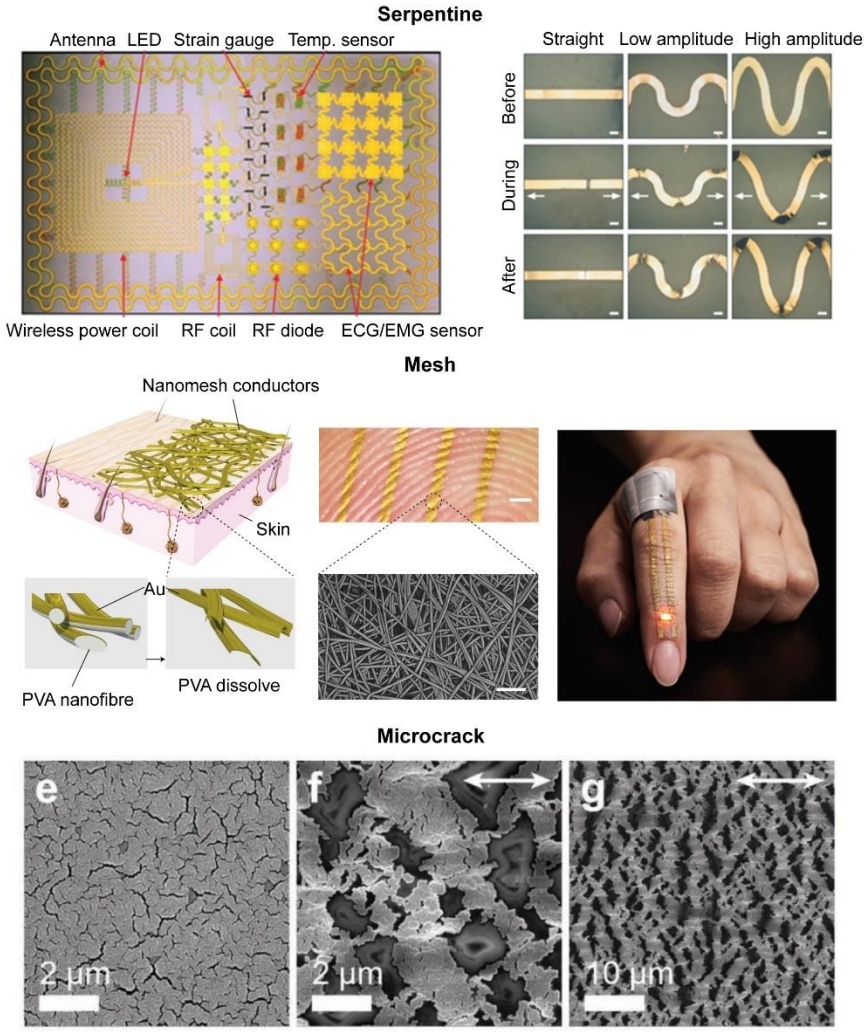

Figure 2.11 Structures for stretchable conductors. The state-of-the-art structural design can be classified as serpentine structure (top, reproduced from Ref, mesh structure, and microcrack nanofilm structure. Figures reproduced from Ref[24, 26, 28, 29]

The electrode system for an on-skin application can be a wet electrode (with electrolyte gel or hydrogel[30]), or a dry electrode (only conductive metal, without electrolyte[31]). For dry electrodes, sweat serves as the electrolyte. Wet electrode gives better ionic conductivity and skin-contacting, thus resulting in better signal quality. A dry electrode is better in gas permeability, longer wearable time, and thinner electrode pattern. Chemically crosslinked hydrogel with ionic additive is a widely used solid electrolyte for bioelectrode application. It has tunable mechanical properties such as a Young's modulus smaller than skin (<0.5 MPa), high elasticity and super-stretchability (>500%). Furthermore, its conductivity can

be modified by addition of conductive fillers or salts. Hydrogel as electrolyte also need an electronic conductor to convert the ionic current into electronic current. Hydrogel-metal nanofilm-elastomer substrate is a classic structure for a hydrogel-based bioelectrode. The bonding between hydrogel ionic conductor and metal nanofilm-elastomer substrate is always a challenge. Chemically modifying the Ti-Au-Ti nanofilm substrate with 3-(trimethoxysilyl) propyl methacrylate can enhance the bonding between the tough hydrogel and Ti nanofilm (Figure 2.12 top)[32]. Stretchable metal nanofilm on elastomer substrate can also be directly applied onto skin as dry electrodes[31]. Skin will easily sweat under the coverage of a non-permeable metal nanofilm-elastomer substrate, contributing to the ionic conductive electrolyte interfacing with the metal nanofilm. The biggest issue is the weak bonding between the metal nanofilm and elastomer substrate. The metal nanofilm would be easily erased off when in contacting with skin, deteriorating the electrical conductivity of the electrode. Strong bonding can be achieved by interface engineering between metal nanofilm and elastomer substrate. For example, a highly stable, stretchable, and conductive Au nanofilm on a PDMS substrate can be obtained by a thermal radiation-assisted metal encapsulation, in which Au is thermally evaporated onto a half-cured PDMS film (Figure 2.12 middle)[31]. PDMS film fully cures during the thermal evaporation process. With Au atoms partially embedded into the PDMS film, there is an interfacial diffusion layer between Au nanofilm and PDMS substrate, achieving high interfacial bonding between Au nanofilm and PDMS substrate. Another strategy for developing electrolytes in contact with skin is to modify protein materials as natural hydrogels. The benefits of protein materials include their biocompatibility towards human skin application, rich resources, and eco-friendly. Silk fibroin is a superior materials candidate in flexible electronics due to its flexibility, high water content, and ionic conductivity. By plasticizing silk fibroin with Ca^{2+} ions, it can be modified into a hydrogel with high stretchability (>400%) and low Young's modulus (0.1 – 1 MP). Evaporating a layer of Au nanofilm onto the silk fibroin film, a biocompatible silk fibroin electrode can be fabricated (Figure 2.12 bottom). Silk fibroin hydrogel serves as an electrolyte layer for the electrode. It shows no inflammation reaction on the skin[21].

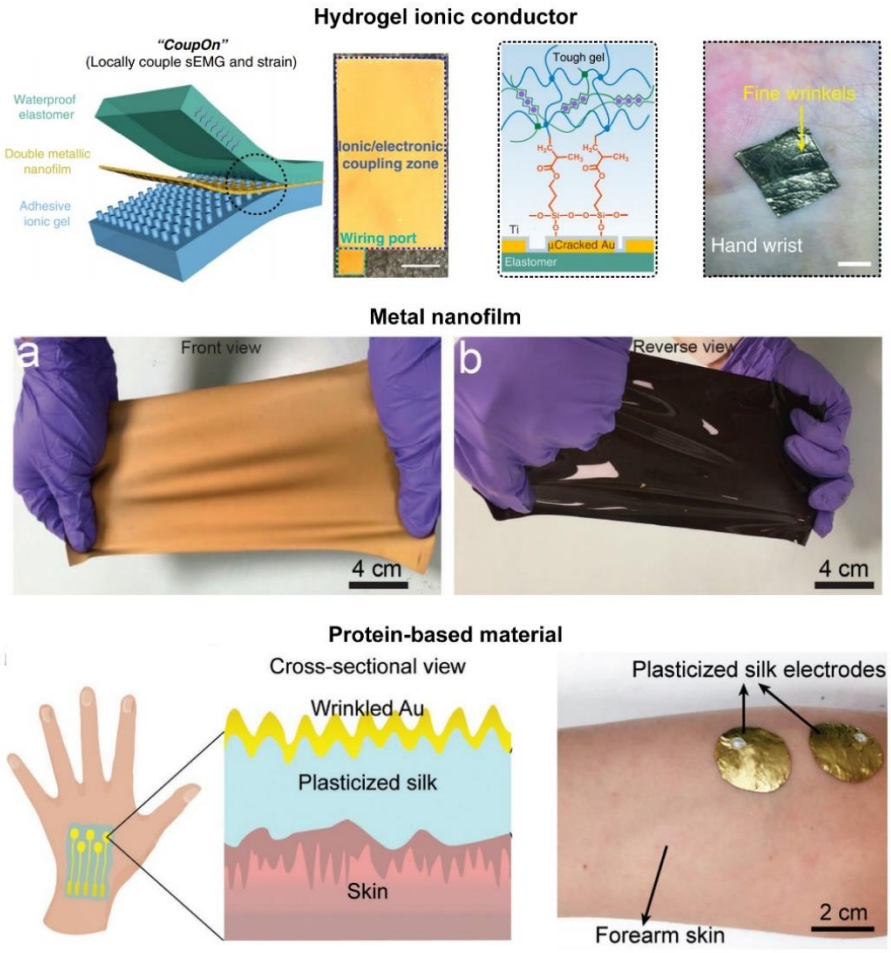

Figure 2.12 Materials design of stretchable, conductive, and soft on-skin bioelectrodes. Hydrogel, a crosslinked polymer containing more than 90% of water, is a widely used ionic conductor in contact with the skin. Metal nanofilms that are stretchable can also be directly applied to the skin as bioelectrodes. Protein-based materials (silk fibroin) crosslinked by ions can work as a biocompatible ionic conductor for on-skin bioelectrodes. Figures reproduced from Ref[21, 31, 32]

2.7 Electrode array

The single skin bioelectrode constructed from hydrogel-metal nanofilm-elastomer substrate structure or metal nanofilm-elastomer substrate can only measure one point on the skin. Due to the relatively large size of the electrode (>3 mm), the measured signal reflects a summed average of the biopotential signal beneath the skin. There is another very important case that the spatial-temporal information about the biopotential is needed. In this case, the electrode array is needed. The fabrication of an electrode array is more

difficult than a single electrode as all the electrode units need to be stretchable and conductive simultaneously. The conductive path is usually narrow as the electrode density goes high, which would increase the resistance of the conductive path. For the electrode array with multiple electrodes that need to be measured, each electrode needs a conductive path to the amplifier device. The way to address each electrode unit can be classified as an active matrix or passive matrix[33]. In the active matrix, each electrode unit relates to a transistor (Figure 2.13 left)[34]. This transistor acts as a switch to control the addressing of the electrode. There are two types of wires connecting the electrode units, one is called word line (also called selector), and the other is called bit line (also called data line). The selector line is to give control voltage to the transistors. When high voltage is given to a word line, the transistors with gates connected to this line will be switched on, electrodes connecting with these transistors can be readout. By scanning word lines one by one, electrodes can be scanned row by row. The benefit of the active matrix is that each time only one row of electrodes is read, reducing the crosstalk between different signal lines. And the number of wirings is also reduced. The disadvantage of the active matrix is that each electrode requires one transistor (or even more than one), which is very complicated to fabricate. The passive matrix electrode is much simpler (Figure 2.13 right). Each electrode unit relates to one conductive trace. Electrical signals from each electrode are read simultaneously. The disadvantage of such an electrode array is that all the signal lines need to be read at the same time, giving rise to high crosstalk. The number of wirings is also higher than an active matrix.

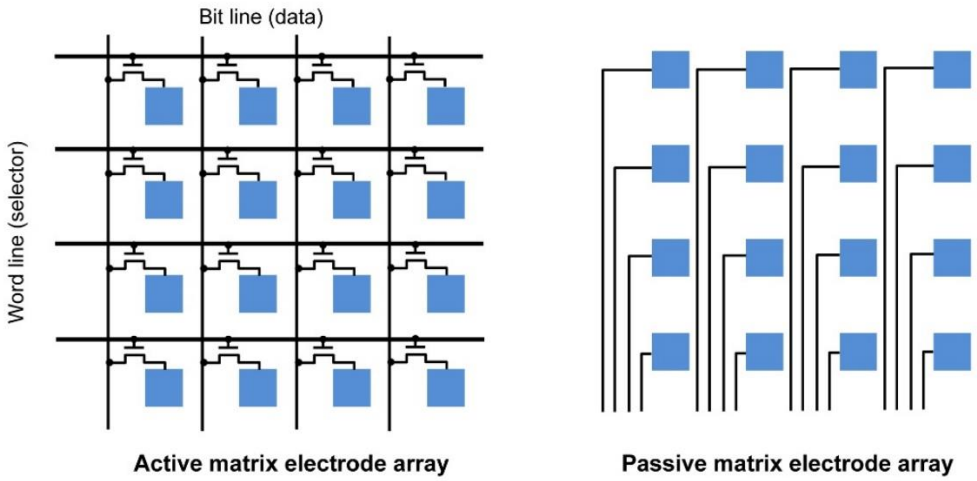

Figure 2.13 Electrode array technologies. The array technologies include active-matrix array or passive matrix. Active-matrix array requires one transistor as a switch for each electrode, it reduces the number of wirings. Passive-matrix requires one wire for each electrode, it is easier to develop but the number of wiring increases with electrode numbers.

The flexible active-matrix electrode array is widely fabricated on polyimide film (Figure 2.14a-c)[35]. Usually, the number of transistors is more than one for each electrode unit to realize high selectivity of the electrode unit and amplification of the signal. However, due to the fabrication complexity, the active-matrix electrode array is mostly fabricated on polyimide, which is not able to be stretched. In contrast, passive electrode arrays can be fabricated on a stretchable substrate, which increases their applicability on deformable tissues or skin (Figure 2.14 d-f)[36, 37].

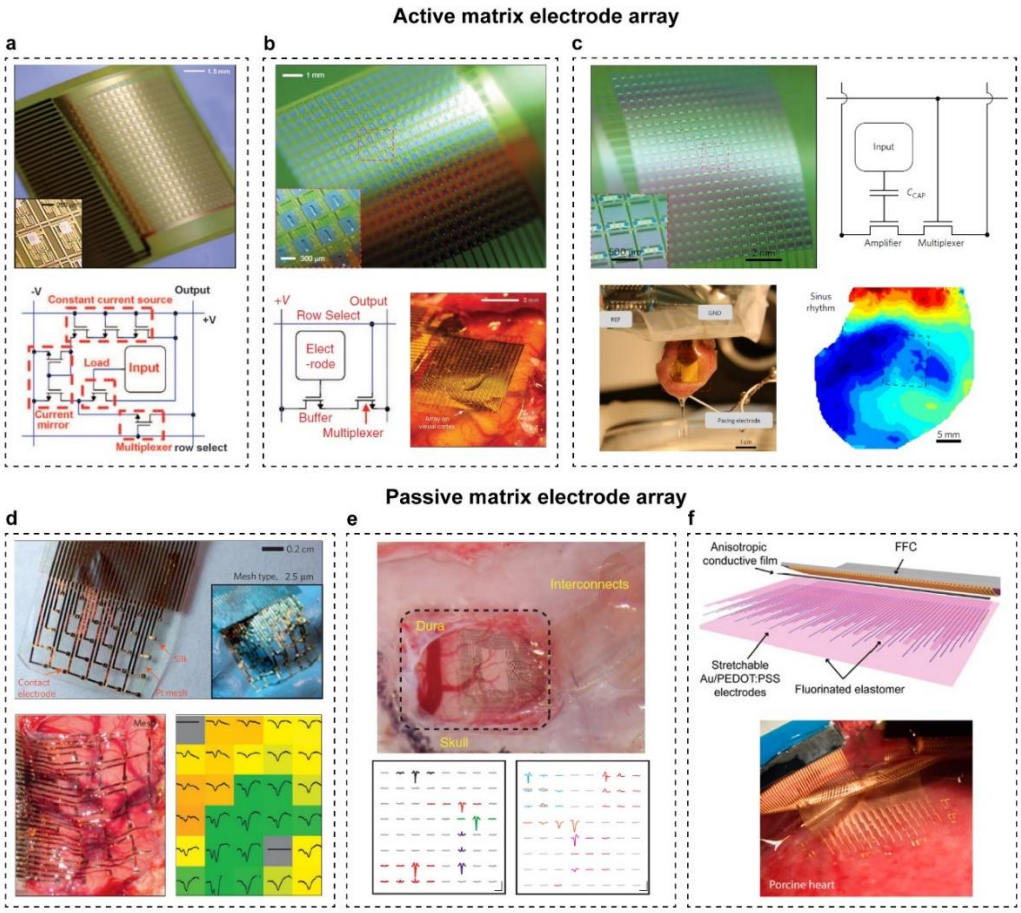

Figure 2.14 Flexible electrode array devices. The electrode array can be classified as an active-matrix array and a passive matrix array. The active-matrix array (a-c) has transistors as a controlling unit for each electrode point. Due to complexity, the electrode is only flexible and difficult to make stretchable. The passive-matrix array (d-e) requires no transistors and only a conductive path for signal transmission. The passive array can be made very soft and stretchable due to the simplicity of the circuit. Figures reproduced from Ref[35, 36]

References

[1] J. G. Webster, *Medical Instrumentation: Application and Design*, WILEY, 2010.

[2] D. J. Aidley, *The Physiology of Excitable Cells*, Cambridge University Press, 1998.

[3] R. Fitzhugh Journal of General Physiology 1960, 43, 867.

[4] https://www.sciencelearn.org.nz/images/2357-types-of-muscle-tissue, 2007.

[5] C. Feng, K. Liu, J.-S. Wu, L. Liu, J.-S. Cheng, Y. Zhang, Y. Sun, Q. Li, S. Fan, K. Jiang, Advanced Functional Materials 2010, 20, 885.

[6] http://droualb.faculty.mjc.edu/Course%20Materials/Physiology%20101/Chapter%20Notes/Fall%202007/chapter_7%20Fall%202007.htm, 2020.

[7] F. Su, B. Deng, H. Li, S. Yang, Y. Qin, J. Wang, C. Liu, International Journal of Modern Physics B 2017, 31, 1750238.

[8] F. Greco, A. Zucca, S. Taccola, B. Mazzolai, V. Mattoli, ACS Appl Mater Interfaces 2013, 5, 9461.

[9] F. Xu, Y. Zhu, Adv Mater 2012, 24, 5117.

[10] S. Okutucu, A. Oto, in *Interpreting ECGs in Clinical Practice*, (Eds: S. Okutucu, A. Oto), Springer International Publishing, Cham 2018, 1.

[11] G. Buzsáki, C. A. Anastassiou, C. Koch, Nature Reviews Neuroscience 2012, 13, 407.

[12] T. Kirschstein, R. Köhling, Clinical EEG and Neuroscience 2009, 40, 146.

[13] M. Le Van Quyen, New Ideas in Psychology 2011, 29, 57.

[14] T. Ros, B. J. Baars, R. A. Lanius, P. Vuilleumier, Frontiers in Human Neuroscience 2014, 8.

[15] J. Jung, H. Lee, I. Ha, H. Cho, K. K. Kim, J. Kwon, P. Won, S. Hong, S. H. Ko, ACS Appl Mater Interfaces 2017, 9, 44609.

[16] A. Del Vecchio, A. Holobar, D. Falla, F. Felici, R. M. Enoka, D. Farina, Journal of Electromyography and Kinesiology 2020, 53, 102426.

[17] B. You, Y. Kim, B. K. Ju, J. W. Kim, ACS Appl Mater Interfaces 2017, 9, 5486.

[18] L. Cai, J. Li, P. Luan, H. Dong, D. Zhao, Q. Zhang, X. Zhang, M. Tu, Q. Zeng, W. Zhou, S. Xie, Advanced Functional Materials 2012, 22, 5238.

[19] Y. Zhang, C. J. Sheehan, J. Zhai, G. Zou, H. Luo, J. Xiong, Y. T. Zhu, Q. X. Jia, Adv Mater 2010, 22, 3027.

[20] Ø. G. M. Sverre Grimnes, *Bioimpedance and Bioelectricity Basics, 3rd Edition*, Elsevier, 2015.

[21] G. Chen, N. Matsuhisa, Z. Liu, D. Qi, P. Cai, Y. Jiang, C. Wan, Y. Cui, W. R. Leow, Z. Liu, S. Gong, K.-Q. Zhang, Y. Cheng, X. Chen, Advanced Materials 2018, 30, 1800129.

[22] H. Wu, G. Yang, K. Zhu, S. Liu, W. Guo, Z. Jiang, Z. Li, Advanced Science 2021, 8, 2001938.

[23] S. Huang, Y. Liu, Y. Zhao, Z. Ren, C. F. Guo, Advanced Functional Materials 2019, 29, 1805924; M.-S. Lee, K. Lee, S.-Y. Kim, H. Lee, J. Park, K.-H. Choi, H.-K. Kim, D.-G. Kim, D.-Y. Lee, S. Nam, J.-U. Park, Nano Letters 2013, 13, 2814.

[24] D.-H. Kim, N. Lu, R. Ma, Y.-S. Kim, R.-H. Kim, S. Wang, J. Wu, S. M. Won, H. Tao, A. Islam, K. J. Yu, T.-i. Kim, R. Chowdhury, M. Ying, L. Xu, M. Li, H.-J. Chung, H. Keum, M. McCormick, P. Liu, Y.-W. Zhang, F. G. Omenetto, Y. Huang, T. Coleman, J. A. Rogers, Science 2011, 333, 838.

[25] S. Wang, M. Li, J. Wu, D.-H. Kim, N. Lu, Y. Su, Z. Kang, Y. Huang, J. A. Rogers, Journal of Applied Mechanics 2012, 79; W.-H. Yeo, Y.-S. Kim, J. Lee, A. Ameen, L. Shi, M. Li, S. Wang, R. Ma, S. H. Jin, Z. Kang, Y. Huang, J. A. Rogers, Advanced Materials 2013, 25, 2773.

[26] A. Miyamoto, S. Lee, N. F. Cooray, S. Lee, M. Mori, N. Matsuhisa, H. Jin, L. Yoda, T. Yokota, A. Itoh, M. Sekino, H. Kawasaki, T. Ebihara, M. Amagai, T. Someya, Nature Nanotechnology 2017, 12, 907.

[27] W. Zhou, Y. Li, P. Li, J. Chen, R. Xu, S. Yao, Z. Cui, R. Booth, B. Mi, D. Wang, Y. Ma, W. Huang, Advanced Materials Technologies 2019, 4, 1800698.

[28] N. Matsuhisa, Y. Jiang, Z. Liu, G. Chen, C. Wan, Y. Kim, J. Kang, H. Tran, H.-C. Wu, I. You, Z. Bao, X. Chen, Advanced Electronic Materials 2019, 5, 1900347.

[29] D. S. Gray, J. Tien, C. S. Chen, Advanced Materials 2004, 16, 393.

[30] J. Deng, H. Yuk, J. Wu, C. E. Varela, X. Chen, E. T. Roche, C. F. Guo, X. Zhao, Nature Materials 2021, 20, 229.

[31] Z. Liu, H. Wang, P. Huang, J. Huang, Y. Zhang, Y. Wang, M. Yu, S. Chen, D. Qi, T. Wang, Y. Jiang, G. Chen, G. Hu, W. Li, J. Yu, Y. Luo, X. J. Loh, B. Liedberg, G. Li, X. Chen, Advanced Materials 2019, 31, 1901360.

[32] P. Cai, C. Wan, L. Pan, N. Matsuhisa, K. He, Z. Cui, W. Zhang, C. Li, J. Wang, J. Yu, M. Wang, Y. Jiang, G. Chen, X. Chen, Nature Communications 2020, 11, 2183.

[33] W. Lee, T. Someya, Chemistry of Materials 2019, 31, 6347.

[34] H. Shim, K. Sim, F. Ershad, S. Jang, C. Yu, Journal of Materials Chemistry C 2020, 8, 10719.

[35] J. Viventi, D.-H. Kim, J. D. Moss, Y.-S. Kim, J. A. Blanco, N. Annetta, A. Hicks, J. Xiao, Y. Huang, D. J. Callans, J. A. Rogers, B. Litt, Science Translational Medicine 2010, 2, 24ra22; J. Viventi, D.-H. Kim, L. Vigeland, E. S. Frechette, J. A. Blanco, Y.-S. Kim, A. E. Avrin, V. R. Tiruvadi, S.-W. Hwang, A. C. Vanleer, D. F. Wulsin, K. Davis, C. E. Gelber, L. Palmer, J. Van der Spiegel, J. Wu, J. Xiao, Y. Huang, D. Contreras, J. A. Rogers, B. Litt, Nature Neuroscience 2011, 14, 1599; H. Fang, K. J. Yu, C. Gloschat, Z. Yang, E. Song, C.-H. Chiang, J. Zhao, S. M. Won, S. Xu, M. Trumpis, Y. Zhong, S. W. Han, Y. Xue, D. Xu, S. W. Choi, G. Cauwenberghs, M. Kay, Y. Huang, J. Viventi, I. R. Efimov, J. A. Rogers, Nature Biomedical Engineering 2017, 1, 0038.

[36] D.-H. Kim, J. Viventi, J. J. Amsden, J. Xiao, L. Vigeland, Y.-S. Kim, J. A. Blanco, B. Panilaitis, E. S. Frechette, D. Contreras, D. L. Kaplan, F. G. Omenetto, Y. Huang, K.-C. Hwang, M. R. Zakin, B. Litt, J. A. Rogers, Nature Materials 2010, 9, 511; J. Liu, X. Zhang, Y. Liu, M. Rodrigo, P. D. Loftus, J. Aparicio-Valenzuela, J. Zheng, T. Pong, K. J. Cyr, M. Babakhanian, J. Hasi, J. Li, Y. Jiang, C. J. Kenney, P. J. Wang, A. M. Lee, Z. Bao, Proceedings of the National Academy of Sciences 2020, 117, 14769; D. Khodagholy, J. N. Gelinas, T. Thesen, W. Doyle, O. Devinsky, G. G. Malliaras, G. Buzsáki, Nature Neuroscience 2015, 18, 310.

[37] A. Vázquez-Guardado, Y. Yang, A. J. Bandodkar, J. A. Rogers, Nature Neuroscience 2020, 23, 1522.

Chapter 3

Experimental Methodology

This chapter introduces the rationales of materials synthesis, characterization techniques, and on-skin biopotential signal measurements related to the conformal electrodes. The principles of materials and characterizations are elaborated with the implementation details in the project. In particular, the synthesis of the adhesive chemical hydrogel as an ionic conductor, stretchable Au nanomesh as an electronic conductor is elaborated. These two types of materials form the core of electrode components. Next, the characterization of the materials and electrode devices with their principles are introduced. The characterization is important in understanding and optimization of the properties of the materials. The interface properties of the conformal electrode on different surfaces with microstructures are also presented. Lastly, the details of different biopotential measurements are introduced.

3.1 Rationale for selection

Hydrogels, chemically or physically cross-linked polymer containing rich water content, which can exceed more than 90% (Figure 3.1)[1]. Some hydrogel materials have promising adhesive and ionically conductive properties, such as polyacrylamide (PAAM) hydrogel[2] and polyacrylic acid (PAA) hydrogel[3]. These hydrogel materials can be used as electrolyte gel layers in conformal electrodes. PSA is one of the most used adhesives in consumer and medical applications[4, 5]. It is a transparent coating layer with controllable adhesiveness. After evaporating the solvent, the adhesive layer will remain as a thin film coating. It is noted that PSA is not conductive on its own. When working as an electrode coating layer, further engineering strategies are needed to endow the coating layer with desired conductivity. PDMS is a silicone rubber widely used as a stretchable substrate for conductive electrodes[6]. It is prepared by mixing two parts together, one is a base, and the other is a curing agent. PDMS has a Young's modulus of around 1 – 10 MPa and a stretchability of around 150%. It also has high optical transparency. Au nanofilm can be evaporated onto the PDMS substrate using a thermal evaporation method. A mask can be applied on top of PDMS film to define desired patterns of Au nanofilm. Au nanomesh is a fractal network which are interconnected to form 2D conductors. It maintains some transparency and stretchability, which is superior for electrode applications.

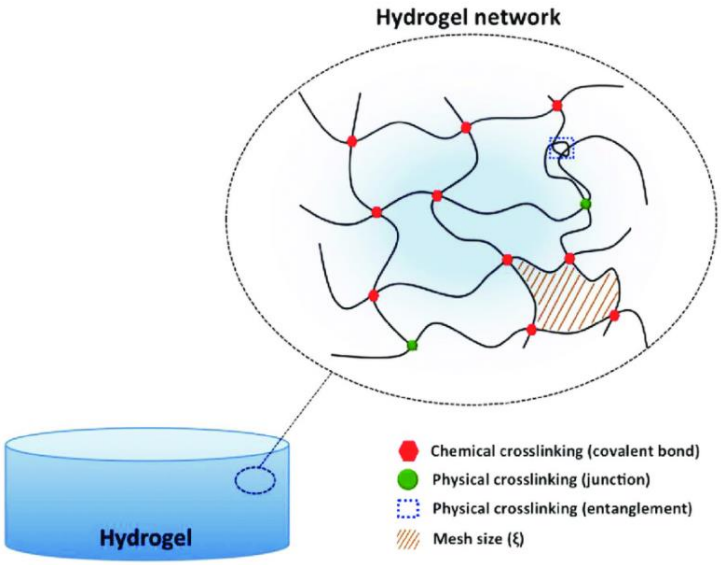

Figure 3.1 Schematic of a hydrogel and its network structure. Hydrogels can be prepared in a bulk or thin-film form. It is composed of 3D interconnected polymer chains. The polymer chains are hydrophilic in that they can contain a large amount of water (more than 90% of its weight). The polymer chains are connected by chemical crosslinking (covalent bond) or physically crosslinking (non-covalent bond). Figure reproduced from Ref[3].

3.2 Synthesis of adhesive hydrogel

Hydrogel synthesis includes the formation of a 3D network of hydrophilic structures which allows them to keep a large amount of water. Hydrogel synthesis involves a polymerization process that joins monomers into long polymer chains and a cross-linking process that connects different polymer chains [7]. Monomers are the most important starting material as they will decide the properties of the final hydrogel network. For adhesive hydrogel synthesis, the most used monomers are acrylic acid and acrylamide due to their ease of polymerization, biocompatibility, transparency, and high adhesiveness. For the polymerization and cross-linking reactions, the monomers need to be mixed with a cross-linking agent in a water solution. The polymerization process can be initiated thermally (thermal initiator and UV initiator), or by a redox initiator. Accelerators can be added to increase the rate of polymerization. Cross-linker is also needed to cross-link different polymer chains. The cross-linking can be a covalent bond or physical bond.

The synthesis of polyacrylic acid hydrogel is one typical example of free-radical polymerization (Figure 3.2). The solution polymerization of acrylic acid is usually initiated by a thermal initiator such as potassium persulfate or ammonium persulfate, with the presence of a water-soluble cross-linker methylene bis-acrylamide. The schematic of such hydrogel synthesis is shown below.

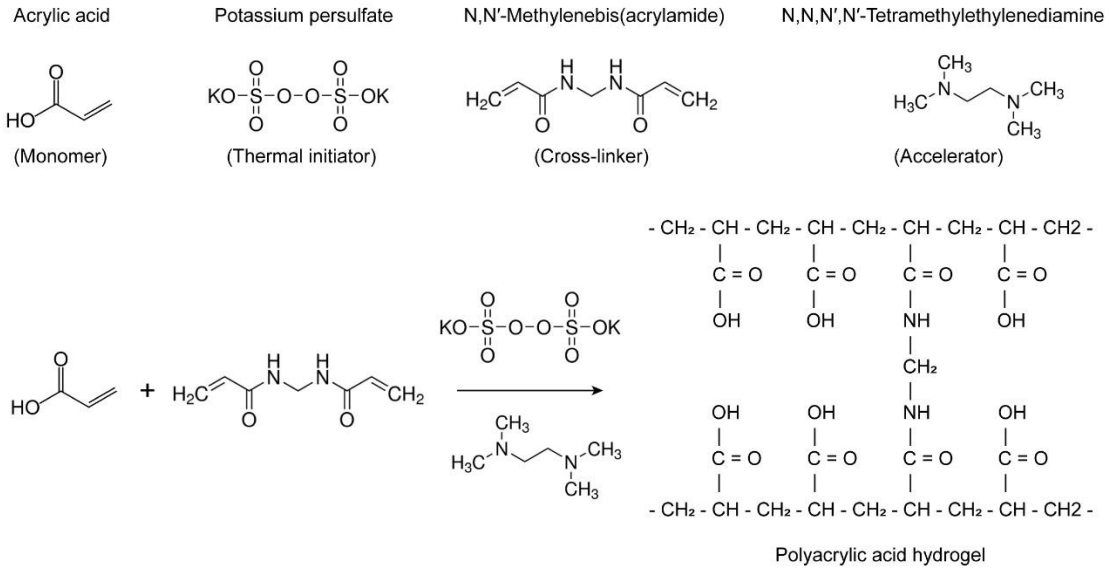

Figure 3.2 Chemical recipes used in the synthesizing of the adhesive polyacrylic acid hydrogel. Acrylic acid is a monomer that will undergo free radical polymerization to form polymers. Potassium persulfate is a thermal initiator to initiate free radical polymerization. N,N'-Methylenebis(acrylamide) is the cross-linker that forms covalent bonds with polyacrylic acid polymer chains. N,N,N',N'-Tetramethylethylenediamine is the accelerator to increase the reaction rate of the polymerization. The final polyacrylic acid hydrogel is an interconnected polyacrylic acid polymer network[7].

3.3 Synthesis of Au nanomesh

The synthesis of Au nanomesh conductor materials is based on Au crystal growth and self-assembly. This template-less and room temperature method allows the formation of Au nanomesh films on the water surface (Figure 3.3)[8, 9]. Au nanoparticles are firstly obtained in an aqueous solution by reducing $HAuCl_4$ using $NaBH_4$. Toluene is added to the aqueous

solution with stirring. The reduced Au will form Au nanoparticles. Under vigorous stirring, the Au nanoparticles are coated with a layer of toluene. After removing toluene, the Au nanoparticle would float on the water surface, further assembly into nanowires and interconnected nanomesh. The interconnected nanowires provide a pathway for electronic transportation, making it a suitable conductive layer. The hollow structure of the nanowires allows light transmission, providing optical transparency. There is no template and surfactant used in such synthesizing process. After evaporating toluene, Au nanowires expose their conductive surfaces with each other, improving the conductivity of the film. No further annealing processes are needed for the Au nanomesh film.

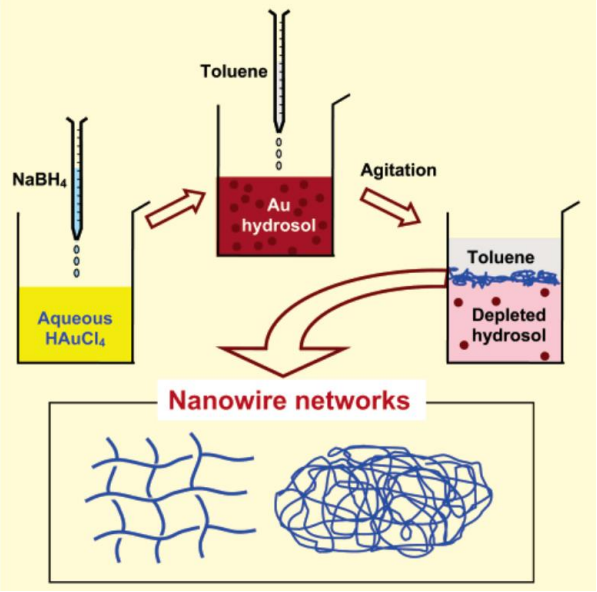

Figure 3.3 Schematic of Au nanomesh synthesis. Au nanoparticles are firstly obtained in an aqueous solution by reducing $HAuCl_4$ using $NaBH_4$. Then adding toluene and vigorous agitation result in the formation of Au nanowires and a layer of mesh on the toluene water interface. Figures reproduced from Ref[8].

3.4 PSA coating on stretchable conductors and bioelectrodes

Water-based PSAs are typically based on acrylic adhesive polymers synthesized from vinyl acrylic monomers[5]. The acrylic PSAs are usually made from a blend of monomer components[4]. Based on their glass transition temperature, the monomers can be classified

as soft, medium, hard, and functional monomers (Table 3.1). Polymers from soft monomers have a T_g below -30 ºC. Polymers from hard monomers have a T_g above 30 ºC. Those with T_g in between are called medium monomers. A PSA recipe contains mostly soft monomers that give it viscous properties. Hard monomers are added in a small amount to increase the cohesive properties of the adhesive. Functional monomers are also added to provide charge and functional groups for the polymer to be cross-linked. The most seen soft, medium, and hard monomers can be seen from the table below. The ready-to-use PSA solution usually includes colloidal particles. By spreading the PSA solution on the desired coating surface and allowing water evaporation, an adhesive film would be coated on the desired surface. It should be noted that the coating surface needs to be hydrophilic for PSA solution spreading, for hydrophobic surface, a plasma treatment is needed to functionalize a layer of hydroxyl groups on the desired surface.

Table 3.1 Commonly used monomers in water-soluble PSAs.

Soft monomers		**Functional monomers**	
n-Butyl Acrylate	2-Ethylhexyl acrylate	Methacrylic acid	Acrylic acid
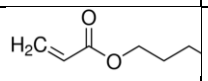	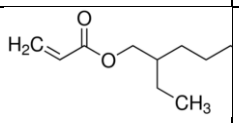	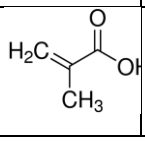	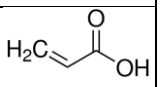
Medium monomers		**Hard monomers**	
Ethyl acrylate	Butyl methacrylate	Methyl methacrylate	Vinyl acetate
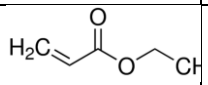	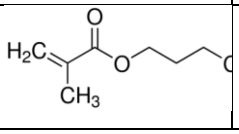	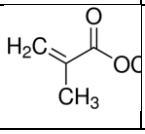	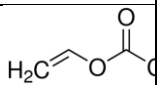

3.5 Characterization of the adhesive hydrogel

The as-prepared adhesive hydrogels need to go through a series of characterization to verify their electrical, mechanical, optical, and biocompatible properties. Hydrogel optimization also depends on the characterized properties. For the electrical properties, as the hydrogel

is an ionic conductor, it cannot be directly measured using an Ohmmeter, instead, electrochemical impedance is needed to characterize the conductivity of the hydrogel. For the mechanical properties, the peeling off adhesive strength is measured and analyzed, due to the safety issue of directly measuring adhesive hydrogel on human skin under a mechanical tester, plant leaves can be used as an alternative to replace human skin for this characterization. Similarly, when it is risky to directly measure certain properties on human skin, a plant surface can be a good alternative for material property evaluation. Moreover, as an important parameter, Young's modulus of the hydrogel can be characterized by a stress-strain test using a mechanical tester.

3.5.1 Electrical property of the adhesive hydrogel

The electrical property of adhesive hydrogel is primarily characterized by electrochemical impedance spectroscopy (EIS) which can be conducted on an electrochemical workstation. The EIS can be measured in a three-electrode system, including a counter electrode (CE), a reference electrode (RE), and a working electrode (WE) (Figure 3.4a). The potential signal is provided between WE and RE, while the resulting current can be measured between CE and RE. The potential signal is a perturbation signal, and the measured current signal is called a response signal. In the practical application, the perturbation signal is usually a continuous sine wave with changing frequencies from high frequency to low frequency (Figure 3.4b). In the electrode system, the current response of this perturbation signal should be measured in a linear domain, which indicates that a proper DC offset is needed besides the small perturbation signal (Figure 3.4c). The relationship between the perturbation signal and the response signal can be reflected as a very important parameter, which is called impedance. The impedance Z can be expressed as[10]:

$$Z(\omega) = \frac{\tilde{V}(\omega)}{\tilde{I}(\omega)} = \left|\frac{\tilde{V}(\omega)}{\tilde{I}(\omega)}\right| (cos\phi(\omega) + jsin\phi(\omega)) = Z_r + jZ_j$$

Where ω is the angular frequency, ϕ is the phase angle between the input and output signals. From the equation above impedance is a complex number and is a function of the input

frequency. The real impedance Z_r is a frequency-dependent resistance and the imaginary part Z_j is a frequency-dependent reactance. The measured impedance can be reflected as the Nyquist plot or Bode plot (Figure 3.4d). In the Nyquist plot, the Z_j is plotted against Z_r. In the Bode plot, the modulus impedance and the phase angle are plotted against input frequency. The impedance result can be further interpreted as an equivalent circuit model, which can be used to fit the Nyquist plot or Bode plot (Figure 3.4e).

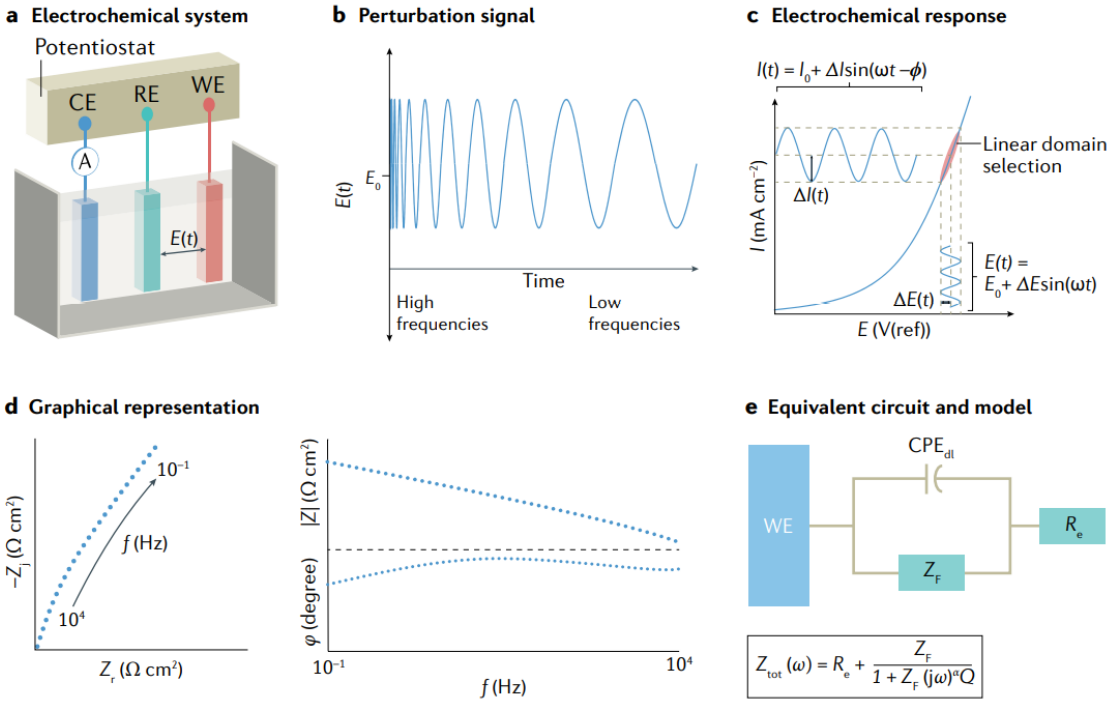

Figure 3.4 Working principle of electrochemical impedance spectroscopy (EIS). (a) Setup of an electrochemical system. The measurement needs three electrodes: working electrode (WE), reference electrode (RE), and counter electrode (CE). A current stimulus is given between CE and RE, while the potential signal is measured between RE and WE. (b) Schematic of a perturbation signal. It can be a current signal or a voltage signal. It is a continuous sine waveform with changing frequencies. (c) Schematic of a relationship between perturbation voltage signal and response current signal. The perturbation signal needs to be located at a linear region. (d) Nyquist plot and Bode plot of the measured EIS result. (e) equivalent circuit model to interpret the resultant Nyquist plot or Bode plot. Figure reproduced from Ref[10].

In the EIS characterization, impedance was measured in two-electrode form. One electrode pair serves as both stimulating electrodes (the perturbation signal) and response signal sensing electrodes (the response current). Such a two-electrode EIS system can be used to characterize three application scenarios. One is to measure the resistance of an electronic conductor, such conductor can be made of Au nanomesh, evaporated Au nanofilm, AgNW on PDMS substrate (Figure 3.5 top left). The second application is to characterize the impedance of hydrogel and hydrogel-electrode interface. The basic configuration is an electrode-hydrogel-electrode sandwich structure (Figure 3.5 top right). The total impedance is composed of two electrode impedances, one hydrogel impedance, and two electrode-hydrogel impedances. The most significant contribution is from the electrode-hydrogel interface impedance. The third application is to apply two hydrogel electrodes onto the skin and measure impedance (Figure 3.5 bottom). The configuration is mainly to characterize the hydrogel-skin interface impedance as this part contributes most of the impedances of the system. Caution must be taken when measuring human skin as this will connect the human body with electrical instruments. Plant surfaces can be used as an alternative biological surface to replace human skin in some circumstances.

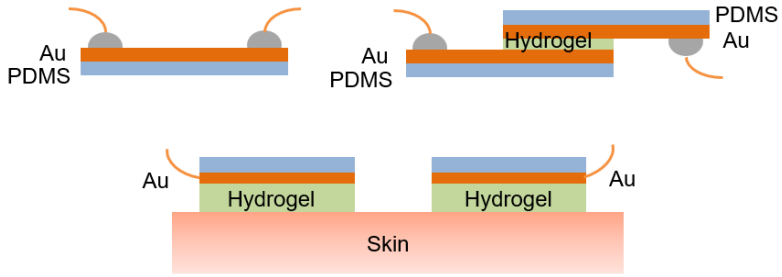

Figure 3.5 Three configurations of skin bioelectrode characterization in EIS system. The measurement is conducted in a two-electrode system. The electronic conductive of an Au-PDMS electrode can be characterized by measuring impedance from its two ends (top left). The Au-PDMS electrode with hydrogel interface can be characterized by a sandwich structure (top right), where each end of the electrode is connected to the electrochemical system. The electrode-skin interface can be characterized by measuring the impedance of two electrodes on the skin (bottom).

3.5.2 Mechanical property of the adhesive hydrogel

The synthesized polyacrylic acid hydrogel is a highly stretchable and adhesive material. The stretchability and adhesiveness can be characterized by a mechanical tester. Stretchability and Young's modulus can be measured from a stress-strain test. Stretchability reflects the total strain that the hydrogel can withstand before the break. Young's modulus is a mechanical property reflecting how easily the material can be stretched or compressed under a stress. Young's modulus can be quantified in a linear region of a materials stress-strain curve as:

$$E = \frac{\sigma}{\varepsilon}$$

Where σ is the tensile stress and ε is the axial strain. In the measurement of Young's modulus, a hydrogel film was fixed on two fixation clippers of a mechanical tester. The mechanical tester is set to a constant strain rate, that is, the hydrogel will be stretched by a constant rate. The stress to sustain such strain rate is measured. And stress-strain curves can be plotted.

The adhesiveness can be quantified from a 90-degree peeling experiment[11]. The surface to be studied needs to be fixed on a platter. The hydrogel needs to be fixed on a flexible but not stretchable backing layer (Figure 3.6). This is to ensure the force measured by the mechanical tester is from peeling the interface rather than stretching the hydrogel itself. During the measurement, half of the hydrogel film is adhered to the studied surface, while the other end is fixed on a clipper in the mechanical tester. The hydrogel is peeled from the studied surface at a constant rate, the force needed to sustain such rate is measured. The plateau force divided by the width of the hydrogel film is noted as adhesive strength.

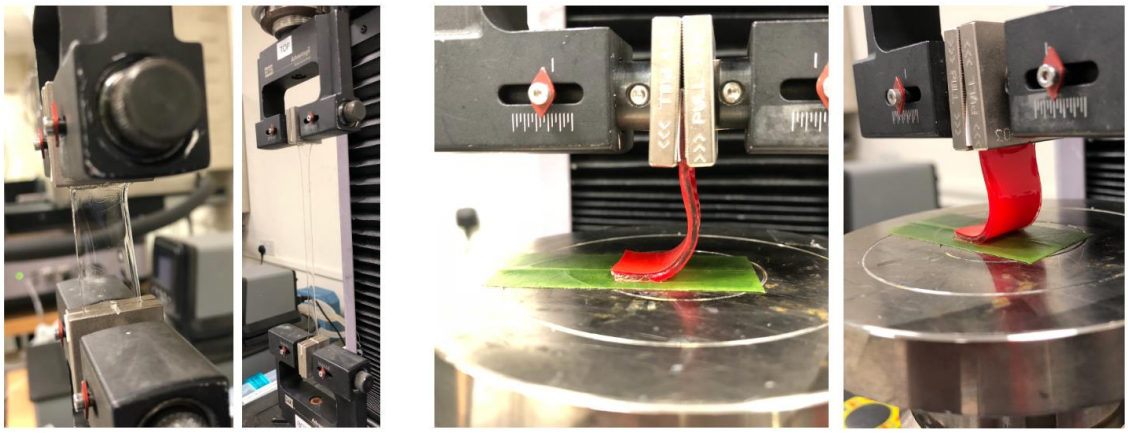

Figure 3.6 Photograph of mechanical tests of hydrogels. The elastic hydrogel can be characterized by a stress-strain test (left). The adhesiveness of the hydrogel can be characterized by a 90-degree peeling test. It is noted that due to the risk of directly measuring on the skin under a mechanical tester, the study surface can be replaced by a leaf surface.

3.5.3 Other properties of adhesive hydrogel

The adhesive hydrogel is also characterized by UV-vis spectroscopy to verify its optical transmittance. UV-vis spectroscopy is an analytical tool that measures the absorbance or transmittance of materials (solids or liquids) in terms of UV or visible light[12]. It can reveal the sample composition and potentially provide information about composition concentration. When the transmittance of visible light is interesting, the result can reflect how transparent the sample is.

The UV-vis spectrum can be measured using a UV-vis spectrophotometer. The UV-vis spectrophotometer contains a light source, a wavelength selector, a light detector, and accompanying computer software (Figure 3.7). The light source (such as xenon, tungsten, halogen, and deuterium lamp) can emit high-intensity light from UV to visible range. A wavelength selector is needed to select different wavelengths of light. The wavelength selector can be made from monochromators, absorption filters, interference filters, cutoff filters, and bandpass filters. Some part of the selected light would be absorbed by the measured sample, and the remaining part transmitted. The transmitted light can be

measured by the detector. The detector can transduce the light signal into an electrical signal based on photoelectric coatings or photosensitive semiconductors. The absorbance of the sample can be calculated using Beer-Lambert's law, which can be expressed as follows:

$$A = log_{10}(\frac{I_0}{I}) = log_{10}(\frac{1}{T}) = -log_{10}(T)$$

Beer-Lambert's law indicates that the absorbance (A) is the logarithm of a fraction of the intensity of light before passing through the sample (I_0) divided by the intensity after passing through the sample (I). The I/I_0 is also noted as transmittance.

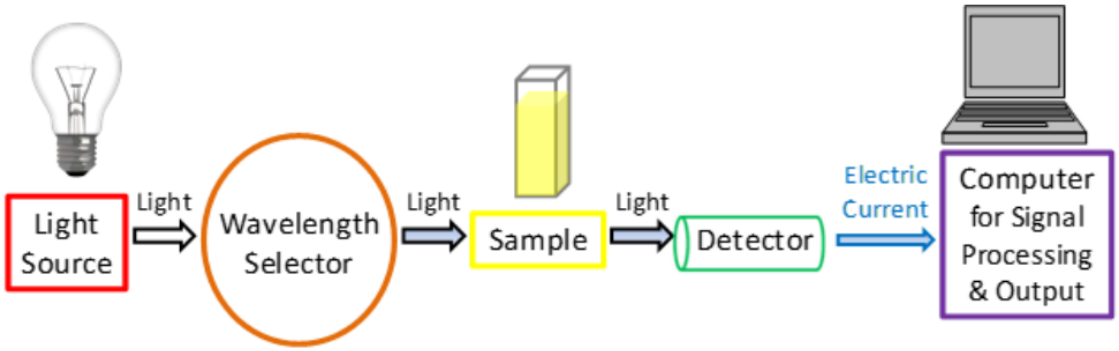

Figure 3.7 Schematic of the working principle of UV-vis spectrophotometry. The spectrophotometry includes a light source to emit light from UV to visible range, a wavelength selector to allow selecting light in a different wavelength. The selected light is emitted on the sample. The transmitted light to captured by the detector and the signal is further processed and visualized in a computer. Figure reproduced from Ref[13].

3.6 Characterization of Au nanomesh

Au nanomesh is a nanoscale material with a nanowire diameter of only 20 – 50 nm. To observe the morphology of such nanomaterial, scanning electron microscopy and transmission electron microscopy are needed. To observe how conformable Au nanomesh film can attach on rough surfaces, optical microscopy can be used. In addition, the Au nanomesh film is an electronic conductor. Its conductivity needs to be characterized using

electrical instruments. To quantify the conductivity of a thin film, square resistance can be measured as it is independent of the size of the thin film. Besides the sheet resistance, the resistance under deformation is also important to determine the stretchability of the conductive material. The stretchability, in this case, reflects the maximum strain that the material keeps conductive. It can be measured using a mechanical tester (to give a constant strain rate) and a Keithley digital multimeter (to measure resistance) simultaneously.

3.6.1 Electrical property of Au nanomesh

Sheet resistance is mostly used parameter to evaluate the conductivity of thin-film conductors. To make the sheet resistance measurement, two equal-sized electrodes are used along two parallel edges of the surface. The length and width of the surface should be equal and equal to the length of the two measuring electrodes (Figure 3.8). The surface resistivity from this measurement can be expressed as[14]:

$$\rho = R\frac{l}{W}$$

Where R is the measured resistance, l is the length between the two measuring electrodes, W is the width of the surface. As the width and length are kept the same, the measured resistance is the same regardless of the measuring electrode size and measured surface size. This resistance value is known as the sheet resistance with a unit of ohms per square (Ω/□).

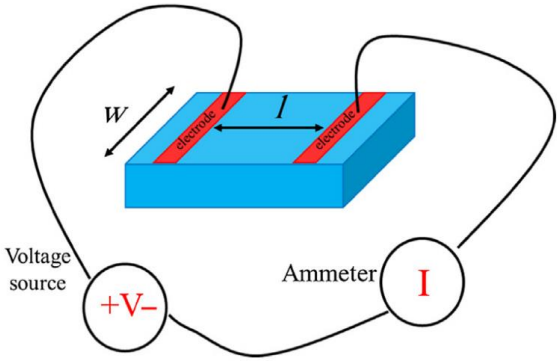

Figure 3.8 Schematic showing the electrical measurement of a thin film sheet resistance. Two measuring electrodes are needed. The measured surface width should be equal to its length to eliminate the effect of sample geometry. Figure reproduced from Ref[14].

Another commonly used technique to measure sheet resistance is by using a four-point probe method. This technique consists of four electrical probes in a line placed on the desired surface. Equal spacing is needed for arranging the probes. A current (I) is applied on the outer probe pair and the voltage drop (ΔV) between the inner probe pair is measured. The sheet resistance can be calculated as:

$$R = \frac{\pi}{ln(2)}\frac{\Delta V}{I} = 4.53236\frac{\Delta V}{I}$$

During the four-probe testing, the surface size needs to be sufficiently larger than the spacing size of the probe distance. Geometric correction is needed if the requirement is not satisfied[15].

3.6.2 Mechanical property of Au nanomesh

Au nanomesh film is not a freestanding film, it should be transferred on an elastic substrate to investigate its conductivity when stretched. PDMS serves as a substrate for Au nanomesh as it is a widely used elastic substrate. Au nanomesh transferred on PDMS form a stretchable conductor. The stretchability of Au nanomesh can be studied with a

mechanical tester (to give constant strain rate) and a digital multimeter (to measure resistance). The configuration is illustrated in Figure 3.9.

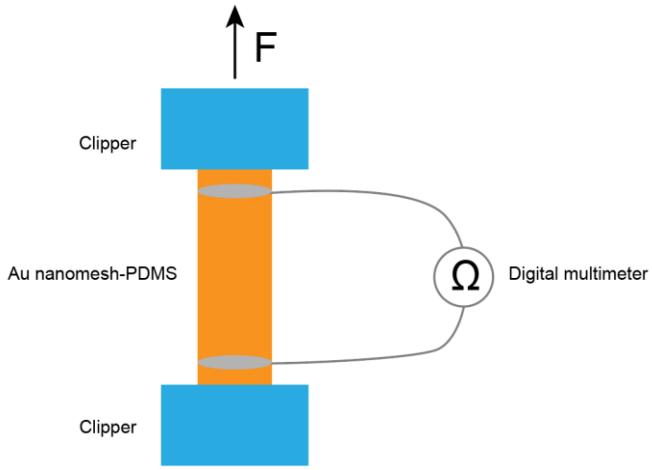

Figure 3.9 Schematic of the mechanical and electrical characterization of the Au nanomesh. The Au nanomesh conductor is not a freestanding film, it needs to be transferred onto a PDMS elastomer substrate to allow stretching under a mechanical tester. The stretch is given at a constant strain rate. The resistance of the Au nanomesh is measured by a digital multimeter at the same time.

3.6.3 Morphological characterization of Au nanomesh

Au nanomesh is composed of nanowires with a diameter of 20 – 50 nm. The nanostructure needs to be investigated using a scanning electron microscope (SEM) and transmission electron microscope (TEM). Electron microscopy is a powerful technique for nanomaterials characterization. Its resolution is much higher than that of light microscopy with the capability to analyze individual atoms. It also has a very high magnification range, from 10 to 500k for SEM and 2000 to 1 million times for TEM. Furthermore, an electron microscope relies on electron-sample interaction to generate signals, which can reveal a wide range of information about the sample. Electron microscopy is a very delicate instrument requiring high vacuum conditions[16].

SEM uses a focused electron beam to sequentially scan the sample (Figure 3.10 left). At each point, the secondary electron signal generated by the sample is collected by detectors.

An electron beam is generated from an electron gun and accelerated by an anode coil. The electron beam is further focused on electromagnetic lenses (condenser lenses). An objective lens with x-y scan coils further focuses on the electron beam and controls the position of the electron beam so that the electron beam can be scanned line by line. The electron beam is finally focused on the sample surface, going through an electron-sample interaction process. Due to the high energy of the electron beam, the sample surface is excited to produce Auger electrons, secondary electrons, backscattered electrons, and characteristic X-rays. Different signals reflect information in different depths of the sample. A series of detectors are placed right above the sample to collect different signals, such as an X-ray detector, back-scattered electron detector, and secondary electron detector. These signals can be amplified and finally visualized in computer software, revealing morphological or compositional information about the sample. It is noted the sample observed in SEM needs to be conductive to avoid charging of the sample. If it is not intrinsically conductive, Au or Pt should be sputter-coated on the sample surface. It also should be thoroughly dried to realize the high vacuum condition of the chamber. To observe the Au nanomesh using SEM, the Au nanomesh is firstly transferred on PDMS, the Au-PDMS film can be directly observed in SEM.

TEM has higher electron energy, higher electron accelerating voltage, and higher resolution than SEM (Figure 3.10 right). It is based on the detection of transmitted electrons, so the sample thickness needs to be controlled. The sample is usually loaded on a sample holder made from carbon mesh. The electrons are generated by an electron gun and accelerated by an anode coil, similar to those of SEM, but with higher energy. The condenser lenses with condenser aperture are used to focus the electron before it interacts with the sample. The objective lens is used to focus the transmitted electrons to form the diffraction pattern and form the first image. The electron beam is further filtered by objective aperture and selected area aperture, received by detector or viewing screen. More lenses can be placed in between condenser lenses and samples for STEM mode. The most advanced TEM also features a correction system before and after the sample for spherical aberration, which can greatly improve the spatial resolution to less than 0.05 nm. Due to its transmission mode, the samples that can be observed by TEM are more limited. The

TEM sample holder is usually less than 3 mm, and the maximum sample thickness is only 200 μm. To observe the Au nanomesh using TEM, the as-synthesized Au nanomesh on the water surface is lifted from water using the copper mesh sample holder and allows for complete drying.

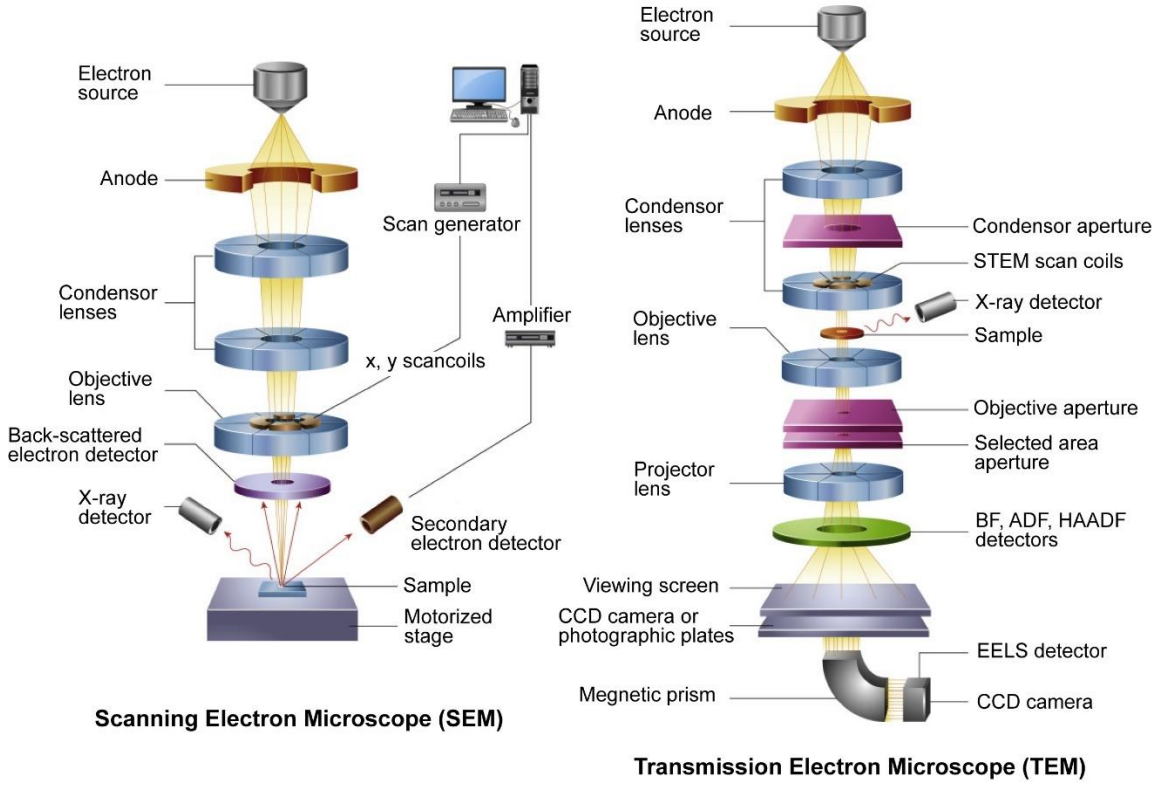

Figure 3.10 Schematic of the working principle of SEM and TEM. Each piece of equipment requires an electron gun and a series of electromagnetic lenses to focus and control the electron beam. A series of detectors are placed near the sample to collect different signals such as secondary electrons or X-rays. Figure reproduced from Ref[16].

3.7 Biopotential signal measurement on the human body

The measurement of biopotential on the human body requires rational electrode design and proper amplifier circuits. The conformal skin bioelectrodes can be used to measure different biopotential signals such as ECG and EMG, however, different biopotential requires different amplifier circuits for best measurement. An amplifier circuit to properly

measure different biopotential signals is possible but requires an intricate design to reject common-mode voltages and ensure amplification bandwidth for all signal frequencies.

3.7.1 ECG measurement

The measurement of ECG signals is a non-invasive yet very valuable clinical diagnostic tool. It uses 12 leads (10 electrodes) to plot 12 waveforms of heart electrical activity from different aspects[17]. The 12-lead ECG is a standard clinical measurement, and it can detect many heart-related diseases such as arrhythmias, coronary disease, or electrolyte imbalance. The 12-lead ECG includes 6 chests (precordial) leads (V1, V2, V3, V4, V5, and V6) (Figure 3.11 left), and 6 limbs (extremity) leads (Lead I, Lead II, Lead III, aVR, aVL, aVF) (Figure 3.11 right). The 6 limb leads are obtained from 4 electrodes, known as RA (right arm), LA (left arm), LL (left leg), and RL (right leg). Viewing the heart as a center point, the 12-lead ECG form 12 perspectives of the heart, which is in two planes, vertical and horizontal planes. The vertical plane includes 6 limb leads (Lead I, Lead II, Lead III, aVR, aVL, and aVF). Lead I, Lead II, and Lead III are measured by bipolar electrode pair (negative and positive electrodes). aVR, aVL, and aVF are unipolar and only need a positive electrode. For the unipolar leads, the reference for the positive electrode is from an Einthoven's triangle (RA, LA, and LL). The averaged reference potential of Einthoven's triangle is called Wilson's Central Terminal (WCT). The aVR, aVL, and aVF are based on the WCT as reference for their positive electrode. The horizontal plane of the heart activity is from the 6 chest leads, V1, V2, V3, V4, V5, and V6. Similar to the aVR, aVL, and aVF, the 6 chest leads are also unipolar which only requires a positive lead. They are also based on WCT as the reference.

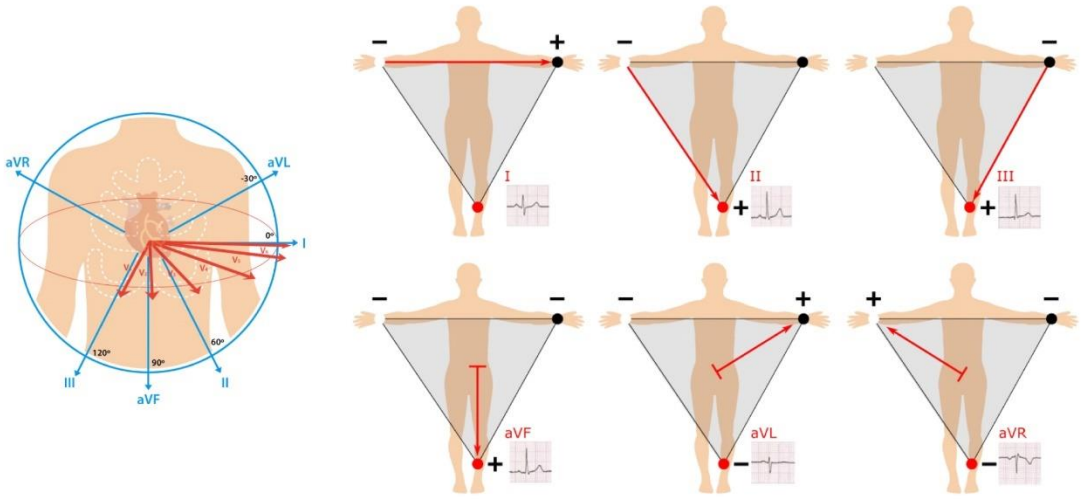

Figure 3.11 Schematic showing the 12-lead ECG system. The 12 leads can give orientational information of two planes about the heart. One is a vertical plane including 6 leads: Lead I, Lead II, Lead III, aVR, aVL, aVF. These 6 leads are called limb leads. The other is a horizontal plane, including 6 leads: V1, V2, V3, V4, V5, and V6. These 6 leads are on the chest. Figures reproduced from Ref[17, 18].

The 12-lead ECG can be measured using a clinical standard ECG machine, however, for personal wearable devices outside the hospital, it is difficult to implement such an instrument. We applied a three-lead ECG measurement with different electrode placements to obtain similar 12-lead ECG waveforms[19]. It should be noted that such 12-lead ECG measurement cannot be used for standard clinical analysis. It is an alternative to roughly estimate the 12-lead waveform for a purpose of convenience and when a standard medical instrument is not available.

In the three-lead ECG measurement, there is a right leg drive (RLD) electrode. This RLD electrode is an output electrode driven by an RLD amplifier (Figure 3.12). This lead senses the common-mode voltage from the other two input electrodes and drives an opposing voltage to the patient. This electrode eliminates the common-mode voltage in the inputs, greatly improving the CMRR.

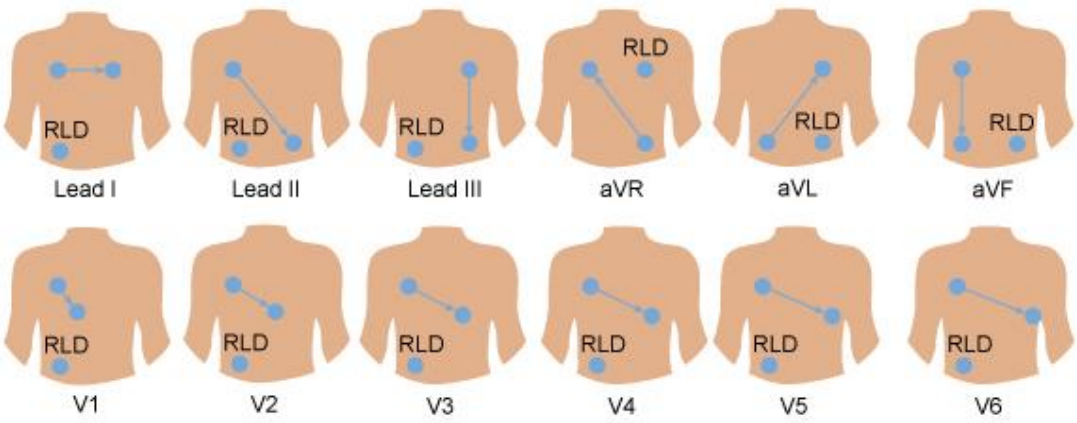

Figure 3.12 The three-electrode system to measure the 12-lead ECG results. Normally the 12-lead ECG system requires 10 electrodes. A three-electrode system can roughly reproduce 10-lead ECG results. The ECG signal from the three-electrode system is measured using an Analog Devices chip AD8232 with a right leg driver (RLD). RLD is like a common ground to reduce noises. This three-electrode system can minimize the measurement electrodes used.

The data acquisition system for the three-lead electrode configuration can be a single lead heart rate monitoring module using AD8232 as the amplifier. It shows a good signal-to-noise ratio due to the RLD electrode. However, such a module in hard PCB (printed circuit board) is not wearable and its output is another amplified analog signal, which requires another analog-to-digital converter (ADC) to feed the data to a computer. To make a more integrated and wearable device, we designed and fabricated a general-purpose biopotential measurement device (Figure 3.13). This device is wireless (based on Bluetooth Low Energy 5.0), miniaturized (as small as 1.8 cm), and flexible (based on polyimide substrate). It is composed of a biopotential amplifier and a Bluetooth microcontroller. The biopotential amplifier amplifies the biopotential (ECG or EMG) with high CMRR. The Bluetooth microcontroller has built-in analog input and ADC. Amplifier signals can be directly fed into the microcontroller and wirelessly sent to the computer or smartphone. This flexible PCB device makes the measuring of biopotential signals much easier.

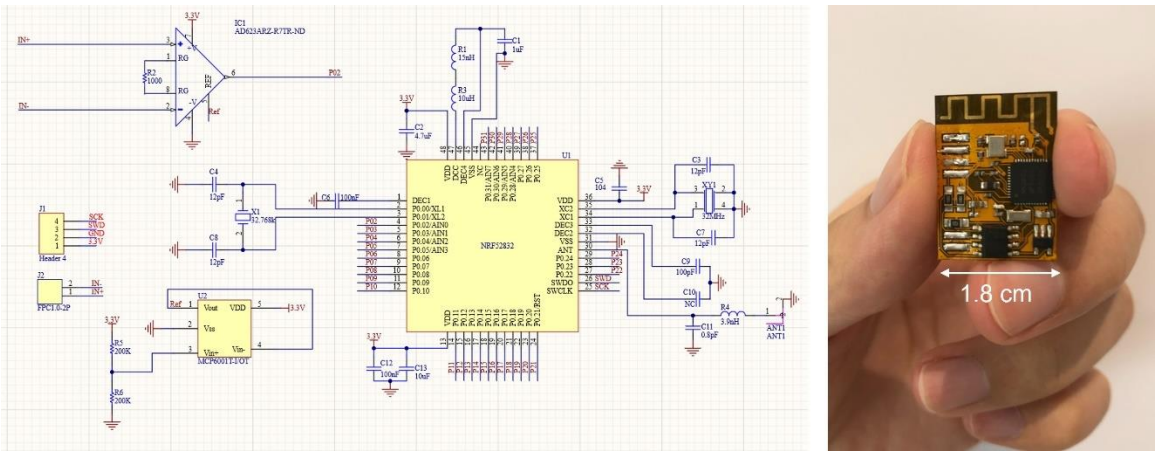

Figure 3.13 The schematic and photo of the customized flexible PCB for measuring biopotential signals. The flexible PCB includes an amplifier and a Bluetooth microcontroller. The flexible PCB is miniaturized (as small as 1.8 cm) and is wireless. It can be used to measure ECG and EMG.

3.7.2 EMG measurement

The EMG signal is measured using a Backyard Brains Heart and Brain SpikerBox and a Texas Instruments Analog front end evaluation board. Three skin electrodes are placed on the arm, one measuring electrode on the center of the biceps brachii muscle and one measuring electrode on the end of the biceps brachii muscle. Another ground electrode can be placed on the back of the hand or in other places without main muscles. The signals are measured without any further filtering.

References

[1] S. Lin, H. Yuk, T. Zhang, G. A. Parada, H. Koo, C. Yu, X. Zhao, Advanced Materials 2016, 28, 4497; C. Yang, Z. Suo, Nature Reviews Materials 2018, 3, 125.

[2] Y. Ohm, C. Pan, M. J. Ford, X. Huang, J. Liao, C. Majidi, Nature Electronics 2021, 4, 185.

[3] M. Prabaharan, J. F. Mano, Macromolecular Bioscience 2006, 6, 991.

[4] Z. Dastjerdi, E. D. Cranston, M. A. Dubé, International Journal of Adhesion and Adhesives 2018, 81, 36.

[5] S. Fujii, S. Sawada, S. Nakayama, M. Kappl, K. Ueno, K. Shitajima, H. J. Butt, Y. Nakamura, Materials Horizons 2016, 3, 47.

[6] M. Ramuz, B. C.-K. Tee, J. B.-H. Tok, Z. Bao, Advanced Materials 2012, 24, 3223; J. Kim, J. Park, U. Jeong, J.-W. Park, Journal of Applied Polymer Science 2016, 133; A. Vohra, H. L. Filiatrault, S. D. Amyotte, R. S. Carmichael, N. D. Suhan, C. Siegers, L. Ferrari, G. J. E. Davidson, T. B. Carmichael, Advanced Functional Materials 2016, 26, 5222.

[7] L. S. Lim, N. A. Rosli, I. Ahmad, A. Mat Lazim, M. C. I. Mohd Amin, Nanomaterials 2017, 7, 399.

[8] G. Ramanath, J. D'Arcy-Gall, T. Maddanimath, A. V. Ellis, P. G. Ganesan, R. Goswami, A. Kumar, K. Vijayamohanan, Langmuir 2004, 20, 5583.

[9] M. D. Ho, Y. Liu, D. Dong, Y. Zhao, W. Cheng, Nano Letters 2018, 18, 3593.

[10] S. Wang, J. Zhang, O. Gharbi, V. Vivier, M. Gao, M. E. Orazem, Nature Reviews Methods Primers 2021, 1, 41.

[11] J. Liu, S. Lin, X. Liu, Z. Qin, Y. Yang, J. Zang, X. Zhao, Nature Communications 2020, 11, 1071; H. Yuk, T. Zhang, S. Lin, G. A. Parada, X. Zhao, Nature Materials 2016, 15, 190; H. Yuk, T. Zhang, G. A. Parada, X. Liu, X. Zhao, Nature Communications 2016, 7, 12028.

[12] V. Amendola, M. Meneghetti, The Journal of Physical Chemistry C 2009, 113, 4277.

[13] https://www.technologynetworks.com/analysis/articles/uv-vis-spectroscopy-principle-strengths-and-limitations-and-applications-349865.

[14] A. K. Reza Taherian, *Electrical Conductivity in Polymer-Based Composites*, Elsevier, 2018.

[15] https://www.ossila.com/pages/sheet-resistance-theory.

[16] G. Hübschen, *Materials Characterization Using Nondestructive Evaluation (NDE) Methods*, Elsevier, 2016.

[17] F. Greco, A. Zucca, S. Taccola, B. Mazzolai, V. Mattoli, ACS Appl Mater Interfaces 2013, 5, 9461.

[18] https://www.cablesandsensors.com/pages/12-lead-ecg-placement-guide-with-illustrations.

[19] K. Yoneyama, M. Naka, T. Harada, Y. Akashi, Journal of Arrhythmia 2020, 36, 1107.

Chapter 4

Design and fabrication of skin bioelectrode materials

This chapter details the design, fabrication, optimization, and characterization of skin bioelectrode materials. The adhesive hydrogels are fabricated using a thermal polymerization process. Their conductivities are modulated by ionic additives. Their mechanical, optical properties are investigated. The Au nanomesh conductor is fabricated using a wet chemistry method. Its electrical, optical, mechanical, and morphological information is characterized, and its fabrication process is optimized. The results show that the skin bioelectrode materials are promising candidates for application on skin biopotential measurement.

4.1 Introduction

To realize high signal fidelity comfort biopotential signal measurement, the development of conformal skin electrodes is very important. Conformal skin electrodes should possess several attributes. One is that Young's modulus of the skin electrodes should be similar to those of skin, this is to ensure the mechanical match between the electrodes and the skin, to make sure the electrodes can deform easily in response to skin deformation[1]. The second attribute is that the electrodes should possess some adhesiveness towards the skin[2]. The skin surface is covered by a layer of dry and non-conductive stratum corneum. This layer may be also very oily due to sweating of the skin. The hairs extruding out the skin surface also obstruct the attachment of electrodes on the skin. The third attribute is that the skin bioelectrode should keep conductive even under deformation. Electrodes depend on conductivity to transduce electrical signals. The conductive electrodes under deformation make it suitable to measure signals even when the skin deforms. The fourth attribute is that the electrode should keep biocompatible on the skin, without causing skin irritation or inflammation when attached to the skin for a longer period.

To realize the requirements of skin bioelectrodes for biopotential signal measurement, rational materials design is important. Acrylic hydrogel is a soft polymeric material that contains a large amount of water[3]. It can be made ionic conductive when supplemented with ionic additives. Its Young's modulus can be modulated to less than 1 MPa, which is even softener than human skin. In addition, it is also adhesive due to its rich carbon hydroxyl groups. PAA hydrogel and PAAm hydrogel are two members of such promising hydrogels. The PAA or PAAm hydrogel can be used as an electrolyte gel layer in contact with skin. In addition to the hydrogel, an electronic conductive layer should also be incorporated to transduce ionic current in hydrogel into the electronic current for external device measurement. For this reason, two types of stretchable conductors were also developed. One is the thermo-evaporated Au nanofilm and the other is chemically synthesized Au nanomesh. Thermo-evaporated Au nanofilm has the advantages of controllable thickness and high repeatability. Most importantly, the Au nanofilm evaporated on the elastomer substrate can form a microcrack, which is useful for achieving

high stretchability. The Au nanomesh has the advantage of controllable transparency while maintaining high conductivity. To overcome the short usage time of hydrogel materials, a conductive and adhesive coating technique based on pressure-sensitive adhesive onto Au nanofilm is also presented.

4.2 Experimental Methods

4.2.1 Preparation of adhesive hydrogel

The PAA hydrogel precursor solution was first prepared[4]. Briefly, in 4 ml deionized water, 1 ml acrylic acid, 20 mg potassium chloride, 40 mg potassium persulfate, 1.67 mg N,N'-methylenebisacrylamide, and 40 µl N,N,N',N'-tetramethylethylenediamine were subsequently added. The precursor solution was degassed under N_2 gas for 10 min to remove O_2. The precursor solution should be used right after the degassing. To make PAA hydrogel in the desired shape, a handmade PDMS mold was made first. The PDMS mold with 3 mm × 3 mm wells was put on top of the glass substrate and a PAA hydrogel precursor solution was poured into the PDMS wells. The PDMS mold was covered by a petri dish and heated in an oven at 70 °C for 15 min. After the heating process, the hydrogel was formed in the PDMS mold and was washed with 0.1 M KCl aqueous solution for 30 min. The preparation of PAAm hydrogel is similar to the PAA hydrogel. The 1 ml acrylic acid needs to be replaced by 0.12 g acrylamide. The precursor solution should be used right after degassing.

4.2.2 Mechanical characterization of adhesive hydrogel

To characterize the adhesive hydrogel in a mechanical tester, the adhesive hydrogel was first prepared in a size of 3 x 1 cm. The two ends of the hydrogel were fixed on the clipper of the mechanical tester. A constant strain rate (0.5 mm s^{-1}) was set to the mechanical tester in software. The hydrogel was stretched until rupture. The stress and strain are recorded. To measure the adhesive strength, one half of the hydrogel was attached to a leaf surface, the other end of the hydrogel was fixed on the clipper of the mechanical tester. There forms

a 90 degree between the part adhered to the leaf surface and the part fixed by the clipper. A constant strain rate (0.5 mm s^{-1}) was set to peel off the adhesive hydrogel, the stress was recorded. Adhesive strength can be calculated by dividing the stress plateau by the width of the hydrogel.

4.2.3 Preparation of Au nanomesh

The Au nanomesh was fabricated as previously reported. Briefly, 4.8 mg of gold (III) chloride trihydrate ($HAuCl_4 \cdot 3H_2O$; Sigma-Aldrich) was dissolved in 25 ml deionized water and stored in a 4 ºC fridge. 0.9 mg of sodium borohydride ($NaBH_4$; Sigma-Aldrich) was dissolved in 25 ml deionized water. The $NaBH_4$ solution in a syringe was slowly added into $HAuCl_4$ solution by a syringe pump. The $HAuCl_4$ solution in a 250 ml glass beaker was kept at 5 ºC and stirred at 400 r.p.m. during adding $HAuCl_4$. The adding of $NaBH_4$ takes 15 min and the $HAuCl_4$ solution is changed into red-wine color. Then 100 ml toluene (Sigma-Aldrich) was added into the mixed solution and stirred at 600 r.p.m. and 5 ºC for 15 min. The solution was rested in the ambient condition for another 30 min with a clear water-toluene layer separation. The toluene top layer was removed using a pipette and the water solution was left in a fume hood. After toluene residuals were fully evaporated, one Au nanomesh layer can be found on the water surface.

4.2.4 Fabrication of Au nanomesh-PVA film

An ITO glass was cut into 4.5 cm x 4.5 cm as a substrate. PDMS was prepared by mixing SYLGARD 184 silicone elastomer base and a curing agent at a ratio of 10:1, spin-coated on the ITO glass substrate at 1000 r.p.m. for 60 s and cured at 80 °C for 5 h. To transfer the Au nanomesh on the water surface to PDMS, the PDMS-glass substrate was gently in contact with the Au nanomesh layer on the water surface and kept for 10 s. The PDMS-glass substrate was lifted and dried in ambient conditions. Au nanomesh was transferred on the PDMS surface. PVA solution was prepared by dissolving 20 wt% PVA (average Mw 31,000-50,000, 87-89% hydrolyzed; Sigma-Aldrich) in deionized water. PVA solution was cast on Au nanomesh-PDMS-glass substrate, spin-coated at 1200 r.p.m. for 60 s, and

dried in an oven at 60 ºC for 1 h. Lastly, PVA was peeled off from the PVA-Au nanomesh-PDMS-glass substrate. Au nanomesh would be attached to the PVA layer, forming Au nanomesh-PVA film.

4.2.5 Fabrication of patterned Au nanomesh-PVA film

A mask was designed in AutoCAD 2020 and a thin polyethylene terephthalate (PET) film was cut according to the designed mask in Silhouette Cameo. The thin PET mask was covered on a PDMS-glass substrate. An Au nanomesh-PVA film was pressed on the PET masked PDMS-glass substrate. Water was added to dissolve PVA, printing Au nanomesh on the PET masked PDMS-glass substrate. PET mask was peeled off and Au nanomesh was patterned on PDMS-glass substrate. PVA solution was cast on the patterned Au nanomesh-PDMS-glass substrate and spin-coated at 1200 r.p.m. for 60 s, dried in an oven at 60 ºC for 1 h. Then PVA was peeled off with Au nanomesh attached, forming patterned Au nanomesh-PVA film.

4.2.6 Fabrication of Au nanomesh-PDMS

A PDMS film was prepared by mixing SYLGARD 184 silicone elastomer base and a curing agent at a ratio of 10:1, spin-coated on a silicon wafer at 800 r.p.m. for 60 s and cured at 80 °C for 5 h. The PDMS film was first attached to a PET film and the PET–PDMS film was cut into the desired shape for transfer onto the Au nanomesh. The PET–PDMS film was put in contact with the Au nanomesh on top of the water surface; the contact was kept for 20 s for a complete transfer. Then the PET–PDMS–Au nanomesh film was lifted and allowed to dry at the ambient condition. The PDMS film was peeled off from the PET for further use.

4.2.7 Characterization of Au nanomesh

The transmittance of Au nanomesh-PVA film was measured using an ultraviolet-visible (UV–vis) spectrophotometer (Shimadzu UV-2550). The nanostructure of Au nanomesh-

PVA film was characterized by a field-emission scanning electron microscope (JEOL, 7600F). The square resistance of Au nanomesh-PVA film was measured using a multimeter. Briefly, the Au nanomesh-PVA film was cut into 1 cm x 1 cm square. Two opposite edges of the square were painted with silver paste lines. The resistance between the two silver paste lines was measured as square resistance.

4.2.8 Electrical and mechanical characterization of Au nanomesh

The cyclability of the Au nanomesh–PDMS film (3 cm × 1 cm) was measured by a parameter analyzer (Keithley 4200) and a mechanical tester (MTS Criterion model C42). A 50% strain was applied to the film at a strain rate of 0.2 mm s^{-1} for 200 times by the mechanical tester. The resistance of the film was recorded by the parameter analyzer. The stretchability of the Au nanomesh–PDMS film (3 cm × 1 cm) was measured by the parameter analyzer and the mechanical tester. The film was stretched at a strain rate of 0.2 mm s^{-1} until rupture. The resistance of the film was recorded by the parameter analyzer. The interfacial impedance between the electronic films and hydrogel was measured by an electrochemical workstation (Zennium E, Zahner Ennium). A hydrogel film (1 cm × 1 cm) was sandwiched between two Au nanomesh–PDMS films (2 cm × 1 cm), with the Au nanomesh in contact with two sides of the hydrogel film. The impedance of the Au nanomesh–hydrogel–Au nanomesh film was measured from 100 to 10^6 Hz. The admittance was calculated as the reciprocal of the impedance to reflect the ease of current transduction from the Au nanomesh to the hydrogel. As control groups, AgNW and CNT on the PDMS film (2 cm × 1 cm)—with conductance like the Au nanomesh film—and the aluminum foil were also measured with the same sandwich configuration. AgNW and CNT films were prepared by the vacuum filtration method, where AgNW and CNT were first filtrated on a filter paper and then transfer printed on a PDMS film; the conductance values of the AgNW and CNT films were tuned by the amounts of solution filtrated on the filter paper.

4.3 Design and fabrication of adhesive hydrogel

Adhesive hydrogel is prepared from thermo-polymerization of PAA. There are some issues related to hydrogel materials. First, the hydrogel material is easy to lose water over time, methods to prevent hydrogel water loss are needed. Second, the ionic current in hydrogel material needs to be transduced into the electronic current. The electronic layer is usually based on an elastomer substrate. To overcome these two issues, the bonding between PAA hydrogel material and elastomeric PDMS material is explored.

To realize a tough bonding between PAA and PDMS, PDMS substrate is firstly plasma treated with a mixed gas including nitrogen and AA (acrylic acid) monomers (Figure 4.1). The plasma treatment embedded a layer of AA monomers on the PDMS surface. Then a PDMS mold is applied on top of the PDMS substrate and PAA precursor solution (AA monomer, thermal initiator, accelerator, cross-linker, ionic additive in aqueous solution). The solution is capped with another PDMS mold layer so that the solution is sealed in a mold chamber. The PAA solution in the PDMS chamber is heated in an oven for 10 min for fully thermo-polymerization. After the thermal treatment, the PDMS mold is removed, and the hydrogel layer is grown attached to the PDMS substrate. The bonding between the PDMS and the hydrogel is achieved due to the participation of the AA layer embedded in the PDMS surface in the thermo-polymerization of the hydrogel. The thickness of the hydrogel layer on the PDMS substrate can be controlled by adjusting the amount of precursor solution.

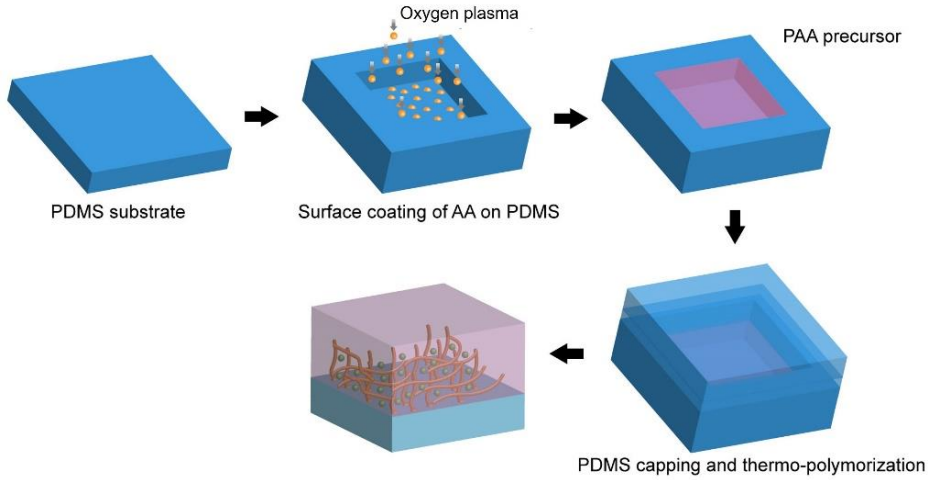

Figure 4.1 Schematic of the fabrication process of PAA hydrogel on PDMS substrate. The PDMS substrate is first coated with acrylic acid monomer to increase bonding between the hydrogel and PDMS. The PAA hydrogel is fabricated inside a PDMS mold on the PDMS substrate.

To verify the efficiency of AA layer coating on the PDMS substrate by the surface plasma treatment of nitrogen-AA mixed gas. Contact angle measurement of the PDMS surface is conducted (Figure 4.2). AA monomer, due to their rich hydrocarboxylic group, is hydrophilic, while PDMS surface is very hydrophobic. The grafting of AA on PDMS is expected to change the surface hydrophilicity. The surface hydrophilicity is measured using an OCA 15 Pro (DataPhysics Instruments GmbH) equipped with a single direct dosing system SD-DM. A water droplet is dropped on the sample surface while a camera is used to photo the profile of the water-sample surface contact. Two areas for each sample are measured. The raw PDMS surface has a contact angle of 119º and 112º. The PDMS surface treated with AA monomers recorded a contact angle of 61º and 69º, which is around only one-half of the raw PDMS surface. This indicates that the plasma treatment of the AA-nitrogen gas mixture on the PDMS surface successfully grafted AA monomers on the PDMS surface.

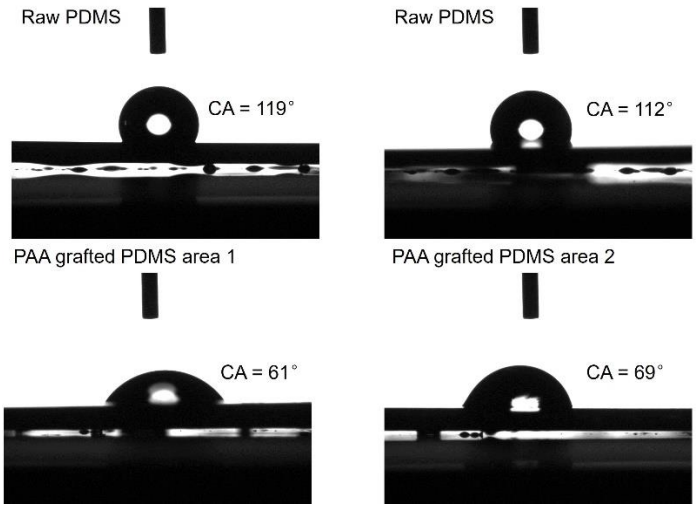

Figure 4.2 Contact angle of PDMS surface after coated by AA monomer. The contact angle decreased from 112 – 119 degrees to 61 – 69 degrees after the AA coating, indicating the hydrophilic effect of the AA coating.

The synthesized PDMS-hydrogel hybrid shows high transparency and high stretchability (Figure 4.3). Due to the grafting of AA monomer on the PDMS surface, the hydrogel and PDMS substrate tightly bonded together keeps intact even during stretching. Due to the elasticity of both PDMS substrate and hydrogel, the hybrid film is highly elastic. The PDMS-hydrogel hybrid is also conformal to different surfaces as the hydrogel side remains adhesive. When adhered to the leaf, the PDMS-hydrogel hybrid is highly conformal. It can instantly cover the hydrophobic leaf surface. On the other hand, the PDMS cover can prevent water loss from the top hydrogel surface, extending the usage time of the hydrogel. The hydrogel can also be adhered to the skin with high conformability, confirming their application as an electrolyte layer in skin bioelectrode.

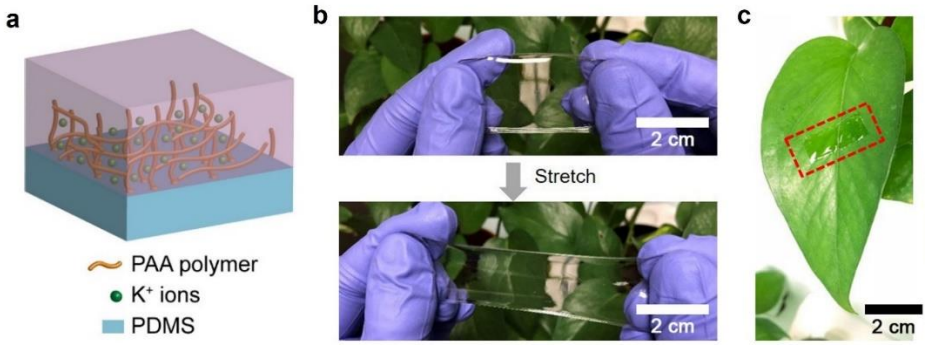

Figure 4.3 The PAA hydrogel on PDMS substrate. (a) Schematic of the PAA hydrogel on PDMS substrate. (b) Photograph of the hydrogel-PDMS under stretching. (c) Photograph of the hydrogel-PDMS attached on a plant leaf, showing its transparency and conformability.

As an electrolyte layer in the skin bioelectrode application, the hydrogel layer should be highly ionic conductive. Hydrogel contains more than 90% of water. Its conductivity is similar to the saline solution (0.9% salt in water), ions can migrate in the hydrogel under an electrical field. The conductivity of hydrogel can be boosted by the addition of ionic additives. Four types of ionic additives ($CaCl_2$, LiCl, NaCl, are KCl) are added to the hydrogel precursor solution at the same concentration of 0.5 M. The electrical properties of the hydrogel can be characterized by EIS. The hydrogel sample is prepared in a film (with a dimension of 30 mm x 10 mm x 1.5 mm). Two ends of the hydrogel connect with liquid metal. Copper wires are inserted into the liquid metal points (Figure 4.4d). The two terminals of the EIS system connect the copper wires. Both Nyquist plot and Bode plot are presented to compare the impedance of hydrogels enriched by different ionic additives (Figure 4.4a-b). The impedance values in terms of capacitive effect and resistive effect are also calculated based on the real part and imaginary part of the Nyquist plot (Figure 4.4c). Each ionic additive is repeated with four samples to obtain statistical meaning. It is found that the KCl and $CaCl_2$ show the highest conductivity in the hydrogel system, making them superior candidates as ionic additives in hydrogel fabrication for skin bioelectrodes.

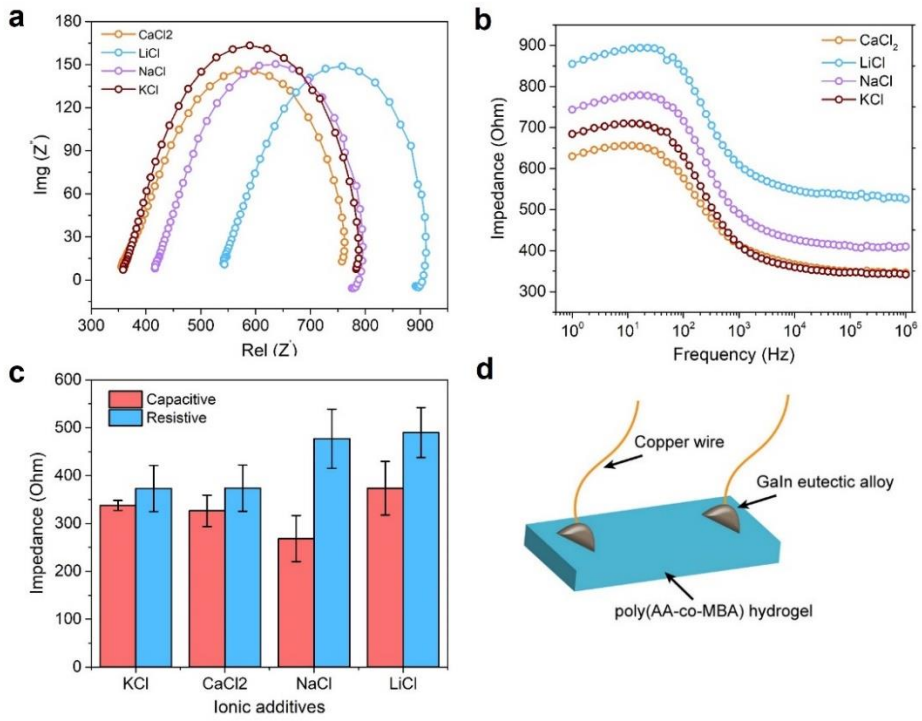

Figure 4.4 Impedance of the PAA hydrogel with different ionic additives. (a) Nyquist plot of the hydrogel with different ionic additives. (b) Bode plot of the hydrogel with different ionic additives. (c) Capacitive and resistive impedance comparison of the hydrogel with different ionic additives. (d) Schematic of the impedance measurement. The hydrogel sample has a dimension of 30 x 10 x 1.5 mm. The ionic additive concentration is 0.5 M. The EIS has a perturbation voltage of 30 mV from 1 Hz to 1 MHz. Each ionic additive was measured with 4 repeated samples.

The ionic conductivity is the most important parameter in evaluating the adhesive hydrogel. However, other properties such as optical transmittance and adhesiveness need to be considered when designing hydrogel materials. Hydrogels with different ionic additives are investigated in a UV-vis spectrophotometer to compare their optical transmittance. For different ionic additives including KCl, NaCl, LiCl, and $CaCl_2$, KCl and NaCl show the highest transmittance spectrum in the 300 – 800 nm wavelength range (Figure 4.5a). To characterize the transmittance values in some specific wavelengths, the transmittance at 440 nm and 660 nm are compared (Figure 4.5b). Hydrogels with KCl and NaCl additives show light transmittance above 90%, indicating the highly transparent property of the hydrogels. The optical transmittance property confirmed the advantages of KCl as a hydrogel ionic additive.

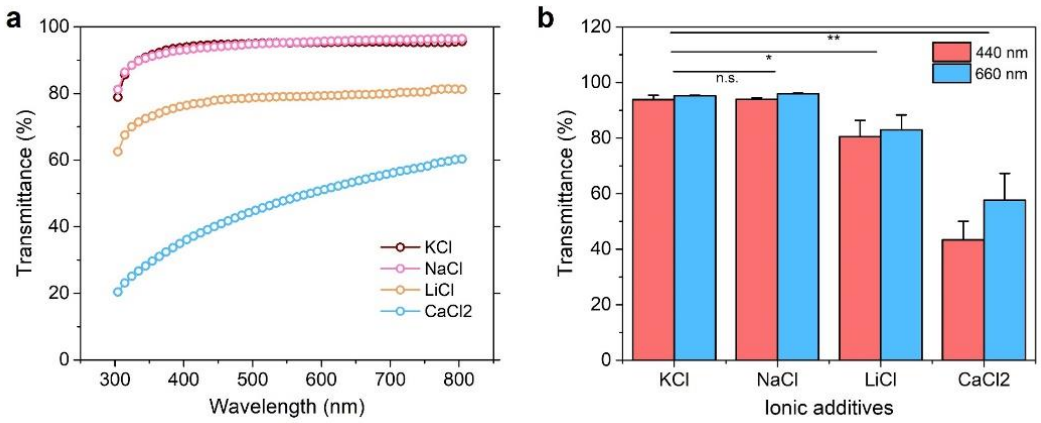

Figure 4.5 Optical transmittance of the hydrogel with different ionic additives. (a) The UV-vis transmittance spectroscopy of the hydrogel with different ionic additives. (b) The transmittance at 440 nm and 660 nm of the hydrogel with different ionic additives. The hydrogel electrode dimension is 40 mm x 15 mm x 2 mm, and the ionic concentration of hydrogel precursor solution is 0.5 M. Student's t-test: n.s., not significant, * $p < 0.05$, ** $p < 0.005$, $n = 3$.

The adhesive property of hydrogels with different ionic additives is another important property. It is an important parameter to determine how conformal the hydrogel can adhere to the skin or other surfaces. The adhesiveness of hydrogels enriched by different ionic additives is investigated by a 90-degree peeling test. The hydrogel films adhere to a plant leaf surface as an alternative to human skin. The other end of the hydrogel is pulled at a constant strain (0.5 mm s^{-1}) and the pulling force is measured in a mechanical tester. The adhesive strength (pulling force divided by the hydrogel film length) is plotted during the peeling process (Figure 4.6a). It can be shown that the $CaCl_2$ enriched hydrogel shows negligible adhesive strength (only 0.4 N m^{-1}), while KCl recorded the highest strength (14 N m^{-1}) (Figure 4.6b). This result indicates that the hydrogel with KCl additive is superior in terms of stronger bonding with different biological surfaces.

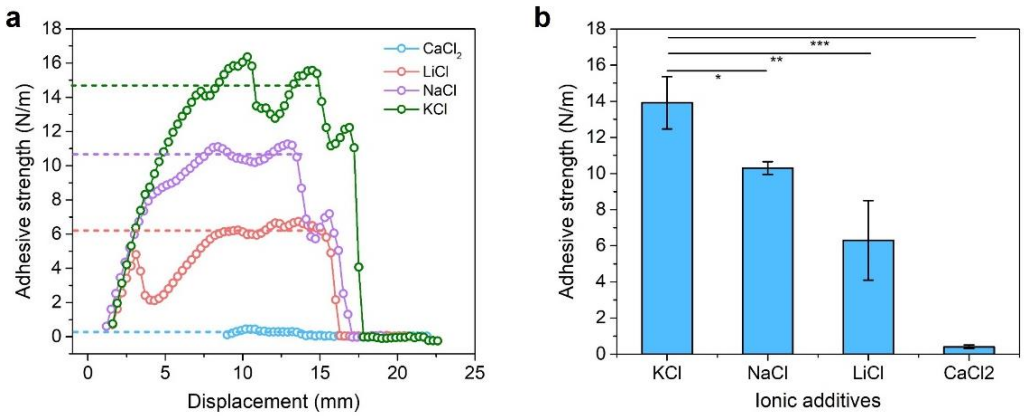

Figure 4.6 Adhesive strength of the hydrogel with different ionic additives. (a) the adhesive strength measured from a mechanical tester. (b) the adhesive strength of hydrogel with different ionic additives. The hydrogel electrode dimension is 40 mm x 15 mm x 2 mm and ionic concentration is 0.5 M, 3M VHB tape is used as hard baking, healthy fresh leaf of lipstick vine as the surface. Student's t-test: * $p < 0.01$, ** $p < 0.001$, *** $p < 0.0005$, $n = 4$.

From the above characterization and analysis, it is confirmed that the KCl additive in the hydrogel demonstrated the best conductivity, transmittance, and adhesiveness properties. As such, KCl can be selected as an ionic additive for hydrogel preparation in skin bioelectrode applications. The effects of different concentrations of KCl in the hydrogel precursor solution are further investigated. The KCl concentrations of 0.5 M, 1 M, and 2 M in hydrogel precursor solution are prepared and the hydrogel is made as previously described. The hydrogels are prepared in the film shape (30 mm x 10 mm x 1.5 mm) for EIS measurement (Figure 4.7). As expected, hydrogels with higher KCl concentrations show lower impedance, as more ions contributed to the migration under the electrical field in the hydrogel. Hydrogel film with 0.5 M KCl additive has an impedance of 746 Ω at 1 Hz, while hydrogel film with 2 M KCl additive has an impedance of 457 Ω. From the impedance measurement it is clear the higher salt concentration, the higher conductivity. However, other properties also need to be considered to choose the proper ionic additive concentration.

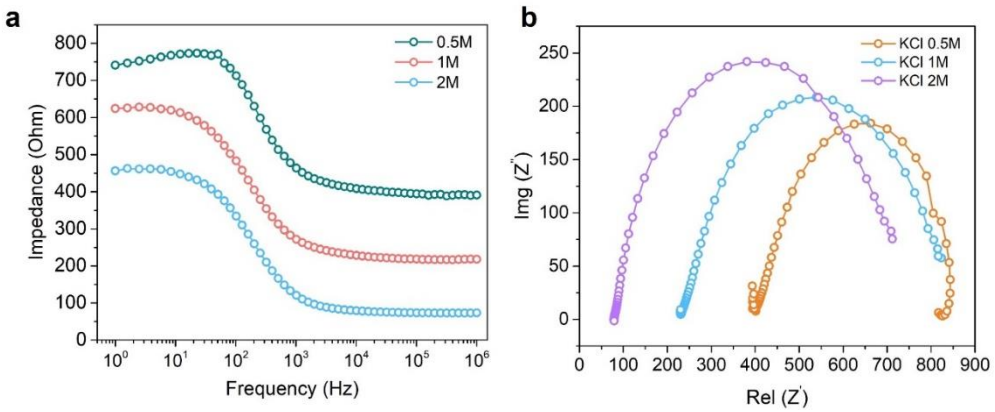

Figure 4.7 Impedance measurement of the hydrogel with KCl additive at different concentrations. (a) The Nyquist plot. (b) The Bode plot. The hydrogel electrode dimension is 30 mm x 10 mm x 1.5 mm.

The optical transmittance of hydrogels enriched with different KCl concentrations is also investigated. Hydrogels are prepared in the film form with a size of 40 x 15 x 2 mm and inserted in a UV-vis spectrophotometer under transmittance mode (Figure 4.8). It is shown that the 0.5 M and 1 M KCl additive does not influence the hydrogel transmittance, which is a transmittance as high as 95% - 97%. However, the 2 M KCl enriched hydrogel film showed a transmittance spectrum only in the 60% – 70% range. This optical transmittance results suggest that the KCl concentration should be kept below 1 M to maintain a high optical transmittance. However, the adhesive property should also be investigated to understand the effects of salt concentration on hydrogel adhesiveness.

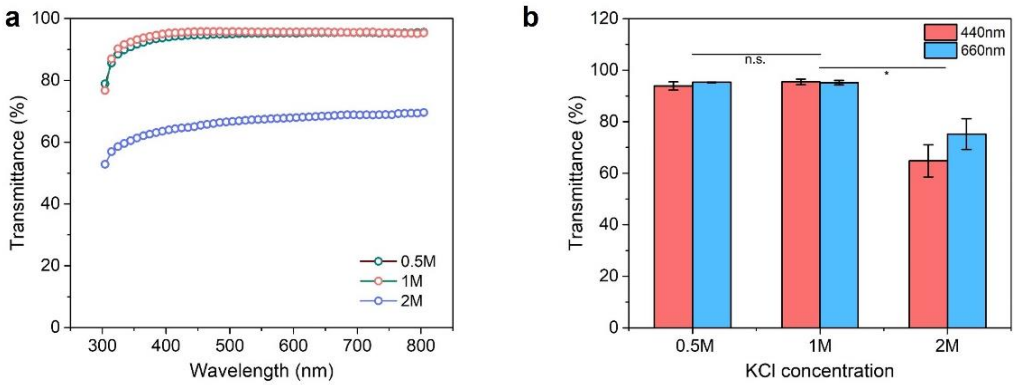

Figure 4.8 Optical transmittance of the hydrogel with KCl additive at different concentrations. (a) The UV-vis spectroscopy of the hydrogel. (b) The transmittance at 440 nm and 660 nm of the hydrogel with different KCl concentrations. Hydrogel electrode area: 40 x 15 x 2 mm. Student's t-test: n.s. not significant, * $p < 0.05$, $n = 3$.

The adhesive strength of the hydrogel with different KCl concentrations is also investigated. The hydrogels are prepared in a film form with a dimension of 40 mm x 15 mm x 2 mm. KCl additive at different concentrations (0.5 M, 1 M, and 2 M) is added to the hydrogel precursor to prepare the hydrogel film. The 90-degree peeling test of the hydrogel films is conducted on a mechanical tester, with one half of the hydrogel film in contact with a plant leaf surface, and another end of the hydrogel film stretched to peel the hydrogel from the leaf surface (Figure 4.9). The hydrogel with 0.5 M and 1 M KCl shows the highest adhesive strength (14.3 N m^{-1} and 14.5 N m^{-1}, respectively). On the other hand, the hydrogel made from a 2 M KCl additive shows an adhesive strength of only 2.5 N m^{-1}. These results suggest that the hydrogels with KCl additive below 1 M have superior adhesiveness. For skin bioelectrode which requires some degree of adhesiveness, the KCl additive of 0.5 M and 1 M can be used to obtain the best combination of conductivity, transparency, and adhesiveness. One possible mechanism of hydrogel adhesion is attributed to the carboxyl group presented in the polymer chain of PAA. The functional carboxyl groups can form hydrogen bonds with other surfaces, prompting adhesion at the interface. For PAA hydrogels with excessive K^+ ions added. The carboxyl groups will be compensated due to charge neutralization, hindering the hydrogen bonding formation with other surfaces.

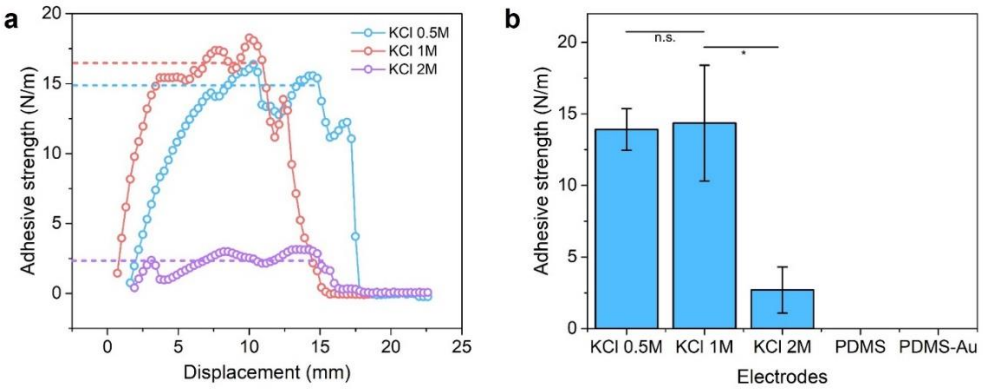

Figure 4.9 Adhesive strength of the hydrogel with KCl additive at different concentrations. (a) the adhesive strength measured from the mechanical tester. (b) the adhesive strength of hydrogel with different ionic additives. Hydrogel electrode area is 40 x 15 x 2 mm, KCl concentration in precursor solution is 0.5 M, 1 M, 2 M. The peeling off rate is 1 mm/s. Student's t-test: n.s. not significant, * $p < 0.005$, $n = 4$.

The prepared PAA hydrogel is a highly elastic material. To investigate its mechanical property, the stress-strain curve is measured in a mechanical tester (Figure 4.10 top). The hydrogel is prepared in a film with a dimension of 40 mm x 15 mm x 2 mm with a 1 M KCl concentration. The stress-strain test of the hydrogel is conducted in a mechanical tester. Two ends of the hydrogel are clipped by the two clippers of the mechanical tester. The hydrogel is stretched at a constant strain rate of 0.2 mm s^{-1}. The hydrogel shows a strain to rupture of 3.4, which means the hydrogel can be stretched to 340% of its initial length before the break (Figure 4.10 bottom). Such a stretchability is superior in skin bioelectrodes application, as the maximum strain skin can be stretched is around 70%.

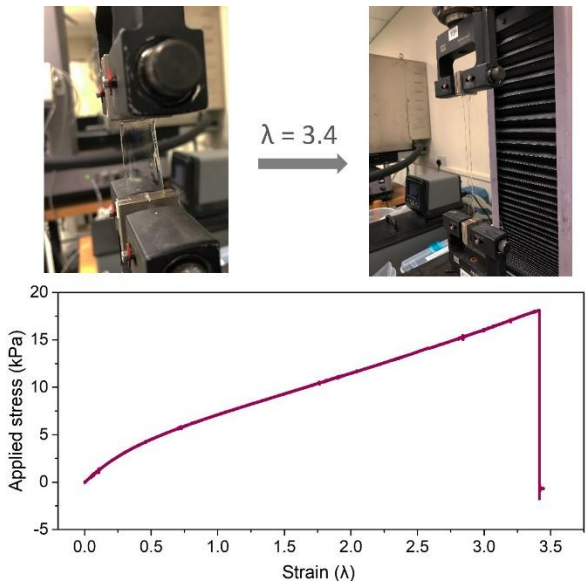

Figure 4.10 Mechanical stress-strain test of the hydrogel. The hydrogel is prepared in a film form with a dimension of 40 mm x 15 mm x 2 mm. KCl concentration used is 1 M. The stress-strain curve is measured in a mechanical tester MTS C42 with a 50 N load cell. The strain rate is set to 0.2 mm s^{-1}.

In a summary, the polyacrylic acid hydrogel was selected and optimized to reach superior properties in Young's modulus, adhesive strength, conductivity, and transparency. The Young's modulus (less than 5 kPa) can increase the comfort of the bioelectrode on the skin and accommodate the skin deformation. The adhesive strength (15.6 N/m) ensures the conformable attachment of bioelectrodes on the skin. The high ionic conductivity can increase the transduction of signals. The transparency (> 95%) allows easy observation of the skin condition during bioelectrode application. The collective properties make the polyacrylic acid hydrogel a superior choice compared with other commonly used electrode materials.

Table 4.1 Comparison of skin electrode-related properties of polyacrylic acid hydrogel compared with other common electrode materials.

	Young's modulus	**Adhesive strength**	**Impedance /Resistance**	**Transparency**	**Reference**
Acrylic hydrogel	5 kPa	16.5 N/m	780 Ω	95%	This work
PEDOT:PSS hydrogel	2MPa	Not adhesive	32 Ω	Not transparent	Nat. Commun. 10, 1043 (2019)
Silk fibroin hydrogel	150 kPa	60 N/m	500 Ω	95%	Adv.Mater.2021, 33, 2100221, Adv. Mater. 2018, 30, 1800129
Au-PDMS	1-2 MPa	Not adhesive	<10 Ω	Not transparent	Adv. Mater. 2019, 31, 1901360
AgNW-PDMS	1-2 MPa	Not adhesive	10 – 20 Ω	85%	ACS Appl. Mater. Interfaces 2020, 12, 5, 6169

4.4 Design and fabrication of Au nanomesh

Human skin surface presents complexed microstructures, hydrophobic oily substances, and extruding hairs is challenging. The conformal attachment on thin-film electrodes on the skin surface is challenging. Hydrogels, due to their low Young's modulus, high stretchability, high ionic conductivity, and rich water content, can serve as a skin contact layer for the ionic conductor. It conformally adheres to the skin due to its high adhesive strength and softness. The potential detected by hydrogel material needs to be further transduced into the electronic current to be measured by external amplifiers and ADC circuits. For this reason, when working as a skin bioelectrode material, hydrogel should have one side in contact with skin and the other side transduced its ionic current into the electronic current. Usually, an electronic conductor is covered on the hydrogel top layer. This electronic conducting layer should have a minimum interfacial impedance with hydrogel material, as transparent as the hydrogel, and conductive enough current transduction.

The Au nanomesh is synthesized as an electronic conductor in contact with the hydrogel layer for electronic current transduction. Au nanomesh was synthesized from a wet-

chemistry method (Figure 4.11)[5]. $NaBH_4$ as a reductant was added to the $HAuCl_4$ precursor solution. Au nanoparticle was formed by the drop-by-drop adding of $NaBH_4$. Toluene was added to create a water-toluene interface for the Au nanoparticle assembly. By vigorous agitation of synthesized Au nanoparticles in the water-toluene biphasic mixture, the Au nanoparticle undergoes coalescence driven by hydrophobic passivation to form Au nanowires, further inter-welding of Au nanowires results in a 3D mesh-like nanostructure at the water-toluene interface, which can be easily transferred to PDMS substrate After stirring. After careful removal of Au nanomesh by a pipette, the Au nanomesh film was ready for transfer printing. A homemade PDMS stamp was used to transfer the Au nanomesh. By carefully attaching PDMS film onto Au nanomesh film for around 30 s, Au nanomesh could be transferred onto the PDMS film.

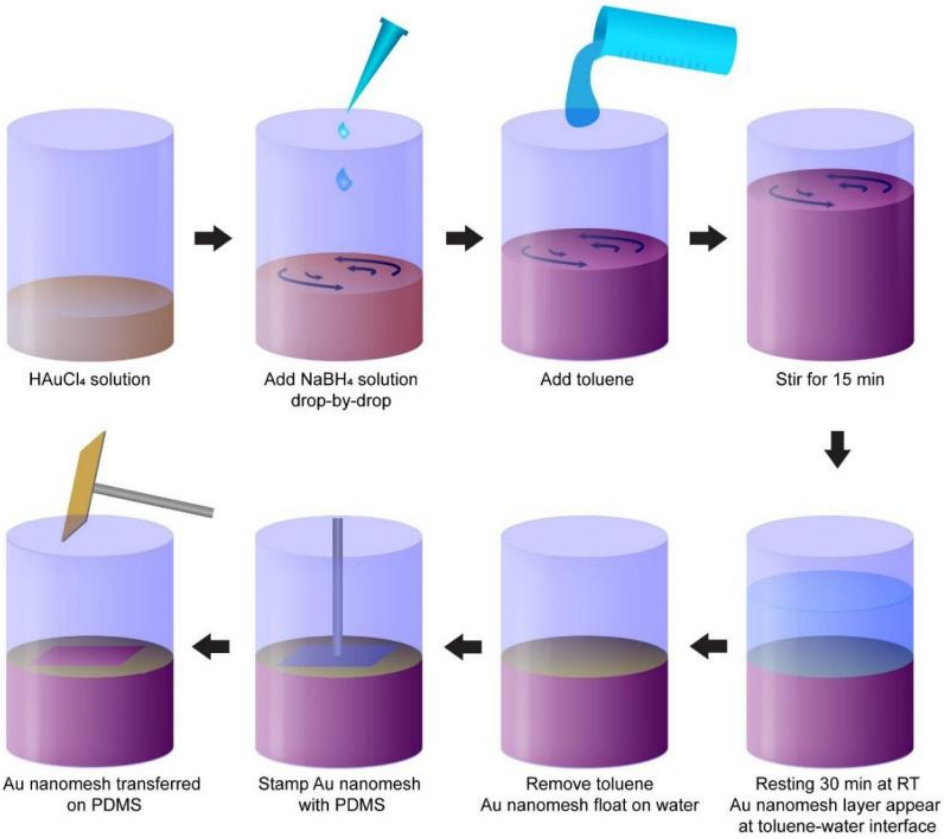

Figure 4.11 The synthesis scheme of Au nanomesh. Au nanomesh was synthesized from a wet-chemistry method. $NaBH_4$ as a reductant was added to the $HAuCl_4$ precursor solution. Au nanoparticle was formed by the drop-by-drop adding of $NaBH_4$. Toluene was added to create a water-toluene interface for the Au nanoparticle assembly. After stirring, Au nanoparticle self-

assembled into Au nanomesh, forming a thin layer of film at the water-toluene interface. After careful removal of Au nanomesh by a pipette, the Au nanomesh film was ready for transfer printing. A homemade PDMS stamp was used to transfer the Au nanomesh. By carefully attaching PDMS film onto Au nanomesh film for around 30 s, Au nanomesh could be transferred onto the PDMS film.

During the reduction of $HAuCl_4$ using $NaBH_4$, the solution shows a red-wine color, which is due to the generation of Au nanoparticles at a specific size. Au nanoparticles at different nanometer diameters can show different colors. To estimate the Au nanoparticle sizes, the UV-vis absorbance of the Au nanoparticle solution is measured using a UV-vis spectrophotometer (Figure 4.12). The Au nanoparticle solution shows a strong peak at 529 nm wavelength. This is due to the strong surface plasmon resonance (SPR) of Au nanoparticles in the solution. SPR is the transverse oscillations of particle surface electrons on interaction with the light of a suitable wavelength. Gold colloids usually have an absorption peak in the visible light range. The SPR peak of 529 nm in the UV-vis measurement indicates Au nanoparticles have a size of around 15 nm[6].

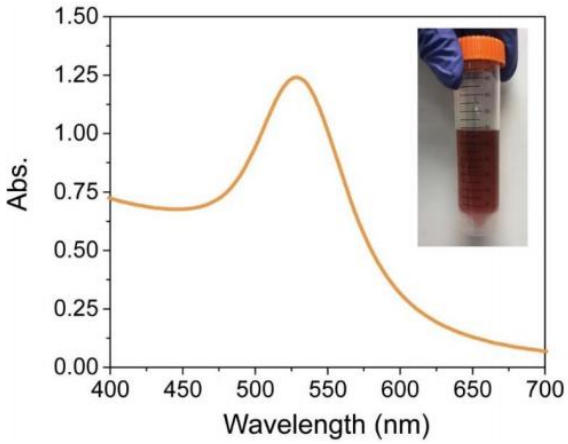

Figure 4.12 UV-vis spectrum of Au nanomesh solution. The Au nanoparticle solution shows a strong surface plasmon resonance (SPR) peak at 529 nm. SPR is the transverse oscillations of particle surface electrons on interaction with the light of a suitable wavelength. Gold colloids usually have an absorption peak in the visible light range. Here, the SPR peak of 529 nm indicates Au nanoparticle size of 15 nm.9 Inset: photograph of Au nanoparticle solution in Corning tube showing red-wine color.

The Au nanomesh morphology can be controlled and optimized to synthesize the most superior nanostructure for the best electrical and optical properties. As the Au nanomesh is synthesized by a reduction process using $NaBH_4$ to reduce $HAuCl_4$, the ratio of the reactive chemical species can be adjusted to investigate their influence on the synthesized Au nanomesh morphologies. During the synthesis process, different weight ratios of $HAuCl_4$ and $NaBH_4$ are used (1.5, 3.0, 4.5, 6.0, 7.5, $HAuCl_4/NaBH_4$). It turns out that the mesh-like nanostructure was maintained in different ratios (Figure 4.13). The nanowires interconnect for high electrical conductivity, while the hollow areas allow high transparency. Due to its best optical and electrical properties, 4.5 mg/mg was selected as the synthesis condition for all the applications (Figure 4.14).

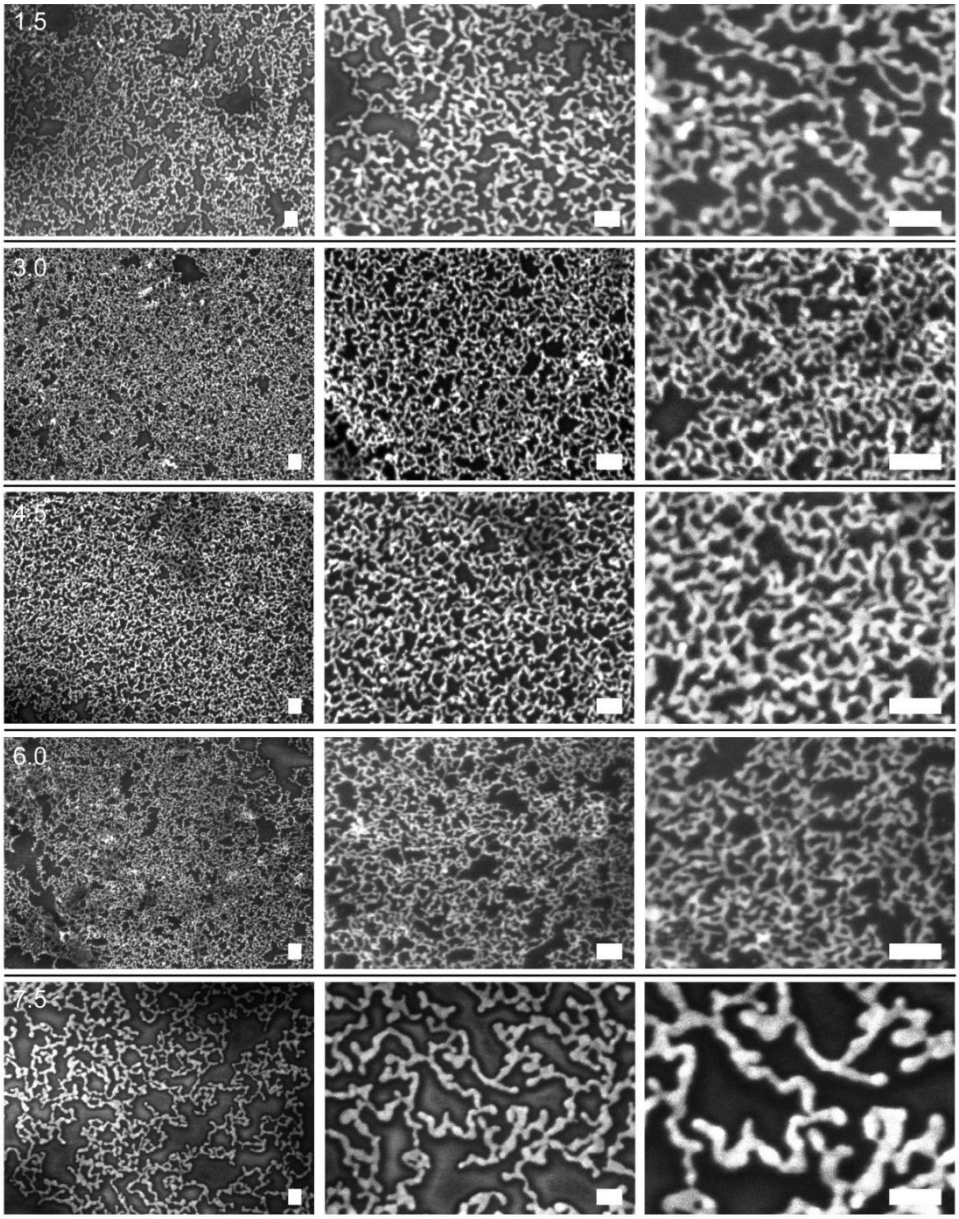

Figure 4.13 SEM image of Au nanomesh synthesized by different precursor ratios. The mesh-like nanostructure was maintained in different ratios. The nanowires interconnect for high electrical conductivity, while the hollow areas allow high transparency and gas exchange. Due to its best optical and electrical properties, 4.5 mg/mg was selected as the synthesis condition for all the applications. Scale bars, 100 nm.

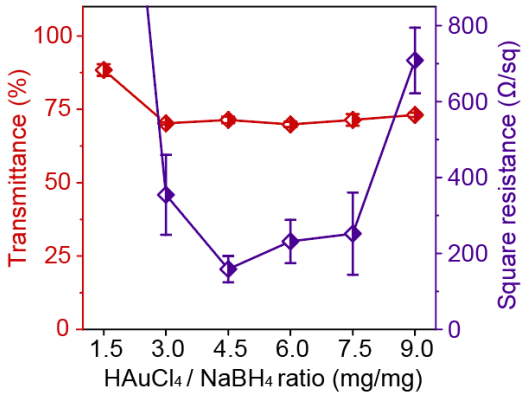

Figure 4.14 Optimization of the Au nanomesh film under different $HAuCl_4/NaBH_4$ weight ratio conditions. 4.5 mg/mg shows the highest transmittance and smallest square resistance.

The intertwined nanowire forms a 2D network which contributes to a continuous conductive film. To understand the electrical conduction property of the Au nanomesh, a simulation of the electrical potential distribution in an Au nanomesh film is conducted in Comsol simulation software. The distribution is uniform in the Au nanomesh despite its irregular hollow structure (Figure 4.15), indicating the minimized effects of the hollow structure on its electrical property uniformity. Such a uniform potential distribution is beneficial for electronic transduction. It means the Au nanomesh film can uniformly conduct current. This conduction uniformity is due to the high density of interconnection of the Au nanowires.

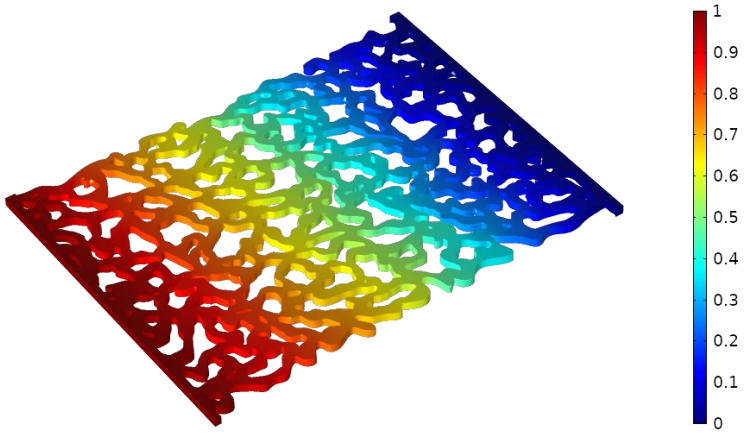

Figure 4.15 A simulation of the electrical potential distribution in an Au nanomesh film. The distribution is uniform in the Au nanomesh despite its irregular hollow structure, indicating the minimized effects of the hollow structure on its electrical property uniformity. The simulation was conducted in Comsol 5.5.

The nanostructure and crystal property of the synthesized Au nanomesh is further investigated by TEM. The freshly synthesized Au nanomesh on the water surface is lifted by a copper mesh TEM sample holder and observed by TEM after it is dried. From the TEM image, the Au nanomesh is formed by interconnected tortuous nanowire fragments (Figure 4.16a). The interconnected nanowires show a diameter of around 15 - 20 nm, agreeing with UV-vis results. A high-resolution TEM image shows the grain boundary between Au nanoparticle junctions (Figure 4.16b). The coalescence of Au nanoparticles is the primary mechanism of Au nanomesh formation. The crystal lattice interplanar spacing of Au nanomesh shows d-spacing equal to 0.236 nm (Figure 4.16c), corresponding to the interspacing distance of Au face-centered cubic (111) plane[7]. The face-centered cubic Au polycrystalline structure of the Au nanomesh is confirmed by the SAED (selected area electron diffraction) image (Figure 4.15d), showing diffraction rings corresponding to (111), (200), (220), (311).

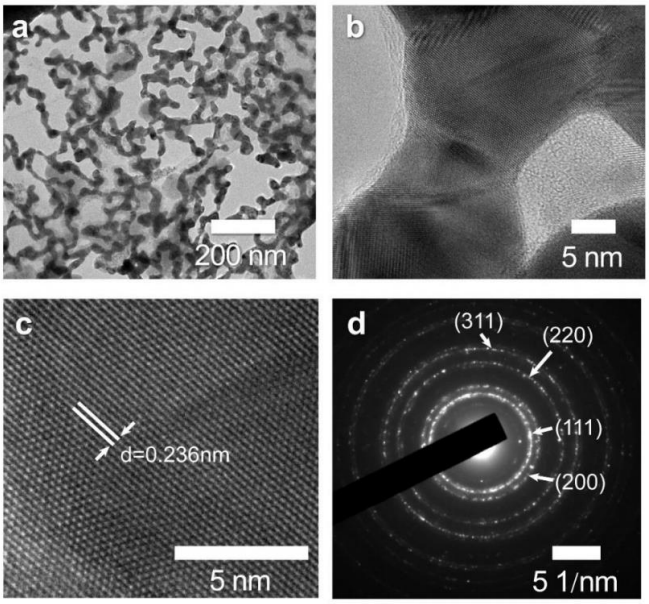

Figure 4.16 TEM characterization of Au nanomesh. (a) Au nanomesh as lifted from the water-toluene interface. The Au nanomesh is formed by interconnected tortuous nanowire fragments. The interconnected nanowires show a diameter of around 15 - 20 nm, agreeing with UV-vis results. (b) A high-resolution TEM image shows the grain boundary between Au nanoparticle junctions. The coalescence of Au nanoparticles is the primary mechanism of Au nanomesh formation7. (c) The crystal lattice interplanar spacing of Au nanomesh shows a d-spacing equal to 0.236 nm, corresponding to the interspacing distance of Au face-centered cubic (111) plane10, 11. (d) SAED (selected area electron diffraction) image of the Au nanomesh, showing diffraction rings corresponding to (111), (200), (220), (311) of face-centered cubic Au polycrystalline nanocrystals.

The Au nanomesh is synthesized at the water-toluene interface. After removing toluene and fully evaporation of toluene residual, the Au nanomesh film can be easily transferred onto a PDMS substrate film, forming Au nanomesh-PDMS electronic conductor. Such conductors can be used in conjunction with previously synthesized adhesive hydrogel to make conformal skin bioelectrodes. Due to its hollow nanostructure, the Au nanomesh-PDMS is also transparent. The photo of Au nanomesh on PDMS film (with a dimension of 2 cm x 2 cm) green leaf background, indicating its high transparency (Figure 4.17a). The Au nanomesh-PDMS film transparency can be further quantified by UV-vis spectrum (Figure 4.17b). The film shows 69% transmittance at the 450-nm wavelength and 71% transmittance at the 650-nm wavelength. The SEM image of the Au nanomesh-PDMS film

reflects the origin of its transparency from a nanostructure perspective (Figure 4.17c). The porous area of the nanomesh allows effective light transmittance of the film. In addition, the conductivity of the film comes from its intertwined 2D network. The tortuous Au nanowires provide the film with superior stretchability. The thickness of the nanomesh is around 20 – 50 nm. The thickness of the Au nanomesh can be increased by transferring multiple layers of Au nanomesh on PVA in our transfer printing technique. Increasing the Au nanomesh thickness would increase the conductivity at the expense of reducing transparency. As such, for the skin bioelectrode application, single-layer Au nanomesh with good conductivity and transparency would be a superior choice.

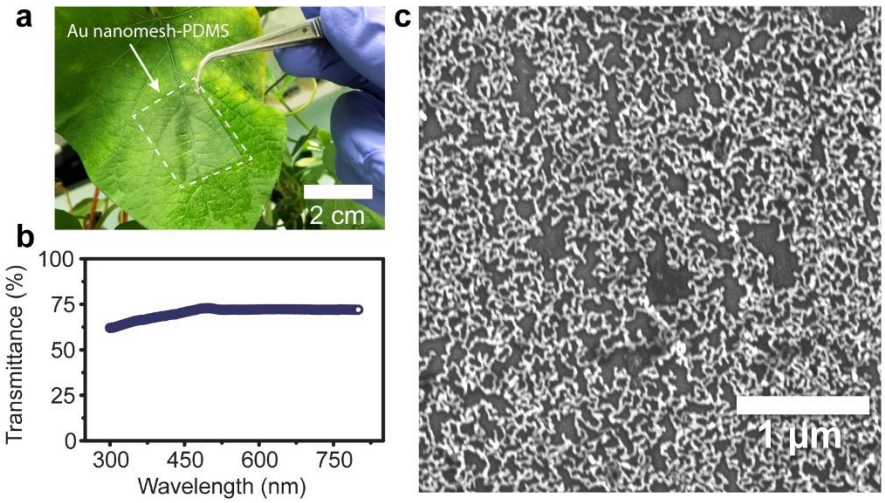

Figure 4.17 Transparency of Au nanomesh-PDMS film. (a) Photograph of Au nanomesh on PDMS film (2 cm x 2 cm) showing its transparency. The Au nanomesh-PDMS film is indicated by a white dashed box. (b) UV-vis spectrum of the Au nanomesh-PDMS film. Plants are responsive to blue (~450 nm) and red (~650 nm) light for photoactivity. The film shows 69% transmittance at the 450-nm wavelength and 71% transmittance at the 650-nm wavelength, indicating the film is transparent enough for light absorption of plants. (c) FESEM image of the Au nanomesh on PDMS film reflects the origin of its transparency from a nanostructure perspective. The porous area of the nanomesh allows effective light transmittance of the film. In addition, the conductivity of the film comes from its intertwined 2D network. The tortuous Au nanowires provide the film with superior stretchability.

The Au nanomesh maintains its conductivity due to the interconnected nanowire structure. The mesh-like structure also endows the Au nanomesh structure with high conductivity even under stretching. The electrical characteristics of Au nanomesh-PDMS film are studied under a mechanical tester and digital multimeter. The film is cut into a rectangular shape with a dimension of 3 cm x 1 cm. Two ends of the film are fixed with a clipper and the film is stretched at a constant rate (0.2 mm s^{-1}). The digital multimeter is connected to the two ends of the film through liquid metal and copper wires. The cycling test of the Au nanomesh-PDMS film is first conducted. The film was cycled at a 50% strain for 200 cycles, showing that the electrode is mechanically and electrically stable during the cycling test (Figure 4.18a). It is also noted that during cycling the highest resistance at maximum strain is reduced. This phenomenon is commonly seen in stretchable Au electrodes, which is possibly due to the cold-welding effect of Au during mechanical strain. The stretchability test of Au nanomesh-PDMS film. The stretchability indicates the maximum strain that the film keeps conductive. The film shows good electrical insensitivity upon stretching. R/R_0 keeps at 10 at a strain of 120%, and the film keeps conductive until 135% (Figure 4.18b).

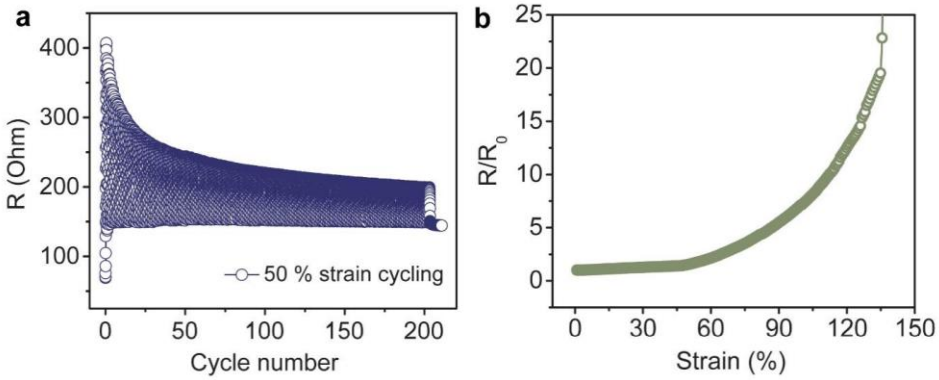

Figure 4.18 Electrical characteristics of Au nanomesh-PDMS film. (a) Cycling test of the Au nanomesh-PDMS film. The film was cycled at a 50% strain for 200 cycles, showing that the electrode is mechanically and electrically stable during the cycling test. It is also noted that during cycling the highest resistance at maximum strain is reduced. This phenomenon is commonly seen in stretchable Au electrodes, which is possibly due to the cold-welding effect of Au during mechanical strain. (b) Stretchability test of Au nanomesh-PDMS film. The film shows good electrical insensitivity upon stretching. R/R_0 keeps at 10 at a strain of 120%, and the film keeps conductive until 135%.

The Au nanomesh is synthesized and characterized as an electronic transduction layer, which means it works with hydrogel to transduce hydrogel's ionic current into electronic current through capacitive coupling. As such, the interface between the Au nanomesh and the hydrogel is very important. Such an interface would contribute to most of the impedance of a hydrogel-Au nanomesh conductor. To quantitatively characterize the interfacial property, interfacial current conduction between the adhesive hydrogel and Au nanomesh interface was measured by EIS (Figure 4.19). As a comparison, CNT, AgNW, and Al foil were also tested as control experiments. All the sizes of electrode films were kept at 2 cm x 1 cm, the size of hydrogel was kept at 1 cm x 1 cm. The device was configured into an electrode-hydrogel-electrode symmetric sandwich structure. In such a configuration, the total conductance of such a sandwich structure comes from the conductance of two electrode film layers, one hydrogel layer, and two electrode-hydrogel interfaces. To make sure only the conductance of the electrode-hydrogel interface is comparable between different electrode materials, the conductance of different electrode films was kept the same. Au nanomesh film shows the highest admittance with adhesive hydrogel compared with CNT, AgNW, and Al foil, which is due to its nanomesh-like structure and relatively large contacting area with hydrogel.

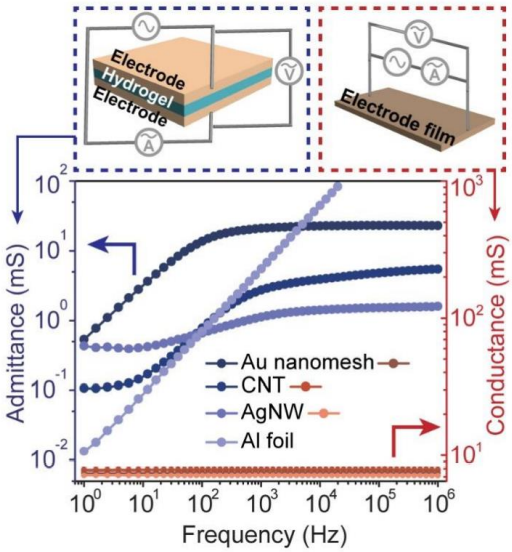

Figure 4.19 Interfacial current conduction between the adhesive hydrogel and Au nanomesh interface measured by EIS. As a comparison, CNT, AgNW, and Al foil were also tested as control

experiments. All the sizes of electrode films were kept at 2 cm x 1 cm, the size of hydrogel was kept at 1 cm x 1 cm. The device was configured into an electrode-hydrogel-electrode symmetric sandwich structure (as shown in the top schematic). In such a configuration, the total conductance of such a sandwich structure comes from the conductance of two electrode film layers, one hydrogel layer, and two electrode-hydrogel interfaces. To make sure only the conductance of the electrode-hydrogel interface is comparable between different electrode materials, the conductance of different electrode films was kept the same (right y-axis). Au nanomesh film shows the highest admittance with adhesive hydrogel compared with CNT, AgNW, and Al foil (left y-axis), which is due to its nanomesh-like structure and relatively large contacting area with hydrogel. Top: Schematic of device configuration.

References

[1] G. Chen, N. Matsuhisa, Z. Liu, D. Qi, P. Cai, Y. Jiang, C. Wan, Y. Cui, W. R. Leow, Z. Liu, S. Gong, K.-Q. Zhang, Y. Cheng, X. Chen, Advanced Materials 2018, 30, 1800129.

[2] Y. Ohm, C. Pan, M. J. Ford, X. Huang, J. Liao, C. Majidi, Nature Electronics 2021, 4, 185; C. Yang, Z. Suo, Nature Reviews Materials 2018, 3, 125; H. Fang, K. J. Yu, C. Gloschat, Z. Yang, E. Song, C.-H. Chiang, J. Zhao, S. M. Won, S. Xu, M. Trumpis, Y. Zhong, S. W. Han, Y. Xue, D. Xu, S. W. Choi, G. Cauwenberghs, M. Kay, Y. Huang, J. Viventi, I. R. Efimov, J. A. Rogers, Nature Biomedical Engineering 2017, 1, 0038.

[3] H. Yuk, T. Zhang, G. A. Parada, X. Liu, X. Zhao, Nature Communications 2016, 7, 12028.

[4] M. Wang, Z. Yan, T. Wang, P. Cai, S. Gao, Y. Zeng, C. Wan, H. Wang, L. Pan, J. Yu, S. Pan, K. He, J. Lu, X. Chen, Nature Electronics 2020, 3, 563.

[5] G. Ramanath, J. D'Arcy-Gall, T. Maddanimath, A. V. Ellis, P. G. Ganesan, R. Goswami, A. Kumar, K. Vijayamohanan, Langmuir 2004, 20, 5583; M. D. Ho, Y. Liu, D. Dong, Y. Zhao, W. Cheng, Nano Letters 2018, 18, 3593; W. Li, N. Matsuhisa, Z. Liu, M. Wang, Y. Luo, P. Cai, G. Chen, F. Zhang, C. Li, Z. Liu, Z. Lv, W. Zhang, X. Chen, Nature Electronics 2021, 4, 134.

[6] R. Das, S. S. Nath, R. Bhattacharjee, Journal of Nanomaterials 2011, 2011, 630834.

[7] C. J. Johnson, E. Dujardin, S. A. Davis, C. J. Murphy, S. Mann, Journal of Materials Chemistry 2002, 12, 1765; Y. Q. Wang, W. S. Liang, C. Y. Geng, Nanoscale Research Letters 2009, 4, 684.

Chapter 5

Antimicrobial hydrogel electrode materials

This chapter details the design, fabrication, optimization, and characterization of silk-based hydrogel materials with antimicrobial properties. The hydrogel is made from the co-assembly of silk fibroin and Fmoc-protected amino acids. The hydrogel is formed with very fast gelation kinetics (within two minutes). Also, Fmoc-Leu-OH presents gram-positive antimicrobial property for the hydrogel. With these benefits, the assembly silk fibroin hydrogel with Fmoc-protected amino acids showed promising killing efficiency against gram-positive B. subtilis. In addition, a tough, wearable, conformal, and antimicrobial hydrogel with silk fibroin and PAAm hydrogel is also presented.

5.1 Introduction

Skin pathogen infection is one of the easiest ways for pathogen transmission if no proper treatment is engaged[1]. The skin pathogen infection can cause skin inflammation, skin biofilm formation, and delayed skin wound healing.[2] In this regard, when designing skin-contacting electrode materials, antimicrobial properties should be considered to avoid biofilm formation on the skin due to long-term coverage of the skin. Silk fibroin, a natural protein produced from Bombyx mori, has drawn great attention recently due to its biocompatibility, biodegradability, high water, and oxygen uptake, low immunogenicity, and tunable mechanical properties.[3] However, the intrinsic drawback of silk fibroin-based hydrogel materials is that it is not bacteria-resistant, and Young's modulus of silk fibroin hydrogel is not comparative with human skin. To this end, we propose a facile way to form silk fibroin hydrogel by simply assembly silk fibroin with Fmoc-protected amino acids. This procedure has very fast gelation kinetics (within two minutes), which is faster than most currently applied silk fibroin gelation methods[4]. Also, it is reported that one of the Fmoc-protected amino acids, Fmoc-Leu-OH (abbreviated as Fmoc-L) presents gram-positive antimicrobial property. With these benefits, the assembly silk fibroin hydrogel with Fmoc-protected amino acids showed promising killing efficiency against gram-positive B. subtilis and can be potentially used as electrode hydrogel materials.

When Fmoc-L, one type of the Fmoc-protected amino acids were used, the impressive gram-positive antibacterial activity of the silk fibroin hydrogel is presented. However, despite the excellent antibacterial property of such silk fibroin hydrogel, it has relatively poor mechanical properties. For skin bioelectrode material it is usually desired to have a hydrogel patch that can be directly applied to the skin. In addition to good biocompatibility and antimicrobial property, the requirement for such patchable hydrogel material also includes a mechanically robust structure so that a flexible freestanding film can form and accommodate possible deformation on the skin. Unfortunately, the silk fibroin hydrogel is not able to work in such requirements. For this reason, a tough, wearable, and conformable hydrogel with silk fibroin and the chemical hydrogel is developed. The chemical hydrogel, PAAm, is made from polymerization and crosslinking acrylamide (AAm) into a covalent

3D network structure. The biocompatibility and antimicrobial activity on this tough hydrogel platform need to be further explored.

5.2 Experimental methods

5.2.1 Preparation of silk fibroin solution

Silk fibroin solution was prepared according to a previous report (Figure 5.1)[5]. Briefly, 10 g anhydrous Na_2CO_3 was added to 2 L DI water to allow thorough dissolution. 10 g Bombyx mori silk fibers were cut into 1 cm pieces and boiled in the 2 L Na_2CO_3 solution for 1 hour. The boiled silk pieces were washed with DI water 6 times thoroughly to remove sericin residues. The degummed silk pieces were then dried in an oven at 60 °C overnight. 5 g dried silk pieces were dissolved in 20 mL 9.8 M LiBr solution for 4 h at 60 °C. The solution would turn to dark yellow after 4h. It was then dialyzed in a dialyzing tube (3K Da) in a beaker with 2 L DI water to remove ions from the silk fibroin solution. The DI water was changed every 1h, 2h, 4h, 8h, and 24h. After dialysis, the silk fibroin solution was stored at 4 °C for later use.

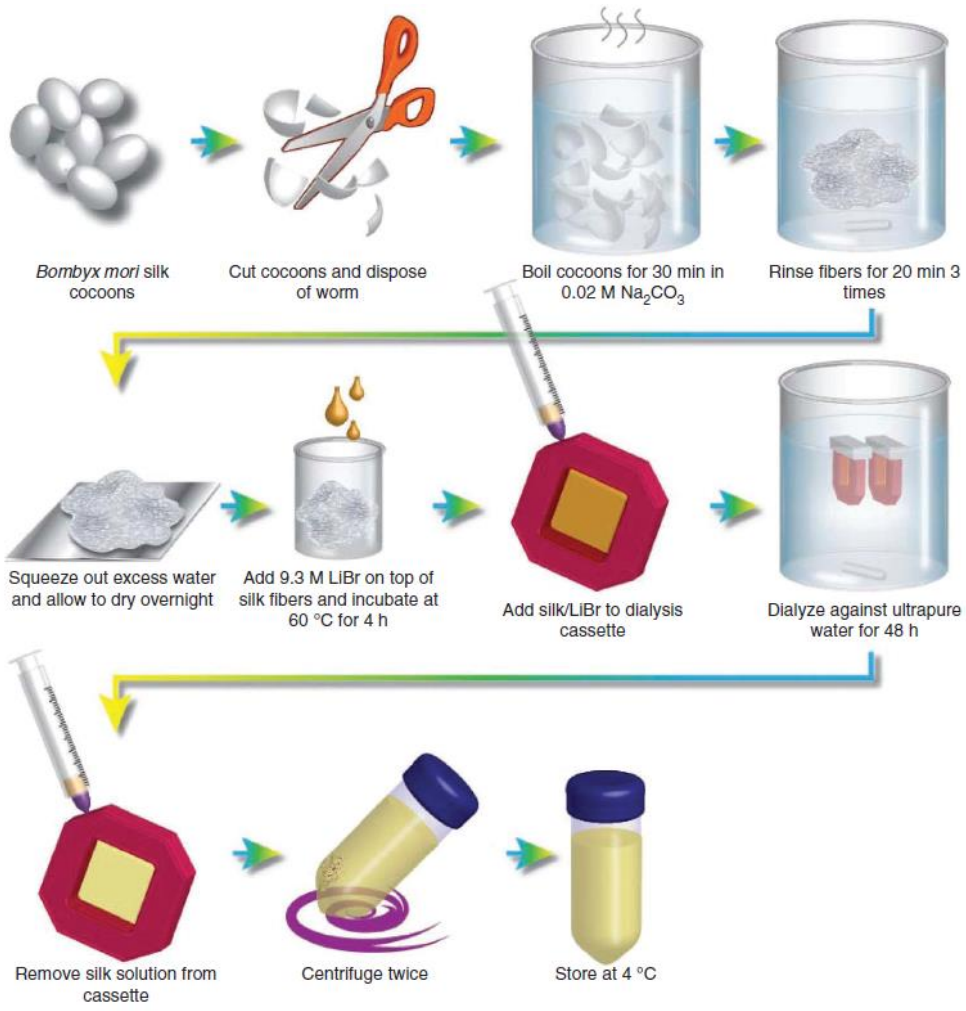

Figure 5.1 Fabrication process of silk fibroin solution. The process roughly includes three steps. The first step is to boil the raw silk cocoons material in Na_2CO_3 to remove the surface sericin layer of silk fiber. The second step is to dissolve silk fibroin fiber into LiBr aqueous solution. The last step is to dialyze the silk/LiBr solution to remove excessive ions. Figures reproduced from Ref[6].

5.2.2 Silk fibroin gelation with Fmoc protected amino acids

Silk fibroin concentration (50 mg mL^{-1}) was determined by a drop-and-dry method in a petri dish. The gelation process was first confirmed by a vial inversion method (Figure 5.2). First, Na_2CO_3 was added to the silk fibroin solution to make a final concentration of Na_2CO_3 as 0.1 M in the silk solution. Then, 500 μL silk solution was added to a 4 mL vial. 10 mg Fmoc-Leu-OH was then added to the silk solution. The vial was put in a water bath

(70 °C) heated on a hot plate for 2 min. For the preparation of other Fmoc protected amino acids, the same procedure was followed besides that Fmoc-Leu-OH was replaced by other Fmoc protected amino acids.

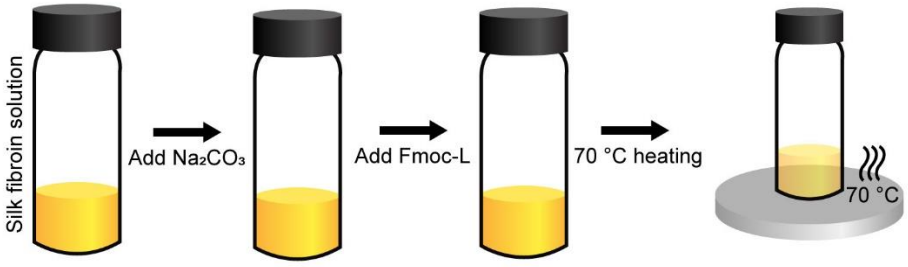

Figure 5.2 Preparation scheme of the co-assembly of silk fibroin and Fmoc-protected amino acids.

5.2.3 FTIR spectrum study of co-assembled silk hydrogel

The silk hydrogel assembled by Fmoc protected amino acids were first studied by FTIR (Perkin Elmer Frontier) under the Attenuated Total Reflection (ATR) mode. The co-assembled silk fibroin hydrogel was first frozen at -80 °C for 24 hours, and subsequently lyophilized for 48 hours. The lyophilized silk fibroin sample was crushed and mixed with potassium bromide at a mass ratio of 1:20. The mixture was grinded with a mortar and pestle to a collection of fine powder. The powder was pressed into a thin rigid film using Specac Manual Hydraulic Press. The film was scanned from 4000 cm^{-1} to 650 cm^{-1} with 16 scans per sample.

5.2.4 UV-vis transmittance spectrum study of co-assembled silk hydrogel

UV-vis transmittance spectrum of co-assembled silk fibroin hydrogel was obtained from Shimadzu UV-2550 UV-vis spectrophotometer. Co-assembled silk fibroin hydrogel was first fabricated in a 30-mm transparent polystyrene petri dish. The petri dish was adhered to a sample holder using double tape. It was scanned from 800 nm to 300 nm under transmission mode.

5.2.5 SEM study of silk fibroin hydrogel assembled by Fmoc amino acids

The morphology of co-assembled silk fibroin hydrogel was studied by field emission scanning electron microscope (FESEM, JEOL JSM-6340F). To prepare the sample for SEM image, the co-assembled silk fibroin hydrogel was first frozen at -80 °C for 24 hours, and subsequently lyophilized for 48 hours. The lyophilized sample was subsequently mounted on a carbon tape of SEM stub, and vacuum sputtered with fine gold layer to avoid surface charging issue under SEM operation. The vacuum sputtering was conducted at a current of 20 mA and a time duration of 15 s. The prepared SEM sample was then observed in SEM with an accelerating voltage of 5 kV.

5.2.6 Bacteria culture

Two types of bacteria were used in our experiment for the antimicrobial property evaluation of our material, one is gram-positive Bacillus subtilis (B. subtilis) and another one is gram-negative Escherichia coli (E. coli). Before the bacteria were used for the experiment, they were grown into an exponential phase overnight in Luria-Bertani (LB) broth medium. The appearance of LB solution turned from clear yellowish to turbid, indicating the existence of bacteria suspension in the LB solution. To harvest the cultured bacteria, the desired amount of the bacteria solution was taken and centrifuged at 8000 rpm for 5 min, the supernatant was discarded, and the pellet was resuspended in 0.85% NaCl aqueous solution. The bacteria in 0.85% NaCl aqueous solution was centrifuged at 8000 rpm for 5 min again, and further resuspended in 0.85% NaCl aqueous solution for further use.

5.2.7 Agar spreading plate experiment for colony-forming unit counting

100 μL of stock solution of bacteria in 0.85% NaCl was dipped on the surface of co-assembled silk fibroin hydrogel inside a petri dish (30 mm diameter). The hydrogel treatment was maintained for 1 hour. As a control experiment, another group of 100 μL

bacteria stock solution was dropped in an empty petri dish and allowed to rest for the same time as the hydrogel treatment. After 1-hour treatment, 100 μL 0.85% NaCl solution was added to both petri dishes, the surface of hydrogel was washed, and the solution was taken from the hydrogel surface into a 1.5 mL vial tube. The treated bacteria solution was serially diluted by 105 times in LB solution. 100 μL of the diluted bacteria LB solution was dipped on the agar plate, spread thoroughly, and incubated in an oven at 34 °C for 12 hours. After the incubation, the plates were taken out and the bacteria colony-forming unit (CFU) was counted in ImageJ (Figure 5.3). The counting method was illustrated in Figure 3.3. If the counted number on the plate from ImageJ is N, then the live bacteria concentration in the initial bacteria solution would be:

$$Bacteria\ Concentration = \frac{N(CFU)}{0.1mL} \times 10^5 = N \times 10^6(\frac{CFU}{mL})$$

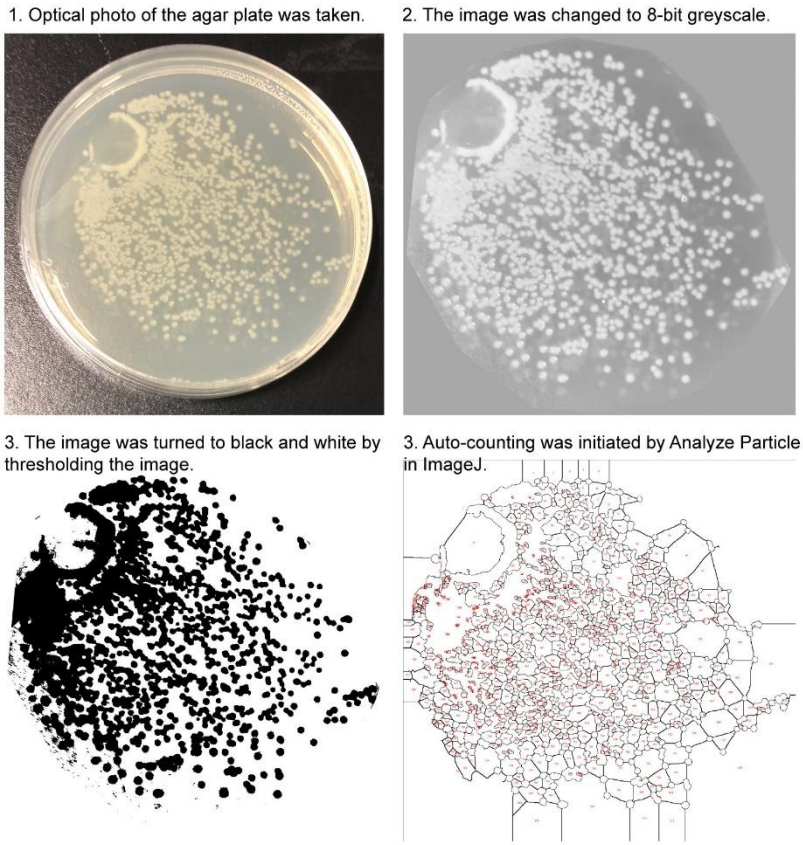

Figure 5.3 Agar spreading plate method to count bacteria colony-forming units in ImageJ.

5.2.8 LIVE/DEAD bacteria fluorescence staining

LIVE/DEAD bacteria fluorescence staining experiment was conducted using LIVE/DEAD BacLight Bacterial Viability Kits (Invitrogen, L13152). The viability kits contain two types of stains sealed in an applicator set: the SYTO 9 for green-fluorescent nucleic acid stain and propidium iodide for red-fluorescent nucleic acid stain. Each stain in the applicator was dissolved in 2.5 mL of DI water and mixed. The mixed stain solution was wrapped with aluminum foil and stored in a 4°C refrigerator to avoid light. When staining the treated bacteria solution (the bacteria treatment was described in Section 3.6. Bacteria Culture). 100 μL of the treated bacteria solution was mixed with 100 μL of the prepared SYTO9/PI staining solution, resting in dark for 20 min to allow the stains to enter the bacteria cell membrane. After that, 5 μL of the bacteria-stained solution was dipped on a glass coverslip, the coverslip was covered with an 18 mm square coverslip. The coverslip was observed using Nikon Ti2 Inverted Research Microscope. Green fluorescence and red fluorescence were captured using GFP and TRITIC filters, respectively.

5.2.9 Preparation of PAAm hydrogel and silk-PAAm hydrogel

For the preparation of PAAm hydrogel, 0.4 g (13 wt%), 0.6 g (20 wt%), and 0.8 g (27 wt%) AAm monomers were added into 3 mL DI water, respectively. Then 10 mg potassium persulfate was added as thermal initiator, 10 μL N,N,N',N'-tetramethylethylenediamine was added as an accelerator, 1.7 mg N,N'-methylenebisacrylamide was added as crosslinker. The solutions were vortexed to allow fully dissolved. Then some amount of the dissolved solution was dropped into a PDMS mold on a glass plate. The top of the mold was covered by a petri dish to prevent water dry out when heated. Finally, the solution in the PDMS mold was put in the oven to heat at 60 °C for 12 min. The hydrogel was obtained by peeling the hydrogel off from the mold. The as-obtained hydrogel was annealed at room temperature in 87% ethanol for 6 hours and subsequently in water for 24 hours. For the preparation of Silk-PAAm hydrogel, the procedure keeps the same, but the 3 mL DI water was replaced by a 3 mL silk solution (5 wt%).

5.2.10 Characteristic study of PAAm hydrogel and silk-PAAm hydrogel

For light microscope study of the surface feature of hydrogel, as-prepared PAAm and Silk-PAAm hydrogel was observed in the light microscope (Zeiss Axioscope) in reflection mode.
For FTIR study of the chemical information of hydrogel, the as-prepared hydrogel was first heated in the oven for 24 hours to remove residual water, then the dried hydrogel film was cut into smaller sizes and measured in FTIR (Perkin Elmer Frontier) under the ATR mode.

For SEM study of the microstructure of the hydrogel, the as-prepared hydrogel was first frozen at -80 °C for 24 hours, then it was lyophilized for 48 hours to remove water. The lyophilized hydrogel was mounted onto carbon tape of an SEM stub, and vacuum sputtered a fine layer of gold. The vacuum sputtering condition was set as 20 mA and 15 s, this would deposit a gold layer with a thickness estimated less than 10 nm. The prepared SEM sample was then observed in SEM with an accelerating voltage of 5 kV.

For the study of fluorescence emission of the hydrogel. The hydrogel was put into a cuvette and measured in a fluorescence spectrophotometer (Agilent Technologies Cary Eclipse Fluorescence Spectrophotometer), the excitation wavelength was set at 280 nm and the emission wavelength was collected at a range between 300 nm and 450 nm.

5.3 Fmoc-protected amino acids assembled silk fibroin hydrogel with antimicrobial properties

Silk fibroin materials have been regarded as a promising candidate for biomedical-related applications such as tissue engineering and regenerative medicine to repair or regrow dead or damaged tissue, wound treatment to promote faster wound healing, and drug delivery to facilitate more controllable drug delivery[7]. The benefits of silk fibroin to such a broad spectrum of application arise from its superior biocompatibility, negligible immunogenicity, and desired biodegradability[8]. However, as a biomaterial with such a

promising application potential, silk fibroin faces the problem of being vulnerable to the microbiome, and silk itself has no resistance to bacterial infection. To be applied as antimicrobial skin bioelectrode material, it must sustain some ability to resist bacterial colonization, or even to effectively remove and kill bacteria. Traditional methods are to physically absorb or chemically crosslink silk fibroin hydrogel with some antibiotics, silver nanoparticles, or antimicrobial polymers[9]. However, these processes either suffered from the complicated fabricating process or low loading efficiency, thus compromising the antimicrobial property of silk fibroin hydrogels. To this end, a facile way to form silk fibroin hydrogel by simply assembly silk fibroin with Fmoc-protected amino acids is developed. This procedure has very fast gelation kinetics (within two minutes), which is faster than most currently applied silk fibroin gelation methods[4]. Also, it is reported that one of the Fmoc-protected amino acids, Fmoc-Leu-OH (abbreviated as Fmoc-L) presents gram-positive antimicrobial property. With these benefits, it would be very promising to assembly silk fibroin hydrogel with Fmoc-protected amino acids.

Co-assembled silk fibroin solution with 12 types of Fmoc-protected amino acids is conducted to evaluate their ability to assembly silk fibroin into the hydrogel. The 12 types of Fmoc-protected amino acids include (Figure 5.4): Fmoc-Ile-OH, Fmoc-Phe-OH, Fmoc-Lys(Boc)-OH, Fmoc-Thr(tBu)-OH, Fmoc-Asp(OtBu)-OH, Fmoc-Leu-OH, Fmoc-Glu(OtBu)-OH, Fmoc-Met-OH, Fmoc-Thr(tBu)-OH, Fmoc-Gly-OH, Fmoc-Ala-OH, and Fmoc-Ser(tBu)-OH. First, we added Na_2CO_3 to freshly dialyzed silk fibroin solution (5 wt%) to make the concentration of Na_2CO_3 in the silk solution to 0.1 M. The addition of Na_2CO_3 to silk fibroin solution is to allow the Fmoc-protected amino acids to be dissolved in the silk fibroin solution. Without Na_2CO_3 addition, the Fmoc-protected amino acids could not be dissolved in silk solution no matter heating, vertexing, or sonicating. After the addition of Na_2CO_3, Fmoc-protected amino acids were subsequently added with a weight of 10 mg Fmoc-protected amino acids to 500 μL silk fibroin solution. The mixed solution was heated in a water bath at 70 °C to allow gelation to take place. The vial tubes were frequently inverted to check the gel formation. If the gel forms, they wound stick on the bottle of the vial tube, if the sol remains, they will flow as the vail tube is inverted.

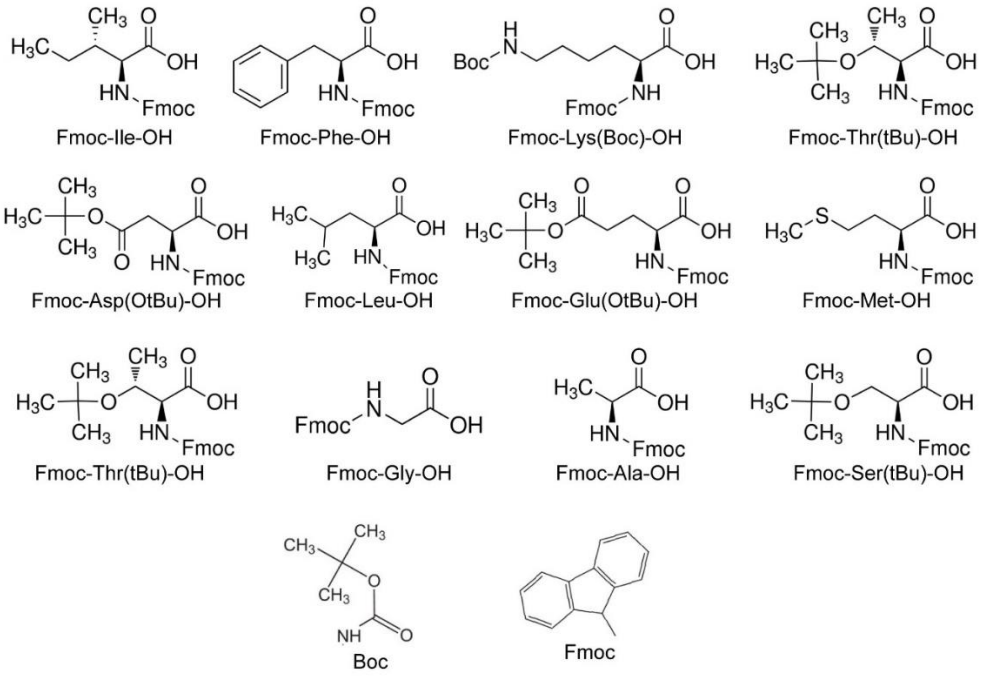

Figure 5.4 Chemical structures of the 12 types of Fmoc-protected amino acids.

Surprisingly, all of them showed gelation behavior with silk fibroin, but with different gelation kinetics and optical transparency (Figure 5.5). Some of the Fmoc-protected amino acids can promote the gelation within one minute and some other gelation processes need more than ten minutes to finish. In addition, some of the gels are relatively transparent while some showed a white opaque appearance. The deviation in gelation kinetics and optical properties due to different Fmoc-protected amino acids requires further detailed study.

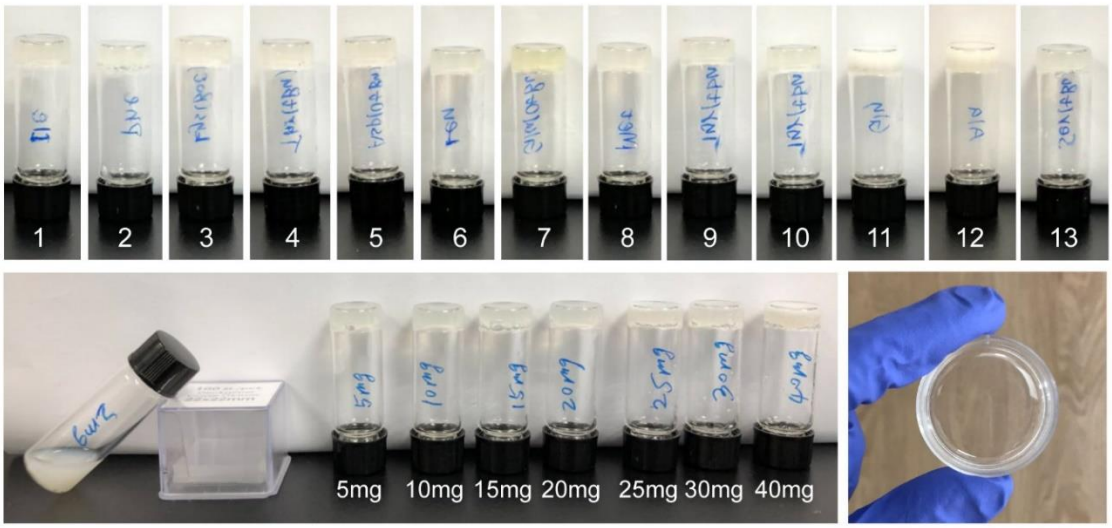

Figure 5.5 Photograph images of assembled silk hydrogel by Fmoc-protected amino acids. Each vial tube was filled with 500 μL silk solution and 10 mg Fmoc-protected amino acids. (a) A series of vial inversion methods to verify the gelation of silk with different types of Fmoc-protected amino acids. From 1 to 12, 1: Fmoc-Ile-OH, 2: Fmoc-Phe-OH, 3: Fmoc-Lys(Boc)-OH, 4: Fmoc-Thr(tBu)-OH, 5: Fmoc-Asp(OtBu)-OH, 6: Fmoc-Leu-OH, 7: Fmoc-Glu(OtBu)-OH, 8: Fmoc-Met-OH, 9: Fmoc-Thr(tBu)-OH, 10: Fmoc-Gly-OH, 11: Fmoc-Ala-OH, 12: Fmoc-Ser(tBu)-OH. (b) Vial inversion method to verify the gelation of silk by Fmoc-Leu-OH with different weights. 2 mg of Fmoc-Leu-OH would not be able to promote the formation of silk, while a weight of 5 mg to 40 mg can promote the formation of silk. (c) Assembled silk hydrogel from 1 mL silk solution in a 30 mm petri dish, the thin layer of hydrogel has a transparent appearance.

Fmoc-L is an antimicrobial building block to effectively kill gram-positive bacteria[10]. The antimicrobial property is from the leucine derivative that is reported to intrinsically possess anti-inflammatory and antibacterial properties[11], peptides that are rich in leucine amino acids have an important role in gram-positive bacterial recognition[12]. From our findings that Fmoc-protected amino acids (including Fmoc-L) can effectively promote the gelation of silk fibroin, we hypothesize that Fmoc-L assembled silk firoin hydrogel would sustain gram-positive antimicrobial properties, thus making the assembled silk a promising hydrogel material with intrinsic anti-inflammatory and anti-bacterial properties.

To further confirm the gelation condition of Fmoc-L with silk fibroin, the mass ratio of Fmoc-L was tuned. Into 500 μL silk fibroin solution, 2 mg, 5 mg, 10 mg, 20 mg, 30 mg,

and 40 mg Fmoc-L was added and heated in a water bath at 70 °C, respectively. The gelation was monitored by the vial inversion method. Remarkably, 2 mg of Fmoc-L could not allow silk fibroin to gelation even for one day. On the other hand, 5 mg, 10 mg, 20 mg, 30 mg, and 40 mg Fmoc-L can assemble silk fibroin into the hydrogel. However, as the Fmoc-L mass increases, the appearance of hydrogel turned into white and opaque, which is probably due to the insolubility of excessive Fmoc-L. When the hydrogel was made thin in a petri dish with 20 mg Fmoc-L in 1 mL silk solution, transparent silk hydrogel was made.

Knowing that assembled silk hydrogel can be made transparent when thickness and Fmoc-L amount can be controlled, the effect of Fmoc-L amount on the hydrogel transparency was further studied using a UV-vis spectrophotometer (Figure 5.6). Firstly, 1 mL silk solution was mixed with different amounts of Fmoc-L. When comparing the Fmoc-L mass with silk fibroin, the weight ratio in the experiments can be converted to 40%, 80%, 120%, and 160%, corresponding to Fmoc-L mass of 20 mg, 30 mg, 40 mg, and 50 mg, respectively. Then hydrogel samples were formed in a small 30 mm polystyrene petri dish, and the petri dish with hydrogel adhered to the UV-vis spectrophotometer sample holder. Considering the polystyrene petri dish is transparent, the measured transmittance would be from the hydrogel. As expected, it is found that the transmittance would decrease when the Fmoc-L amount increases. More studies would be conducted to confirm the proposed reason that the reduced transmittance is due to excessive Fmoc-L precipitated from the hydrogel. For antimicrobial electrodes, the transparency can facilitate the visual observation of the skin condition while measuring the electrical signals. For this application, transparency higher than 70% would be high enough for the observation. The assembled Fmoc-L hydrogel with transparency of > 90% is sufficient for the application.

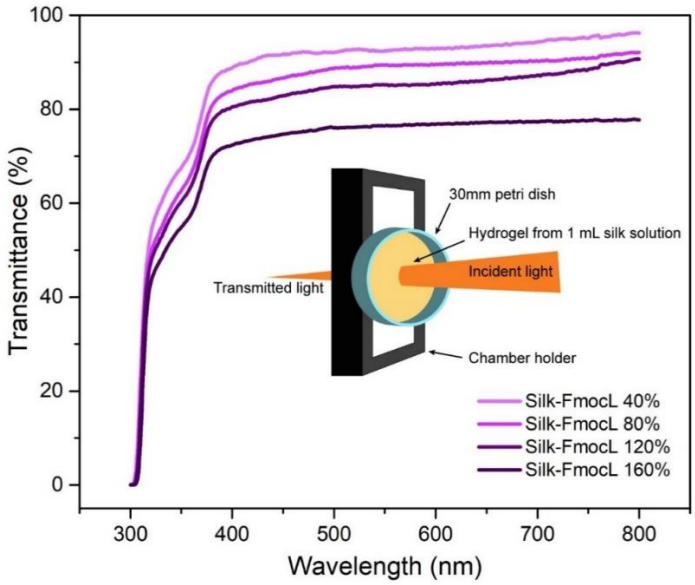

Figure 5.6 UV-vis spectrum of assembled hydrogel prepared inside a petri dish. As the weight ratio of Fmoc-Leu-OH over silk fibroin increases, its transparency decreases. The silk fibroin hydrogel was prepared from a 1 mL silk fibroin solution.

The microstructure of hydrogel can help reveal detailed information about the formation mechanism of the assembled silk hydrogel. SEM images of the prepared silk hydrogel were captured (Figure 5.7). First, 1 mL silk fibroin solution was added to a small 30 mm polystyrene petri dish, a different amount of Fmoc-L (as measured using weight ratio compared with silk fibroin weight) was added, pure silk solution sample is also prepared for comparison. All the samples (with gelation or without gelation) were frozen under -80 °C overnight to freeze the sample network, subsequently, the frozen samples are lyophilized for 48 hours to totally remove water but still maintain the morphological structure of the sample framework. Pure silk fibroin showed dense fibrous surface morphology. It is noted that pure silk could not form observable hydrogel no matter the heating temperature and duration in our experiment. This fibrous structure is probably due to the precipitation of Na_2CO_3 crystal due to the addition of Na_2CO_3 into the silk solution. For Silk-Fmoc-L-8%, the hydrogel is also not formed. As indicated by the SEM image, a flat surface was observed. For the sample of Silk-Fmoc-L 40%, hydrogel formed and showed the most transparent appearance. From the SEM image, the porous, sheet-like microstructure demonstrates the sustaining of a large amount of water in the hydrogel. The

porous and sheet-like structure is typical for lyophilized hydrogel. As the amount of Fmoc-L keeps increasing, the samples also form a hydrogel, but lyophilized samples are very fragile and crushed fragments are observed. In conclusion, Silk-Fmoc-L 40% showed the best morphology and mechanical property when assembled as a hydrogel. In later experiments of anti-bacterial study of silk hydrogel, Silk-Fmoc-L 40% was used.

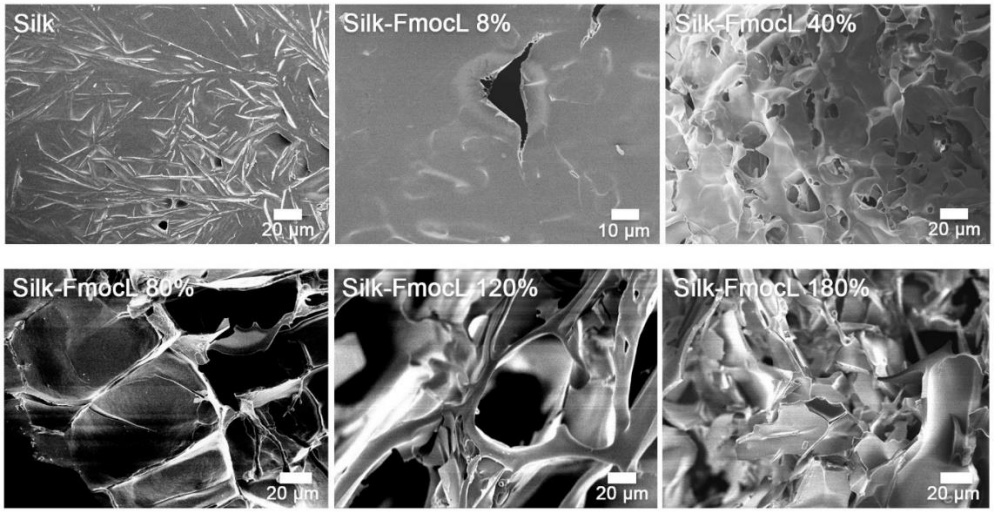

Figure 5.7 SEM images of silk fibroin hydrogel prepared from different Fmoc-Leu-OH weight ratios. The hydrogel samples were first lyophilized, and vacuum sputtered a gold layer for SEM imaging. Only Silk and Silk-Fmoc-L (8%) cannot form a hydrogel, Silk-Fmoc-L (40%) formed the most robust structure. Silk-Fmoc-L (80%), Silk-Fmoc-L (120%), Silk-Fmoc-L (180%) showed crushed hydrogel fragments.

To study the mechanism of silk hydrogel formation due to the presence of Fmoc-L. FTIR-ATR spectrum with different amounts of Fmoc-L was studied. It is reported that silk fibroin solution is a metastable solution with the random coil as the dominant secondary structure. As they are not thermodynamically the most stable, they intend to form hydrogels when treated with shearing force, pH adjustment, water exclusion, solvent treatment, or heat treatment. This is achieved by transforming random coil secondary structure to thermodynamically more stable β-sheets. Hydrophobic β-sheets work as physical crosslinks to main the gel shape and essentially stabilize the gel. At the stage of gel formation, the transmittance is reduced to the formation of a heterogeneous structure,

causing increased light scattering in the visible light range[13]. In a summary, β-sheets formation plays an essential role in the gelation process of silk fibroin as well as the mechanical property of the gel. The higher content of β-sheets, the higher degree of crystallinity.

A series of Silk-Fmoc-L samples with different Fmoc-L amounts are prepared by frozen and lyophilization process and the samples were crushed with mortar and pestle, pressed into pellets, the FTIR spectra of the samples are measured in FTIR-ATR mode. As shown in Figure 5.8, there is a trend of peak evolution with the increase of Fmoc-L amount. For silk fibroin protein, β-sheets and random coil secondary structures can be distinguished from amide I, amide II, and amid III vibrating bands[14]. The band of amide I is due to C=O stretching and C-N stretching. The vibrating band has a different peak position for different conformation: random coil has a peak position at around 1645 cm^{-1} and β-sheet has a peak position at around 1625 cm^{-1}. The band of amide II is mostly due to C=O in-plane bending, C-N stretching, and N-H in-plane bending. For amid II, the random coil has a peak position at around 1530 cm^{-1} and the β-sheet has a peak position at around 1512 cm^{-1}. Amide III band is mostly due to C-N stretching, for which random coil has a peak position at around 1230 cm^{-1} and β-sheet has a peak position at around 1270 cm^{-1}[15]. By comparing the peak intensity of these three-amide vibrating bands, the transformation of random coil and β-sheet can be deduced.

From Figure 5.8 of Amide I, for pure silk sample, the peak is at around 1645 cm^{-1}, corresponding to a secondary structure of random coil, which is in accordance with its state as a solution, without formation of a hydrogel. When silk fibroin is in the solution phase, the random coil is the most prominent secondary structure conformation it applies. As the Fmoc-L amount increased from 8% to 160%, the peak at 1645 cm^{-1} disappeared with an appearance of a new peak at around 1622 cm^{-1}, corresponding to the peak of β-sheet secondary structural conformation. For Amide II and Amide III peaks the same trend was also observed. These results indicate that Fmoc-L promoted the transformation of the random coil into β-sheet, thus the formation of silk fibroin hydrogel. The mechanism of

silk fibroin secondary structure transformation by Fmoc-L is probably due to the hydrophobic interaction to hydrogen bonding interaction between silk fibroin and Fmoc-L.

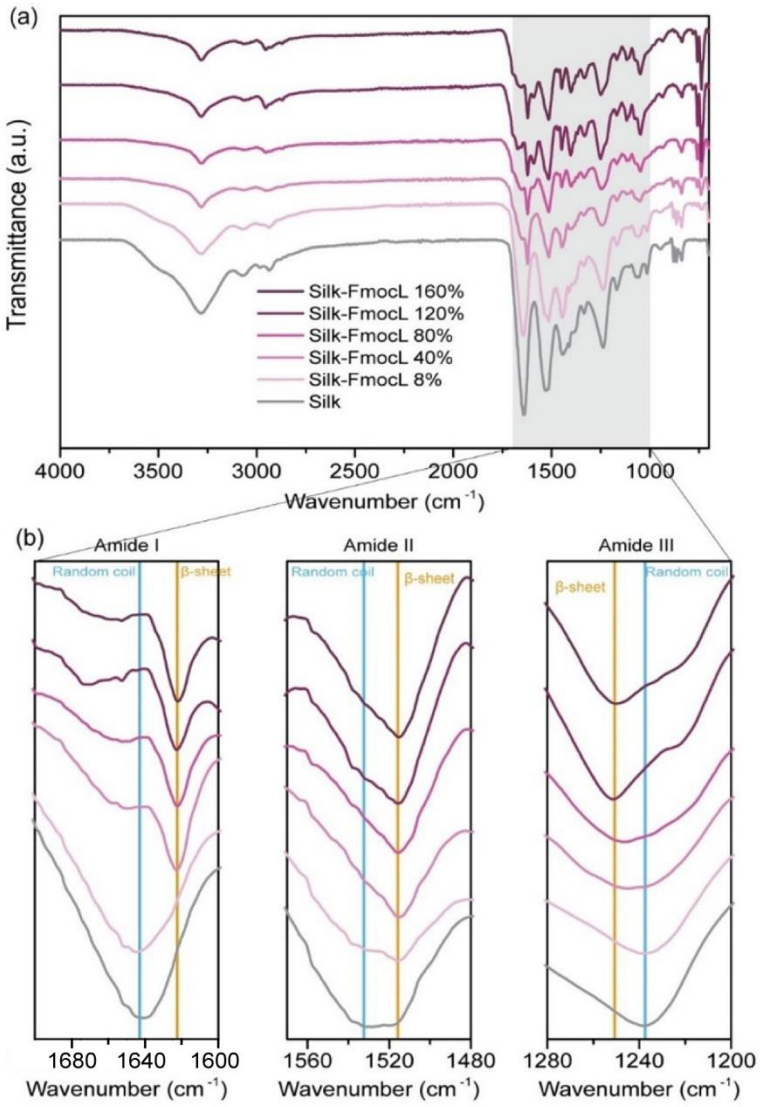

Figure 5.8 FTIR-ATR spectrum of Silk-Fmoc-L samples from different silk and Fmoc-L weight ratios. Specifically, three peak structures were analyzed in detail. These three peak structures include Amide I C=O stretching (1630 – 1650 cm^{-1}), Amide II secondary N-H bending (1540 – 1520 cm^{-1}), and Amide III C-N stretching (1270 – 1230 cm^{-1}). As the Fmoc-L weight ratio increases, the β-sheet conformation is also increased, and random coil conformation is decreased.

The antimicrobial property of Fmoc-L assembled silk fibroin hydrogel was estimated using Bacillus subtilis (B. subtilis). B. subtilis is a commonly seen gram-positive bacteria model. To prepare the anti-bacterial experiment. B. subtilis was incubated overnight in Luria-Bertani (LB) broth medium into an exponential phase. 100 μL of stock solution of bacteria in 0.85% NaCl was dipped on the surface of co-assembled silk fibroin hydrogel inside a petri dish (30 mm diameter). The hydrogel treatment was maintained for 1 hour. As a control experiment, another group of 100 μL bacteria stock solution was dropped in an empty petri dish and allowed to rest for the same time as the hydrogel treatment. After 1-hour treatment, 100 μL 0.85% NaCl solution was added to both petri dishes, the surface of hydrogel was washed, and the solution was taken from the hydrogel surface into a 1.5 mL vial tube. The treated bacteria solution was serially diluted by 105 times in LB solution. 100 μL of the diluted bacteria LB solution was dipped on the agar plate, spread thoroughly, and incubated in an oven at 34 °C for 12 hours. After the incubation, the plates were taken out and the CFU was counted.

From Figure 5.9 the control group of bacteria is densely spread on the agar plate, indicating very high viability, with a live bacteria concentration of around 8.13 x 108 CPU mL^{-1}. As a comparison, bacteria treated by assembled silk hydrogel showed an almost clean agar plate surface, indicating no bacteria are alive after the hydrogel treatment. This result demonstrates a surprisingly high bacterial kill efficiency of Fmoc-L assembled silk fibroin hydrogel.

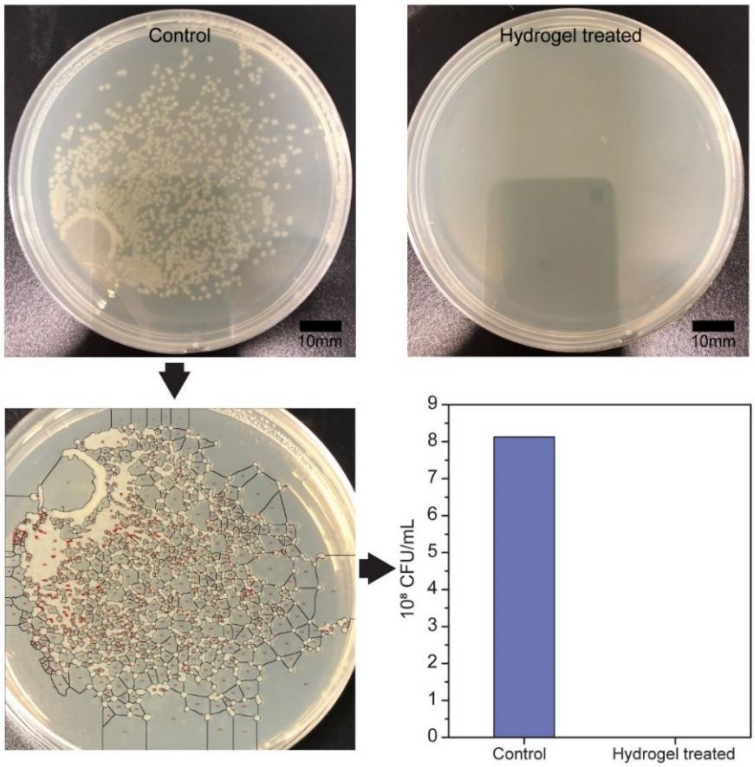

Figure 5.9 Agar plate spreading method to verify the bacteria-killing efficiency of Silk-Fmoc-L hydrogel. B. subtilis was used as a model bacterium in this experiment. Bacteria solutions were first treated with Silk-Fmoc-L hydrogel and then incubated on an agar plate; the colony-forming units (CFU) are counted. Compared with control bacteria which is incubated without hydrogel, the hydrogel treated bacteria agar plate showed a very clean surface, without any observable bacteria colonies, the control plate showed rather plenty of bacteria colonies, corresponding to a live bacterial concentration of 8.13×10^8 CFU mL^{-1}.

To further confirm the bacteria-killing effect of Fmoc-L assembled silk fibroin hydrogel, live/dead bacteria staining by SYTO 9 and propidium iodide was conducted. SYTO 9 enters live and dead bacteria membrane and has a green fluorescence, PI only enters the dead bacteria membrane and emits red-yellow fluorescence. By comparing the fluorescence intensity of green and yellow, the live and dead bacteria density can be distinguished. As shown in Figure 5.10, bacteria solution in the control group showed prominent green fluorescence, indicating a great number of live bacteria, while bacteria solution treated by Fmoc-L assembled silk fibroin hydrogel showed prominent yellow fluorescence, demonstrating that almost all the bacteria are killed by silk fibroin hydrogel.

This fluorescence result agrees well with the agar plat spreading experiment, further confirms the strong bacteria-killing effect of Fmoc-L assembled silk fibroin hydrogel.

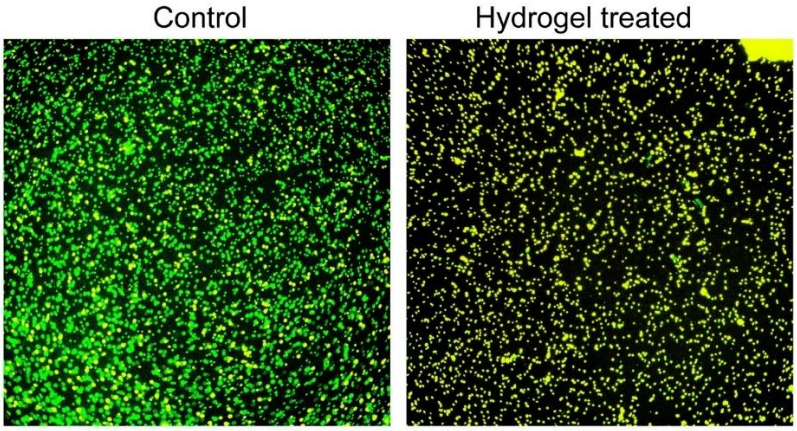

Figure 5.10 LIVE/DEAD bacteria staining of bacteria before and after hydrogel treatment. SYTO 9 staining has a green fluorescence while PI staining has a red-yellow fluorescence. SYTO 9 stains both live and dead bacteria and PI stains only dead bacteria. The bacteria after hydrogel treatment showed almost all dead fluorescence while control bacteria showed almost all live fluorescence, indicating that the hydrogel is very effective in killing bacteria.

In a conclusion, a family of Fmoc-protected amino acids is found to assemble silk fibroin into a hydrogel through a very facile water bath heating method. No organic or toxic additives are included in the fabrication process. The silk fibroin assembling mechanism due to the presence of Fmoc-protected amino acids is due to the hydrophobic fluorenyl group encourages the silk fibroin chain movement, transforming from random coil towards more thermodynamically stable β-sheet structure, β-sheet can work as physical crosslinks for the gel is formed. As reported earlier, Fmoc-Leu-OH, one of the Fmoc-protected amino acids, has intrinsic gram-positive antibacterial activity due to the presence of the leucine group in its structure. For this reason, we further studied the Fmoc-L assembly of silk fibroin. It was found that as the number of Fmoc-L increases, more β-sheet is transformed from random coil secondary structure. And Fmoc-L weight ratio of 40% compared with silk fibroin showed the best gel-forming property. B. subtilis, a common type of gram-positive bacteria, was studied for the antibacterial activity of as-assembled silk hydrogel.

Agar plate spreading experiment and live/dead fluorescence staining showed that a bacteria concentration of 8.13 CFU mL^{-1} was almost totally killed by the hydrogel, indicating excellent antibacterial property due to the co-assembled Fmoc-L.

A previous study demonstrated a silk fibroin hydrogel material due to a facile assembly process by Fmoc-protected amino acids. When Fmoc-L, one type of the Fmoc-protected amino acids were used, the impressive gram-positive antibacterial activity of the silk fibroin hydrogel is presented. However, despite the excellent antibacterial property of such silk fibroin hydrogel, it has relatively poor mechanical properties and can only be applied as an injectable hydrogel for skin bioelectrode application. The requirement for patchable antimicrobial hydrogel includes a mechanically robust structure so that a flexible freestanding film can form and accommodate possible deformation on the skin. Unfortunately, the silk fibroin hydrogel we proposed in the last project is not able to work in such a requirement.

PAAm hydrogel, a synthetic hydrogel from polymerization and crosslinking AAm into covalent 3D network structure, is reported to possess exceptional mechanical properties (Figure 5.11).

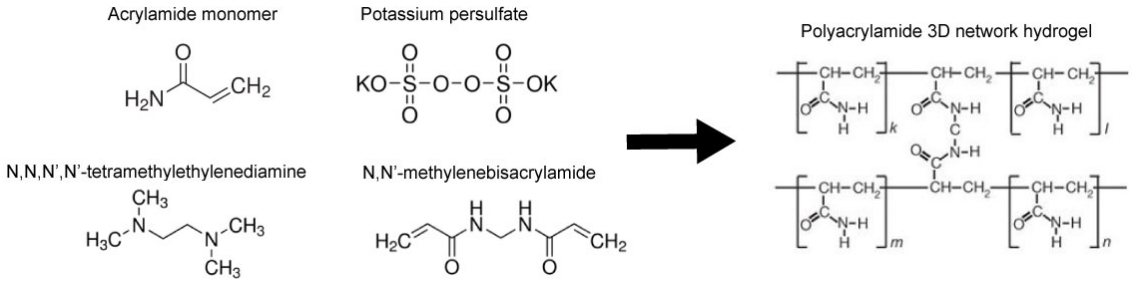

Figure 5.11 Chemical structure of the reagents and products during the hydrogel synthesis. Acrylamide was used as the monomer to undergo polymerization, potassium persulfate was added as thermal initiator, N,N,N',N'-tetremethylethylenediamine was added as crosslinker. The formed PAAm is a 3D network that can withstand more than 90% of water.

As PAAm hydrogel possesses excellent mechanical properties such as high toughness and stretchability, and silk fibroin hydrogel possesses excellent biocompatibility but with poor mechanical property, a hydrogel composed of double network with silk fibroin interpenetrated with PAAm is developed, the silk fibroin protein network would work as an energy dissipating media at the same time, thus hardening the PAAm hydrogel, PAAm hydrogel, on the other hand, would offer a robust backbone framework for silk fibroin to anchor on it through hydrogen bond due to the plenty of ester groups. In addition, it is reported that ethanol annealing would enhance the mechanical property of silk fibroin hydrogel by promoting β-sheet formation[16]. For this reason, the as-prepared Silk-PAAm hydrogel is treated with 87% ethanol for 6 hours, then followed by water annealing for another 24 hours to remove any unreacted chemical residues. AAm hydrogel as a control group underwent the same treatment procedures. It was observed that both Silk-PAAm hydrogel and PAAm hydrogel turned from transparent to opaque white appearance after the ethanol treatment with shrinkage of hydrogel volume (Figure 5.12). This is probably since ethanol dehydrated the hydrogel and packed the hydrogel backbone to a more ordered microstructure increasing light scattering so that the volume shrunk, and the color changed from transparent to opaque.

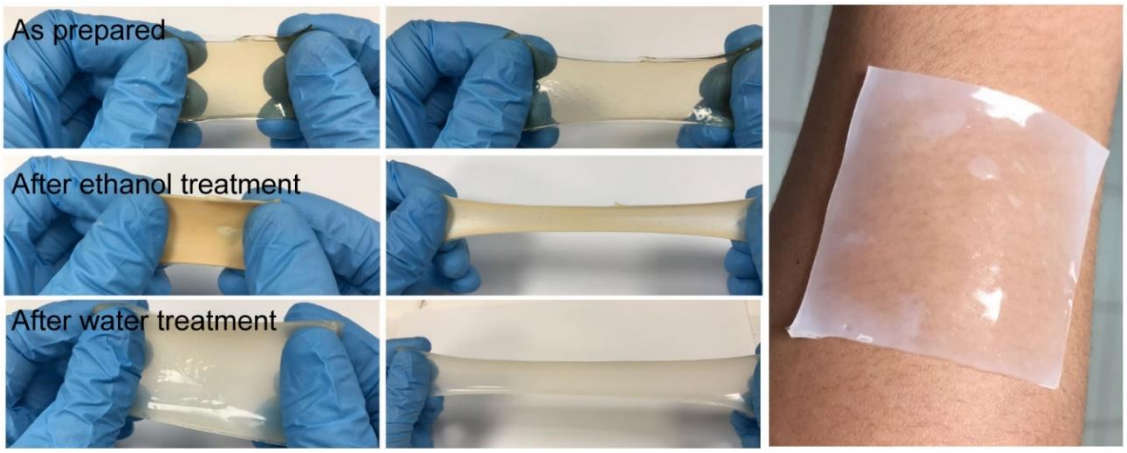

Figure 5.12 Photograph images of the obtained Silk-PAAm hydrogel. The weight ratio of silk to water is 5% while the weight ratio of AAm to water is 20%. The hydrogel showed good mechanical properties as reflected by stretching. It is also wearable on skin with moderate adhesiveness. After water treatment, the hydrogel has a semi-transparent appearance.

To verify the proper weight ratio of AAm over silk, the weight percentage of AAm as compared with water is tuned in both Silk-PAAm hydrogel and AAm hydrogel. In the experiment, 0.4 g, 0.6 g, 0.8 g AAm are added into 3 mL of silk fibroin solution (5 wt%), respectively. Converting the weight ratio of AAm monomer and water, they are denoted as Silk-AAm 13%, Silk-AAm 20%, Silk-AAm 27%. AAm hydrogel in the control experiment also follows the same weight ratio of AAm monomer, denoted as AAm 13%, AAm 20%, and AAm 27%. Interestingly, for samples of Silk-AAm 20% and Silk-AAm 27%, after the hydrogel was stretched, there was a surface crack layer formed, indicating there is a layer separation (Figure5.13). It is noted that silk fibroin hydrogel is harder compared with the soft PAAm hydrogel. The cracked surface should come from a thin layer of silk fibroin. For comparison, Silk-AAm 13% did not show such a cracked surface layer, as shown in Figure 5.13. In the sample of Silk-AAm 20% and Silk-AAm 27%, the content of AAm monomer is higher than the sample of Silk-AAm 13%. More AAm monomers would form a denser 3D network compared with hydrogel formed from fewer AAm monomers. If the 3D PAAm network is dense, then it is more difficult for silk fibroin to wrap through the PAAm meshes, thus the penetrating density of silk fibroin into the PAAm 3D network is restricted, some silk fibroin would be expelled from inside PAAm hydrogel to the surface of the hydrogel. For hydrogel sample Silk-AAm 13% with less AAm monomers, the formed PAAm 3D network is looser, allowing more silk to wrap around. The Silk-AAm 13% showed a uniform interpenetrating network between PAAm polymer and silk fibroin polypeptides.

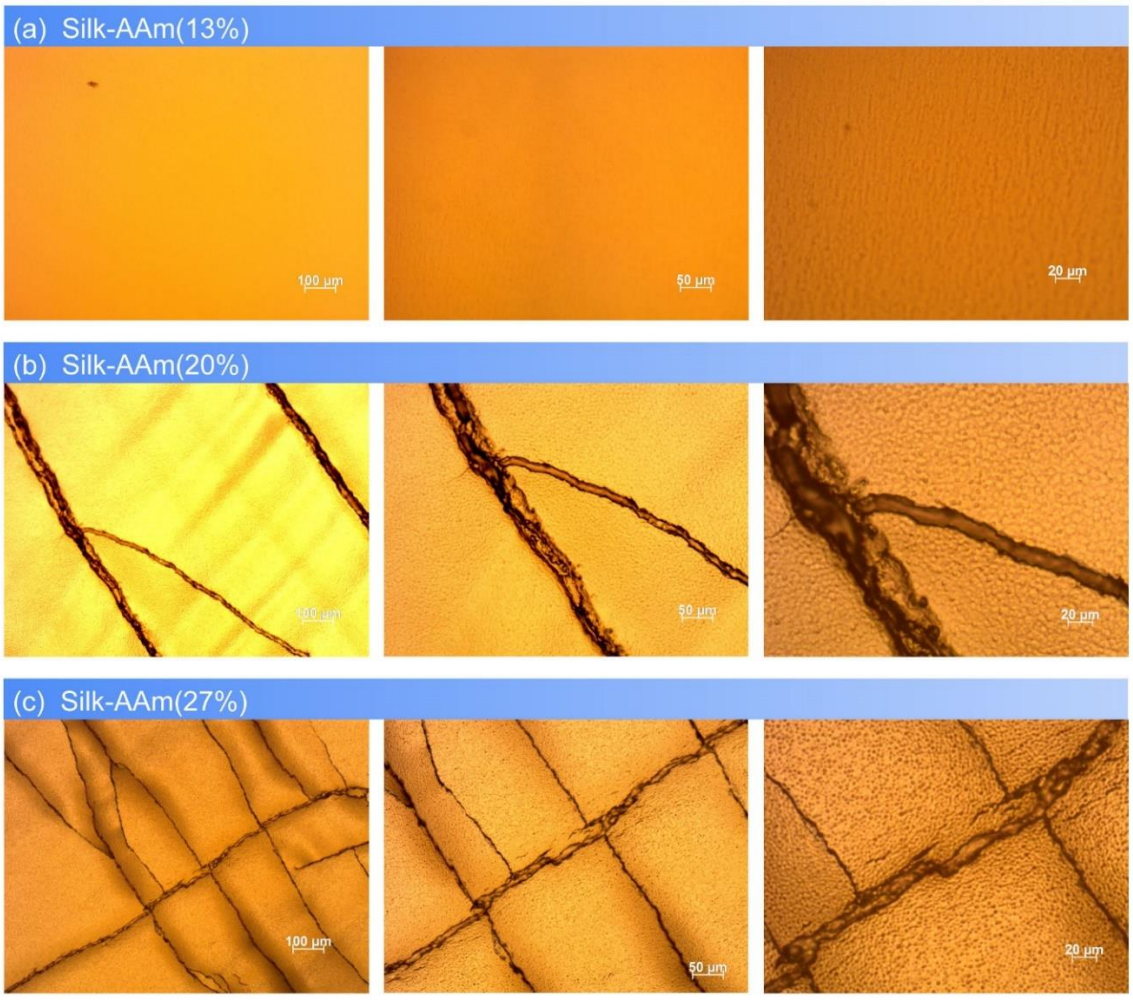

Figure 5.13 Light microscope images Silk-AAm hydrogel with different AAm weight ratios at 5X, 10X, and 20X. Other preparation parameters of the hydrogels were kept the same. Very interestingly, a hydrogel with 13% AAm monomer showed a smooth surface feature without any crack formation, indicating the formation infiltration of polyacrylamide network and silk fibroin network. However, Silk-AAm hydrogel with 20% AAm monomer and 27% monomer showed dense surface crack, which is formed due to a separated rigid silk layer on the top of the hydrogel.

As a control experiment, the pure PAAm hydrogel is also prepared (Figure 5.14). As expected, with the absence of silk fibroin, the PAAm hydrogel showed a uniform surface feature without any crack formation, further confirming that the brittle surface crack structure is from the aggregation of silk fibroin.

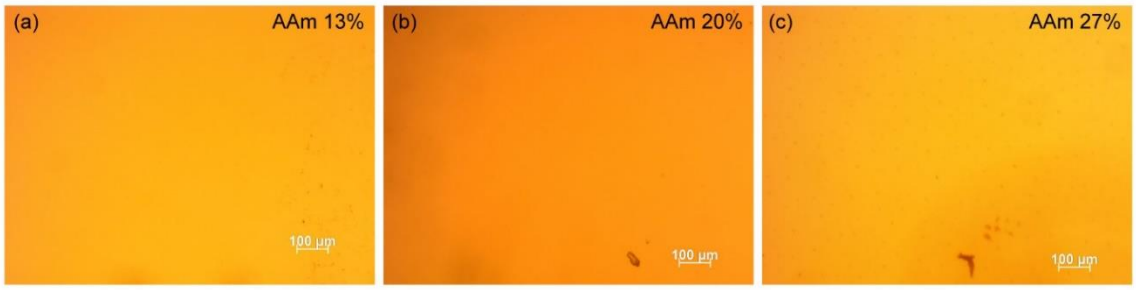

Figure 5.14 Light microscope images of control hydrogel made of pure AAm. With the variation of AAm weight ratio, there is no surface crack formation, this indicates that the crack formed in Silk-AAm is due to the presence of silk fibroin.

It is more interesting to investigate the mechanical property of Silk-AAm hydrogel and AAm hydrogel to understand the change of the PAAm 3D network system due to the addition of silk fibroin (Figure 5.15). To prepare the sample for the measurement, PDMS mold is first fabricated to make a 10 mm x 30 mm x 5 mm hollow structure, the PDMS mold is further pressed onto a glass surface. 400 µL Silk-AAm hydrogel precursor or AAm hydrogel precursor were poured into the mold and covered by a polystyrene petri dish lid, the mold was heated at 60 °C in an oven for 12 min. The formed hydrogel is harvested and measured in an MTS tester. From the mechanical stress-strain test of PAAm hydrogels, it is observed that as the weight ratio of AAm increases, its break elongation and Young's modulus also increase, this confirms that more AAm monomers would form a denser 3D network structure, thus its strength is increased. The trend of increasing AAm monomer content follows a similar rule as that of AAm-hydrogel, but their break elongation strains kept almost the same. When analyzing the effect of incorporation silk fibroin, Young's modulus of Silk-AAm 27% hydrogel is increased to 206.9 kPa compared with 39.6 kPa in AAm-27% hydrogel, Young's modulus of Silk-AAm 20% is increased to 100.4 kPa compared with 15.0 kPa in AAm-20%, Young's modulus of Silk-AAm 13% is 7.0 kPa compared with 6.8 kPa in AAm 13% hydrogel. The hardening effect of silk fibroin on the PAAm hydrogel is most prominent when the AAm monomer weight percentage is high, while is negligible when the AAm monomer is 13%. Indeed, when applying the hydrogel material for skin electrodes, the material is usually preferred to be soft to allow more conformable attachment on the skin. Harder materials would possibly leave some area of

the wound uncontacted with the dressing and vulnerable to bacterial infection. In this case, the hardening effect of silk fibroin on PAAm hydrogel is unfavored and should be avoided. For this reason, a hydrogel with the formulation of Silk-AAm 13% would be superior for applying as wound dressing material, instead of the hardened Silk-AAm 27% and Silk-AAm 20%.

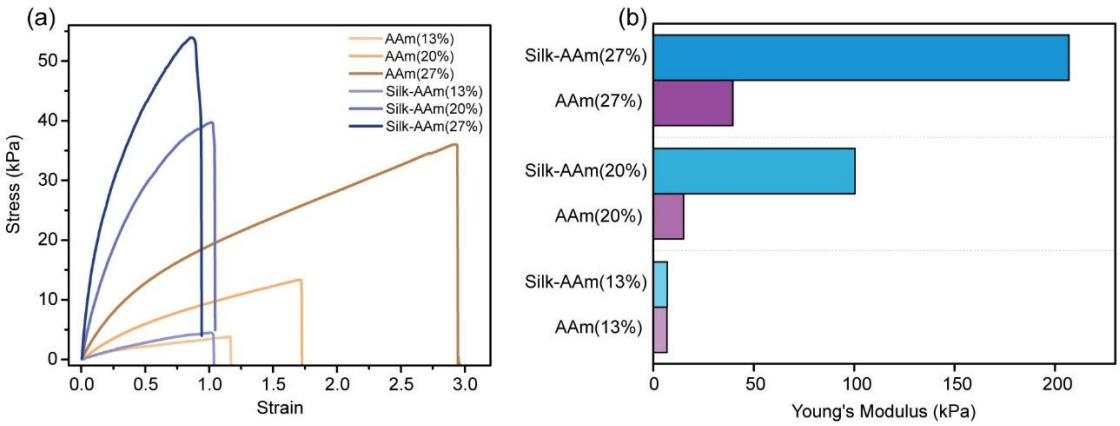

Figure 5.15 Mechanical stress-strain cure (a) and Young's modulus (b) of hydrogels made from different AAm weight ratios. The break elongation Silk-AAm is smaller compared to that without silk, while Young's modulus of Silk-AAm hydrogel is larger than that without silk. This indicates that there is an obvious hardening effect of the hydrogel by the silk.

To prepare the Silk-AAm 13% hydrogel with antimicrobial property, Silk-AAm 13% hydrogel was first fabricated as described above. Fmoc-L solution was prepared by adding 100 mg of Fmoc-L to 30 mL 0.1 M Na_2CO_3 solution. The Silk-AAm 13% hydrogel was dipped into the Fmoc-L solution for 24 hours to absorb Fmoc-L molecules. The finally obtained Silk-AAm-Fmoc-L hydrogel showed a whiter color compared with before Fmoc-L absorption.

To study the chemical structure of Silk-PAAm-Fmoc-L, the FTIR-ATR spectrum of the lyophilized films was studied (Figure 5.16). To prepare the sample for FTIR, the hydrogel was first treated with 87% ethanol for six hours and subsequently treated with DI water for another 24 hours, then the hydrogel was dipped into Fmoc-L solution for 24 hours to allow thorough absorption of Fmoc-L, followed by total drying out in the oven. From the FTIR

spectrum of Silk-AAm-Fmoc-L film, it was observed that vibrating bands for amide I, amide II, and amide III showed peak shifts towards the β-sheet formation, while Silk-AAm still showed quite plenty of random coil structure. As indicated from our first project, Fmoc-L would encourage hydrophobic interaction and chain movement, which is in favor of β-sheet formation.

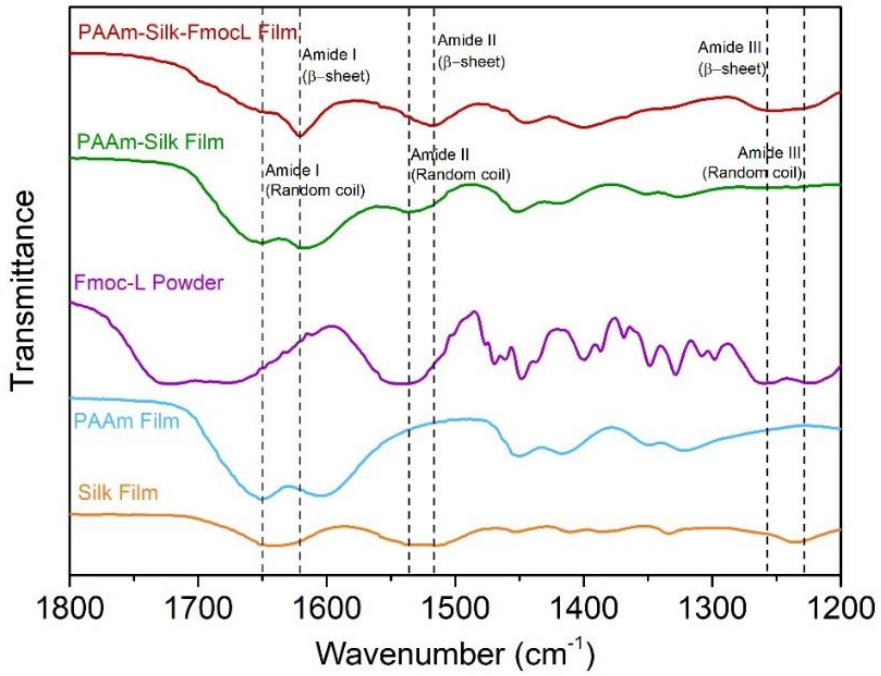

Figure 5.16 FTIR-ATR spectrum of Silk-AAm with different comparing samples. There is an obvious presence of β-sheet conformation in the Silk-AAm hydrogel, indicating that a physical crosslink of a β-sheet of silk fibroin was formed in the Silk-AAm hydrogel.

It was reported that Fmoc has fluorescence at around 335 nm due to the presence of the fluorescent fluorenyl group[17]. As a result, by measuring the fluorescence of the material, the existence of Fmoc-L can be deduced. The fluorescence of Silk-AAm-Fmoc-L hydrogel was conducted with Fmoc-L Na_2CO_3 solution scanned as a control group (Figure 5.17). It can be shown that for the control Fmoc-L Na_2CO_3 solution there is a peak of 341 nm followed by a peak at 375 nm. The 341 nm peak should come from the fluorenyl group in Fmoc-L and the 375 nm peak is probably due to the excimer emission. For the hydrogel sample of Silk-PAAm-Fmoc-L, there is a prominent peak at 321 nm, corresponding to the

fluorescence emission of the fluorenyl group. The shift of this peak from 341 nm to 321 nm is probably due to the change of reflective index of water and air. For the Fmoc-L Na_2CO_3 solution it was measured in water and for the hydrogel of Silk-PAAm-Fmoc-L it was measured in air, both are filled in a quartz cuvette. The difference in the solid or liquid sample may be the reason for such a shift.

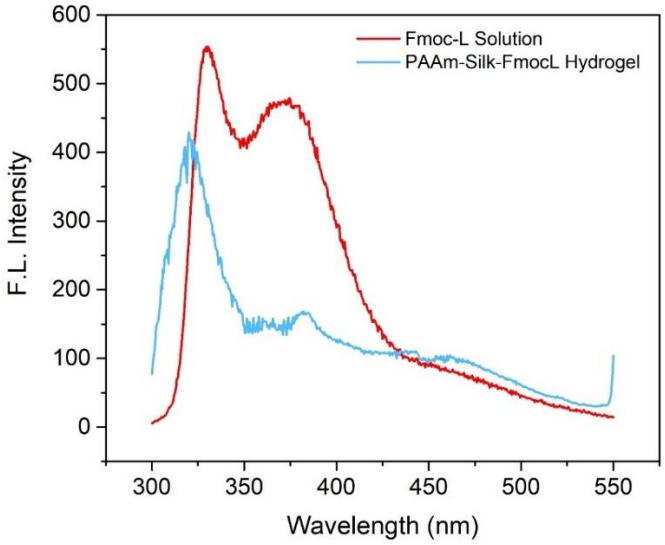

Figure 5.17 Fluorescence spectrum of Silk-AAm hydrogel when loaded with Fmoc-L. The emission peak of 328 nm is due to the fluorenyl group in Fmoc-L, while the peak at 371 nm is due to the excimer emission. This indicates that the Fmoc-L was integrated with Silk-AAm hydrogel.

Lastly, the microstructure of Silk-PAAm hydrogel and Silk-PAAm-Fmoc-L hydrogel was investigated in SEM (Figure 5.18). To prepare the sample for SEM, the hydrogels were stored at -80 °C for 24 hours and subsequently lyophilized for 48 hours to fully remove any water moieties. From the SEM image of Silk-PAAm hydrogel, there is a fine porous structure due to the evaporation of water. The 3D framework is also well maintained without any observable phase separation, indicating that silk fibroin is uniformed interpenetrated into the PAAm polymeric structure. For the Silk-PAAm-Fmoc-L hydrogel, very interestingly, there is a fine layer of nanorods grown on the wall of hydrogel with a length of around 5 μm and diameter of around 100 nm. Since this nanorod phenomenon is not observed in Silk-AAm hydrogel, these nanorods are probably formed from the precipitation of Fmoc-L during the freezing and lyophilizing process. To justify this

hypothesis, more hydrogel samples need to be observed. The hydrogel needs to be dried in the oven rather than freeze-dry to check the differences.

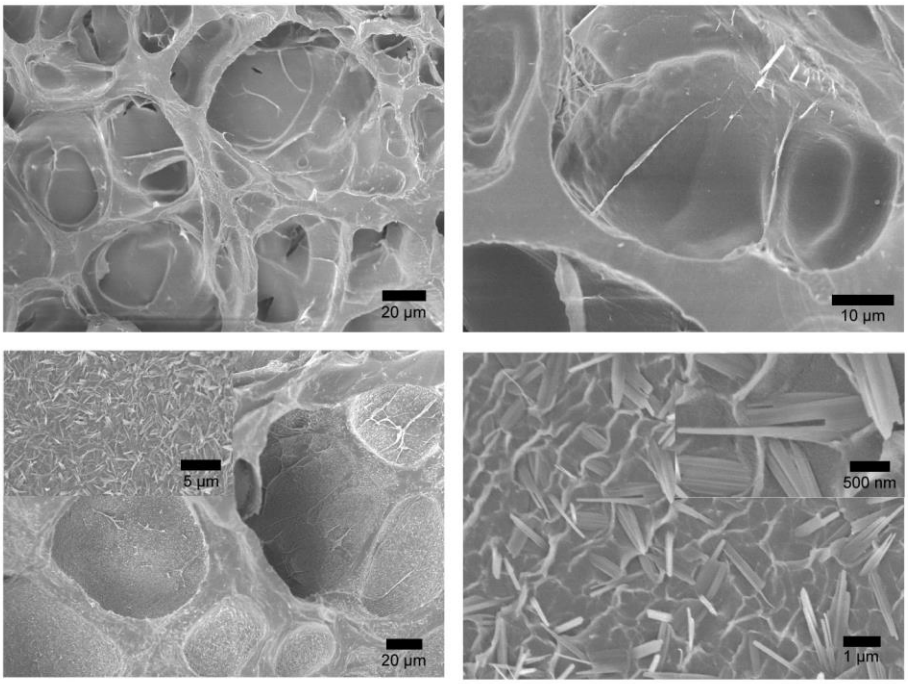

Figure 5.18 SEM images of Silk-AAm (top) and Silk-AAm-Fmoc-L (bottom). In Silk-AAm there showed a typical porous structure of hydrogel. Interestingly, in Silk-AAm-Fmoc-L there showed a layer of nanorods grown on the surface of the hydrogel structure. These nanorods are probably due to the precipitation of Fmoc-L. The formation mechanism requires further study to justify.

In conclusion, silk fibroin hydrogel with promising biocompatibility and antimicrobial activity thus is an ideal hydrogel material for skin bioelectrode applications. However, silk fibroin hydrogel assembled from β-sheet formation has very poor mechanical properties. In addition, silk fibroin has no intrinsic ability to resist bacterial infection, thus increasing the risk of bacterial colonization on the skin. To tackle these problems, silk fibroin was incorporated with PAAm hydrogel to form a robust and elastic hydrogel. PAAm provides a tough 3D polymeric network for silk fibroin to interpenetrate through. It was found that when AAm monomer content is high, a denser 3D polymeric network would form. The denser PAAm network has two effects: The first effect is to restrict the silk fibroin hydrogel

interpenetration and expel some of the silk fibroin into the surface layer, forming a brittle layer that will crack when the hydrogel is stretched. The second effect is to increase the break elongation and Young's modulus of the hydrogel. Another finding from the mechanical test is that the addition of silk to the PAAm hydrogel would harden the material if the PAAm 3D network is dense. To avoid the phase separation of silk fibroin and PAAm network as well as the hardening of hydrogel, Silk-AAm 13% was used to make homogenous and soft hydrogel. Further antimicrobial functionalization would be investigated to apply the hydrogel for skin bioelectrode application.

Reference

[1] J. M. Torpy, A. Burke, R. M. Glass, JAMA 2005, 294, 2122; S. Towfigh, T. Clarke, W. Yacoub, et al., Archives of Surgery 2011, 146, 448.

[2] S. Guo, L. A. DiPietro, Journal of Dental Research 2010, 89, 219.

[3] M. Farokhi, F. Mottaghitalab, Y. Fatahi, A. Khademhosseini, D. L. Kaplan, Trends in Biotechnology 2018, 36, 907.

[4] G. M. Nogueira, M. A. de Moraes, A. C. D. Rodas, O. Z. Higa, M. M. Beppu, Materials Science and Engineering: C 2011, 31, 997.

[5] G. Chen, N. Matsuhisa, Z. Liu, D. Qi, P. Cai, Y. Jiang, C. Wan, Y. Cui, W. R. Leow, Z. Liu, S. Gong, K.-Q. Zhang, Y. Cheng, X. Chen, Advanced Materials 2018, 30, 1800129.

[6] D. N. Rockwood, R. C. Preda, T. Yücel, X. Wang, M. L. Lovett, D. L. Kaplan, Nature Protocols 2011, 6, 1612.

[7] M. Floren, C. Migliaresi, A. Motta, J Funct Biomater 2016, 7.

[8] M. Farokhi, F. Mottaghitalab, Y. Fatahi, A. Khademhosseini, D. L. Kaplan, Trends Biotechnol 2018, 36, 907.

[9] M. Ribeiro, M. P. Ferraz, F. J. Monteiro, M. H. Fernandes, M. M. Beppu, D. Mantione, H. Sardon, Nanomedicine 2017, 13, 231; Z. Karahaliloğlu, Materials Technology 2018, 33, 276.

[10] I. Irwansyah, Y. Q. Li, W. Shi, D. Qi, W. R. Leow, M. B. Tang, S. Li, X. Chen, Adv Mater 2015, 27, 648.

[11] C. A. Dinarello, Cell 2010, 140, 935; A. Ahmad, S. Azmi, J. K. Ghosh, Amino Acids 2011, 40, 749.

[12] P. H. Chan, Y. C. Chen, Anal Chem 2012, 84, 8952; H. K. Kang, D. E. Kang, B. H. Boo, S. J. Yoo, J. K. Lee, E. C. Lim, The Journal of Physical Chemistry A 2005, 109, 6799.

[13] A. Matsumoto, J. Chen, A. L. Collette, U.-J. Kim, G. H. Altman, P. Cebe, D. L. Kaplan, The Journal of Physical Chemistry B 2006, 110, 21630.

[14] F. Paquet-Mercier, T. Lefèvre, M. Auger, M. Pézolet, Soft Matter 2013, 9, 208.

[15] R. Urie, C. Guo, D. Ghosh, M. Thelakkaden, V. Wong, J. K. Lee, J. Kilbourne, J. Yarger, K. Rege, Advanced Functional Materials 2018; S.-W. Ha, A. E. Tonelli, S. M. Hudson, Biomacromolecules 2005, 6, 1722.

[16] D. Su, M. Yao, J. Liu, Y. Zhong, X. Chen, Z. Shao, ACS Appl Mater Interfaces 2017, 9, 17489; K. Numata, N. Ifuku, H. Masunaga, T. Hikima, T. Sakai, Biomacromolecules 2017, 18, 1937.

[17] A. M. Smith, R. J. Williams, C. Tang, P. Coppo, R. F. Collins, M. L. Turner, A. Saiani, R. V. Ulijn, Advanced Materials 2008, 20, 37; V. Jayawarna, M. Ali, T. A. Jowitt, A. F. Miller, A. Saiani, J. E. Gough, R. V. Ulijn, Advanced Materials 2006, 18, 611.

Chapter 6

Conformable skin electrodes for biopotential measurement

This chapter details the applications of skin bioelectrodes in the measurement of biopotential signals from human skin. Two types of biopotential signals (ECG and EMG) are measured. A novel PSA-coated technique to endure all the conductive film adhesive to the skin is presented. This technique allows all non-adhesive electrode surfaces, irrespective of their conductive materials or substrate materials adhesive to the skin. This can greatly solve the conformal issue related to most of the skin bioelectrodes. For the ECG measurement, 12-lead ECG characteristic results are obtained from a 3-electrode method. This method would greatly simplify the ECG measurement to reproduce 12-lead results. Furthermore, a miniaturized wireless flexible PCB is designed and fabricated to measure 3-electrode ECG and EMG signals. This flexible PCB, along with the conformal electrodes developed, would contribute to a wearable system for skin-based biopotential signal measurement.

6.1 Introduction

To measure the biopotential signals from the skin, conformal electrodes are needed. However, commonly used stretchable conductor-substrate electrode materials are not adhesive to the skin surface, making the attachment of the thin film electrodes on the skin surface difficult[1-3]. Stretchable electrodes are usually made from stretchable conductors on the stretchable substrate[4]. The stretchable conductors include thermo-evaporated Au nanofilm[3], AgNW[5], CNT[6], PEDOT: PSS conductive polymer film[7], and chemically synthesized Au nanomesh transparent conductor[8], etc. The stretchable substrates include PDMS, SEBS, ecoflex, etc. Unfortunately, all the above-mentioned materials (conductors and substrates) are not adhesive to the skin. The skin has a complex surface microstructure that is difficult to adhere to, in addition, the oily substance on the skin makes the skin hydrophobic, further increasing the challenges for adhesion[9]. Lastly, hairs extrude from the skin surface, obstructing the skin-thin film contact. For these reasons, the dry thin film electrode is difficult to directly attach to the skin for biopotential signal measurement. Hydrogel materials we previously developed can resolve the issue of adhering to the skin, but they easily dehydrate, losing water to the environment, limiting their application time. For long-term skin application, alternatives to hydrogel materials as an adhesive is needed. Another commonly used method is to use medical tape as a backing layer to fix the non-adhesive electrodes on the skin[10]. Such a method would limit the stretchability of the electrodes due to the restrain of the non-stretchable medical tape.

Here, we present a universal and facile method to fabricate conductive and adhesive conformal electrodes. The technique uses PSA to coat the surface of the electrode. PSA is not conductive on its own[2, 11]. However, The PSA naturally forms on sparse areas of the electrode. The areas covered by PSA serve as the adhesive anchoring points to bond the skin and the electrode. The areas uncovered by PSA keeps conductive and serve as signal transduction path to measure the signal from the skin. This technique has some advantages over hydrogel functionalization methods. Firstly, this technique is not dependent on specific materials. That is, any conductor materials (thermo-evaporated Au nanofilm, AgNW, CNT, conductive polymer, or chemically synthesized Au nanomesh, etc.) or

substrate materials (PDMS, SEBS, ecoflex, etc.) can be used. Secondly, the technique is facile to use. The only requirement to apply the coating is to plasma-treat the surface to be coated, which is compatible with most of the materials. The purpose of surface plasma treatment is to increase the hydrophilicity because the PSA coating depends on drop-casting an aqueous solution.

6.2 Experimental method

6.2.1 Preparation of Au nanofilm on PDMS

The Au nanofilm on the PDMS electrode was prepared by thermo-evaporation of Au on the PDMS substrate. A PDMS substrate film was prepared by mixing SYLGARD 184 silicone elastomer base and a curing agent at a ratio of 10:1, spin-coated on a silicon wafer at 800 r.p.m. for 60 s and cured at 80 °C for 5 h. After curing, the PDMS film on the Silicon wafer is put inside a thermal evaporator (Kurt J. Lesker Nano 36) for Au evaporation. A layer of 5 nm Cr was firstly evaporated on PDMS at an evaporating rate of 0.2 nm s^{-1}. Then a layer of 80 nm Au was subsequently evaporated on the Cr layer at an evaporating rate of 0.5 nm s^{-1}. The holder for the PDMS-Silicon wafer is rotated during evaporation to ensure uniform evaporation. After the thermal evaporation, the Au nanofilm on PDMS is peeled off from the silicon wafer for further use.

6.2.2 Preparation of Au nanofilm on SEBS

The Au nanofilm on SEBS (styrene-ethylene-butylene-styrene) electrode was prepared by thermal evaporation of Au on the SEBS substrate. A SEBS substrate film was prepared by dissolving SEBS polymer in toluene. Then the SEBS in toluene solution is cast in a glass petri dish and placed in a fume hood for 4 days. Toluene solution would be fully evaporated during this time, leaving a SEBS film formed in the glass petri dish. The SEBS film is peeled off from the glass petri dish and put into a thermal evaporator (Kurt J. Lesker Nano 36) for Au evaporation. A layer of 80 nm Au was subsequently evaporated on the Cr layer at an evaporating rate of 0.5 nm s^{-1}. The holder for Au-SEBS is rotated during evaporation

to ensure uniform evaporation. After the thermal evaporation, the Au nanofilm on SEBS is peeled off from the silicon wafer for further use.

6.2.3 Preparation of AgNW on PDMS

The AgNW conductor was firstly prepared on a glass substrate. Briefly, a glass substrate was treated with surface plasma. AgNW in isopropyl alcohol (Sigma-Aldrich) was spin-coated on the glass substrate and baked at 70 ºC for 10 min to fully evaporate isopropyl alcohol. The baking temperature was further increased to 200 ºC to anneal the junctions of contacting AgNWs to improve their electrical conductivity. A PDMS precursor was prepared by mixing an SYLGARD 184 silicone elastomer base and a curing agent at a ratio of 10:1. The precursor liquid is poured on the AgNW-glass substrate and spin-coated at 600 r.p.m. The PDMS-AgNW-glass is cured in an oven at 80 ºC for 6 h. After curing, the PDMS-AgNW is peeled off from the glass. AgNW is partially embedded in the PDMS, forming a very strong bonding between the conductor and the substrate. The AgNW-PDMS electrode can be used as skin electrodes.

6.2.4 EIS impedance measurement of electrodes on the skin

Different skin bioelectrode samples (Au-PDMS, Au-SEBS, and AgNW-PDMS) are cut into rectangular shapes of 2 x 1 cm^2. One end of the electrode film is bonded to copper wire and the other half (1 x 1 cm^2) is used as an electrode area to contact the skin. The electrode surfaces were coated with PSA to provide adhesiveness to the skin. For each electrode type, two electrodes adhere to the skin with a separation of 2 cm. The two electrodes connect with the two terminals in the EIS system. The Bode plot was obtained from the skin bioelectrode system.

6.2.5 Adhesive strength measurement on skin

The Au-SEBS skin bioelectrode samples were cut into rectangular shapes of 3 x 0.5 cm^2. The electrode surface was coated with PSA. Different PSA amount is used to realize

different electrode adhesiveness. Half of the skin bioelectrode is attached to human skin; the other end of the electrode is clipped by the clipper of the mechanical tester. The electrode was peeled off from the skin at a constant strain rate of 0.5 mm s^{-1}. The force used for the peeling is recorded. Adhesive strength is obtained by dividing the peeling force by the length of the electrode.

6.2.6 Measurement of ECG and EMG

The ECG signal was measured using an AD8232 single lead ECG module purchased from Sparkfun. Three electrodes are used for each ECG measurement. One electrode serves as the positive terminal, one electrode serves as the negative terminal, and the third electrode serves as an RLD. This RLD electrode supplies a common-mode voltage detected at the two measuring electrodes to the human body. Such a design would reduce the common-mode noises and DC offset, providing more clear signals. The analog output of the ECG module connects with a Data Acquisition System (Smacq USB 2610) to convert the amplified analog signal from the ECG module to a digital signal to be recorded on the computer. The signals are further filtered in software using a (0.5 – 40 Hz) bandpass IIR (infinite impulse response) filter. The EMG signal was measured using a Backyard Brains Heart and Brain SpikerBox.

6.3 On-skin characterization of skin electrodes

The non-adhesive skin electrodes, when coated with PSA, show promising conformal adhesiveness towards the skin. The PSA coating can be controlled to be very thin, without affecting the thickness of the skin electrodes. The thickness of skin electrodes is dominated by the elastomer substrate layer, it can be controlled by changing the spin-coating speed of the elastomer. As such, the skin bioelectrode can be made very thin (less than 100 μm), realizing the high conformability of the electrodes. As a comparison, the Au-PDMS electrodes without PSA coating cannot adhere to the forearm skin with hairs presenting (Figure 6.1 left). In the contrast, the PSA-coated Au-PDMS electrode shows intact conformability, even with skin wrinkles appearing on the electrode surface (Figure 6.1

middle). Attaching the PSA-coated electrode on the fingertip reveals a fingerprint pattern on the electrode, indicating the electrode is highly conformal thanks to the adhesive coating (Figure 6.1 right).

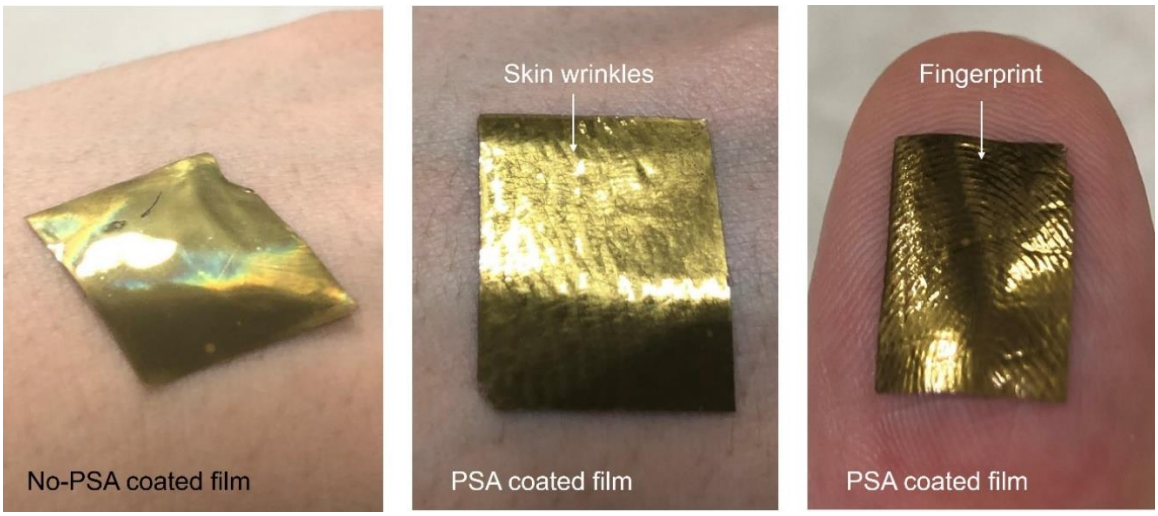

Figure 6.1 Photograph of PSA coated Au nanofilm on PDMS attached on human skin. No-PSA-coated Au nanofilm shows difficulties in covering hairy skin, while PSA-coated film can conformably cover hair skin. Skin wrinkles and fingerprints can form on the Au nanofilm.

The PSA coated electrode is a dry electrode, there is no hydrogel electrolyte layer beneath the electronic conduction layer in contact with the skin. Due to the lack of electrolytes, the electrodes require sweat underneath the electrode to serve as electrolytes for signal transduction. After the attachment of the electrode layer on the skin, the skin will sweat, which can moisturize the electrode surface and form an ionic conduction pathway between the electrode and the tissues underneath the stratum corneum. The skin-electrode conductivity is characterized by an impedance. Au-SEBS electrode is selected as a typical electrode to measure the skin-electrode impedance. The skin electrode is cut into a rectangular shape with a dimension of 2 x 1 cm^2. One end of the electrode connects with copper wire and the other half part of the electrode is coated with PSA for skin contact. Two such electrodes adhere to the skin with a separation of 2 cm. The two electrodes connect with two terminals in the EIS system. The skin impedance is measured from 1 Hz to 10^6 Hz. The Au-SEBS electrode without PSA coating is fixed on the skin with medical

tape, which is a common procedure in fixing non-adhesive electrodes on the skin. Commercial Ag/AgCl-gel electrode is also measured as a comparison. From the EIS Bode plot, the commercial Ag/AgCl-gel electrode records the lowest impedance for all the frequencies (Figure 6.2a), this is due to the presence of the electrolyte gel layer, which can greatly increase the ionic connection with the skin, benefiting for signal transduction. On the other hand, the Au-SEBS electrode with PSA coating or with medical fixation shows a slightly higher impedance than the commercial Ag/AgCl-gel electrode. The PSA-coated Au-SEBS electrode is further slightly higher than the medical tape fixation one. This is due to some areas of the PSA coating being blocked by the non-conductive PSA layer. These blocked areas reduce the effective contacting area with the skin, thus slightly increasing the impedance. However, the PSA-blocked areas serve an important role in bonding the skin and the electrode, improving the conformability of the electrodes. Though some area is sacrificed giving rise to slightly higher impedance, it is worth improving the skin adhesiveness, thus getting rid of the application of medical tapes. The phase angle comparison between commercial electrodes, tape-fixed Au-SEBS electrodes, and PSA-coated Au-SEBS electrodes also shows a similar result as the impedance plot (Figure 6.2b).

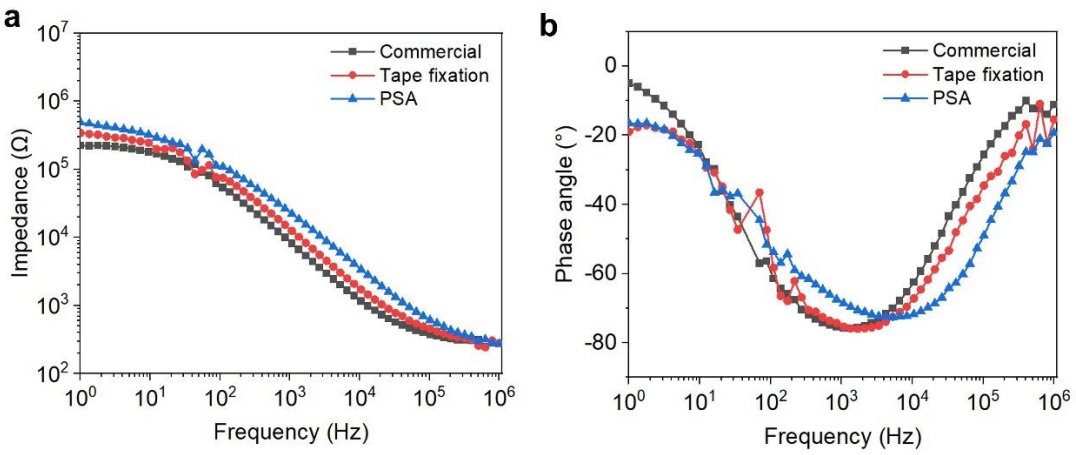

Figure 6.2 Impedance measurement of Au nanofilm-SEBS electrodes on the skin. (a) The Bode plot of the commercial Ag/AgCl-gel electrodes, tape-fixed Au nanofilm-SEBS electrodes, and PSA coated Au nanofilm-SEBS electrodes. (b) The phase angle of the commercial Ag/AgCl-gel electrodes, tape-fixed Au nanofilm-SEBS electrodes, and PSA coated Au nanofilm-SEBS electrodes.

Another type of stretchable electrode is also compared. Au-PDMS electrodes are obtained by thermal evaporating Au nanofilm on the PDMS elastomer substrate. The Au-PDMS substrate is surface plasma treated and cut into a rectangular shape of 2 x 1 cm^2. One end of the electrode connects with copper wire and the other half is coated with PSA for skin contact. Two skin electrodes adhere to the skin with a separation of 2 cm. The two electrodes connect with the two terminals of the EIS system and impedance is measured from 1 Hz to 10^6 Hz. The Au-PDMS electrodes that are not PSA coated are fixed with medical tape on the skin. Commercial Ag/AgCl-gel electrodes are used as a control. The Au-PDMS electrodes show similar results as that of Au-SEBS (Figure 6.3a). Commercial electrodes record the smallest impedance value due to their electrolyte gel layer that greatly improves skin-contacting. Medical tape-fixed Au-PDMS electrodes show slightly smaller impedance than PSA-coated Au-PDMS electrodes. Similarly, this is due to the coating of non-conductive PSA blocking some areas of the Au nanofilm surface. Such blocked areas reduce the effective area for skin signal transduction. However, such a PSA-blocked area is important in adhering the electrode on the skin, without the usage of medical tapes. The phase angle of the three-electrode groups also shows similar results as that of impedance (Figure 6.3b).

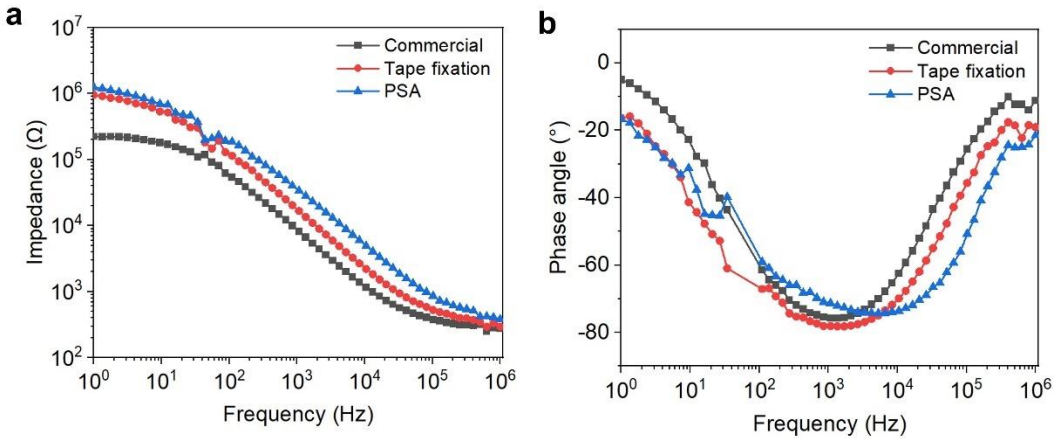

Figure 6.3 Impedance measurement of Au nanofilm-PDMS electrodes on the skin. (a) The Bode plot of the commercial Ag/AgCl-gel electrodes, tape-fixed Au nanofilm-PDMS electrodes, and PSA coated Au nanofilm-PDMS electrodes. (b) The phase angle of the commercial Ag/AgCl-gel electrodes, tape-fixed Au nanofilm-PDMS electrodes, and PSA coated Au nanofilm-PDMS electrodes.

The PSA coating on electrodes that are not intrinsically adhesive is important in realizing electrode conformability on the skin. The PSA coated some area of the electrode at the microscale. These areas serve as the adhesive anchoring points to bond skin and the electrode (Au nanofilm) in this case. To investigate the effects of PSA on the adhesiveness of the skin electrodes. Different amounts of the PSA are coated on the non-adhesive electrodes, Au-SEBS. To control the amount of the PSA on the electrodes, different layers of PSA are coated. The adhesiveness of the PSA-coated electrodes is measured using a mechanical tester. The electrodes are plasma-treated and cut into a rectangular shape of 4 cm x 0.5 cm. One-half of the electrodes adhere to the skin and the other end is clipped by the mechanical tester. The mechanical tester peels the electrode off from the skin at a constant strain rate of 0.5 mm s^{-1}. The force is measured, and the adhesive strength is obtained by dividing the force by the electrode width. The Au-SEBS electrodes coated with one layer PSA record an adhesive strength plateau of 1.1 N m^{-1}, while the electrodes coated with three-layer PSA show an adhesive strength plateau of 7.4 N m^{-1} (Figure 6.4). This adhesiveness would give a comfortable adhesion on the skin, and it can be modulated by adjusting the PSA coating layers.

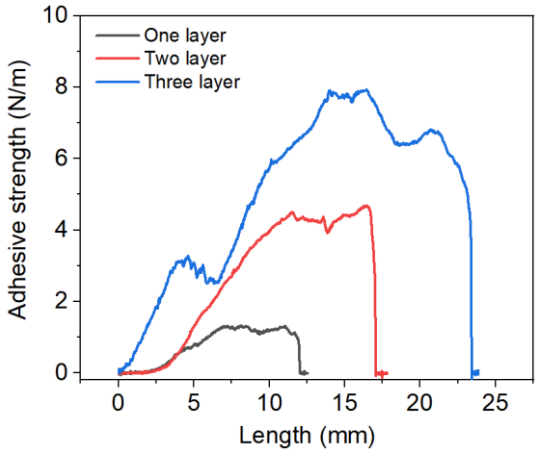

Figure 6.4 Adhesive strength measurement of PSA-coated Au nanofilm-SEBS electrodes on human skin. The adhesiveness can be controlled by coating different layers of PSA.

With the investigated conductive and adhesive properties, the PSA-coated electrodes can be used to measure biopotential signals. To make the whole device fully wearable, a miniaturized and wireless PCB is designed and fabricated. The flexible PCB board is based on an instrumentation amplifier (AD623, Analog Devices) to acquire and amplify the biopotential signals. The instrumentation amplifier is used because it has high common-mode rejection ratios and adjustable gain to amplify the signals. The output of the instrumentation amplifier is connected to the analog input terminal of an SoC (System on Chip, NRF52832). This SoC is a microcontroller with ADC and Bluetooth for data transmission. The analog signal in this terminal is further converted to a digital signal and transmitted to a computer or smartphone through Bluetooth. To integrate such flexible PCB with the PSA-coated electrodes for on-skin biopotential signal measurement (Figure 6.5). The electrode is firstly treated with plasma. Half of the electrode is coated with PSA for contact with skin. The other end of the electrode is coated with PSA for bonding the conductive pad on the flexible PCB. To fix the flexible PCB on the skin, the backing of the PCB is also coated with PSA. This PSA coating serves as a pure adhesive layer for PCB. With the PSA coating, all the bonding issues in conformal electrodes and flexible PCB can be resolved.

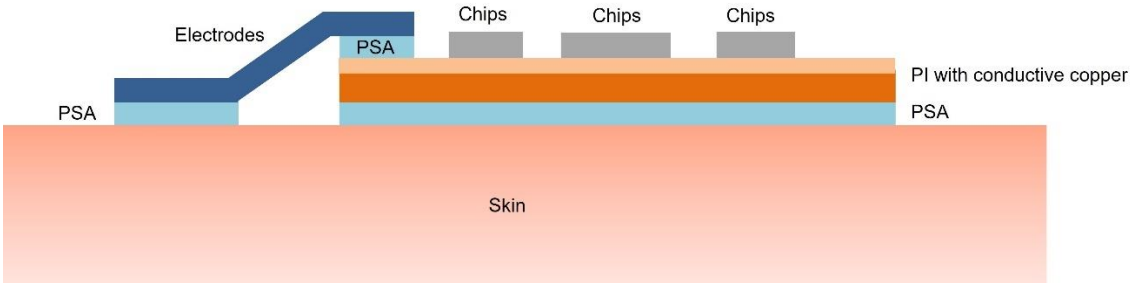

Figure 6.5 Schematic of applying PSA for adhering flexible PCB with human skin, bonding conformal electrodes with flexible PCB, and adhering the conformal electrodes with skin.

The flexible PCB with the conformal electrodes (PSA-coated Au-PDMS) can be integrated and wearable on the skin. The integrated devices can be attached to the chest to measure ECG or on arm to measure EMG (Figure 6.6a-b). The data is sent to another NRF52832 board which connects to a computer through serial communication. A Matlab program is

written to read and visualize the Bluetooth-transmitted data in real-time. It is shown that such a miniaturized wearable device can constantly measure ECG signals from a chest (Figure 6.6c). The ECG waveform as visualized in the Matlab window shows the proper functioning of the flexible PCB. The signals are acquired from the PSA-coated Au-PDMS electrodes. This indicates that the PSA-coated conformal electrodes can be integrated with wireless flexible devices for fully wearable biopotential signal measurement.

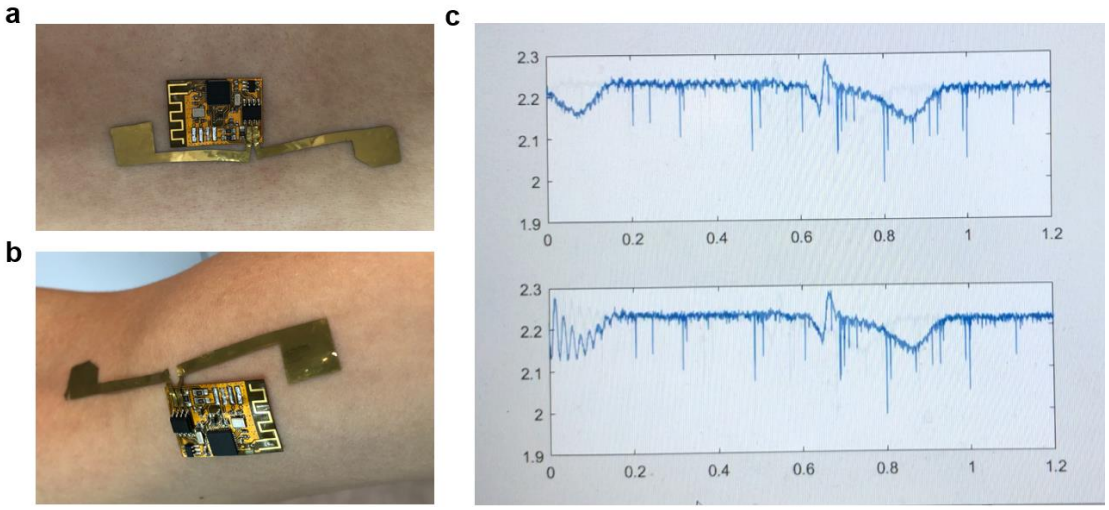

Figure 6.6 Application of the miniaturized and wireless flexible PCB to measure the biopotential signal from the skin. The flexible PCB can be adhered to on the chest to measure ECG and on arm to measure EMG.

With the PSA-coated conformal electrodes confirmed to accurately acquire biopotential signals from human skin, the electrodes are further used to provide comprehensive signals about 12-lead ECG. In the clinic application 12-lead ECG including 10 electrodes is used to measure 12 waveforms about the heart electrical activity, which can help doctors to diagnose many heart-related diseases such as arrhythmias, coronary disease, or electrolyte imbalance. The 12-lead ECG includes 6 chest leads (V1, V2, V3, V4, V5, and V6), and 6 limb leads (Lead I, Lead II, Lead III, aVR, aVL, aVF). The 6 limb leads are obtained from 4 electrodes, known as RA, LA, LL, and RL. Lead I, Lead II, and Lead III are measured by bipolar electrode pair (negative and positive electrodes). aVR, aVL, and aVF are unipolar and only need a positive electrode. For the unipolar leads, the reference for the

positive electrode is from an Einthoven's triangle (RA, LA, and LL). The 12-lead ECG is very helpful to measure using a clinical standard ECG machine, however, for personal wearable devices outside the hospital, it is difficult to implement such an instrument. Instead, a three-lead ECG measurement with different electrode placements is used to obtain similar 12-lead ECG waveforms. It should be noted that such 12-lead ECG measurement cannot be used for standard clinical analysis. It is an alternative to roughly estimate the 12-lead waveform for a purpose of convenience and when a standard medical instrument is not available. In the three-lead ECG measurement, there is an RLD electrode. This RLD electrode is an output electrode driven by an RLD amplifier. This lead senses the common-mode voltage from the other two input electrodes and drives an opposing voltage to the patient. This electrode eliminates the common-mode voltage in the inputs, greatly improving the CMRR. In the 12-lead ECG measurement using 3 electrodes, three types of conformal electrodes are used, including Au-PDMS, Au-SEBS, and AgNW-PDMS, to reflect the versatility of the PSA coating method. For each type of electrode, two methods are compared, the electrode is either coated with PSA to adhere to skin or fixed on skin with medical tape. All electrodes are used on the same person under the same condition. It is noted that both the PSA-coated electrodes and medical tape fixed electrodes can measure clear ECG waveforms with a similar signal-to-noise ratio (Figure 6.7-6.12). This agrees with the previous on-skin impedance measurement that the PSA-coated electrodes and medical tape fixed electrodes have a similar impedance. The 12-lead ECG waveforms were recorded using Au-PDMS electrodes (both PSA coated, or medical tape fixed), Au-SEBS electrodes (both PSA coated, or medical tape fixed), and AgNW-PDMS electrodes (both PSA coated, or medical tape fixed) are presented in Figure 6.7-6.12. The EMG signal measured from PSA-coated Au-PDMS electrodes, Au-SEBS electrodes, and AgNW-PDMS electrodes is presented in Figure 6.13. All the biopotential signals show clear signal traces, indicating that the PSA electrode coating technique is a robust, effective, and universal method for conformal electrodes.

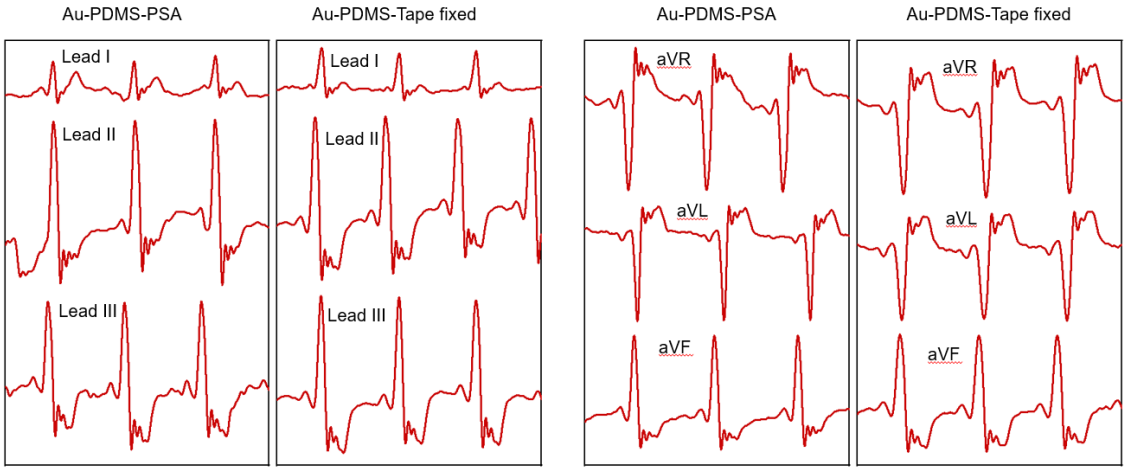

Figure 6.7 12-lead ECG (Lead I, Lead II, Lead III, aVR, aVL, aVF) signal measured from Au-PDMS coated with PSA compared with medical tape fixation.

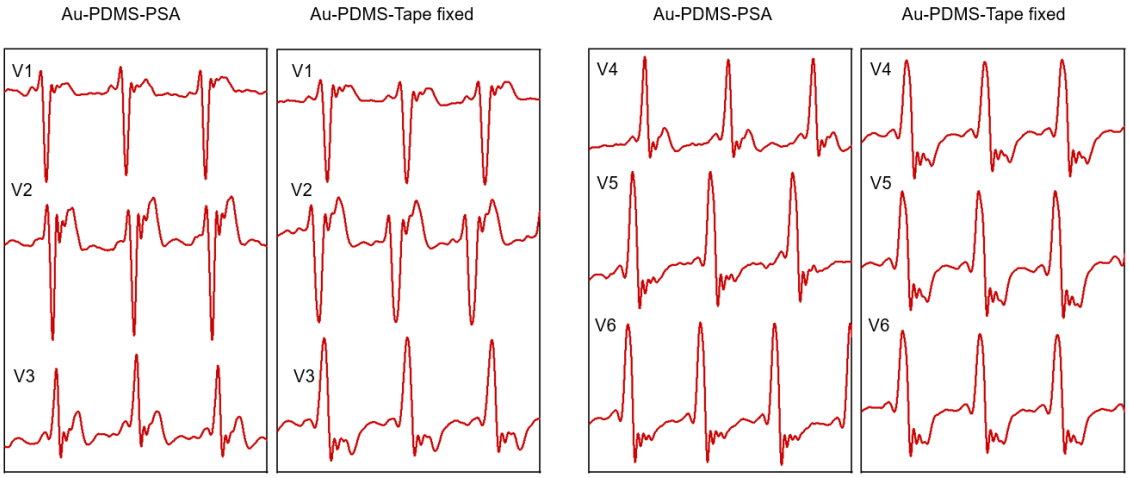

Figure 6.8 12-lead ECG (V1 – V6) signal measured from Au-PDMS coated with PSA compared with medical tape fixation.

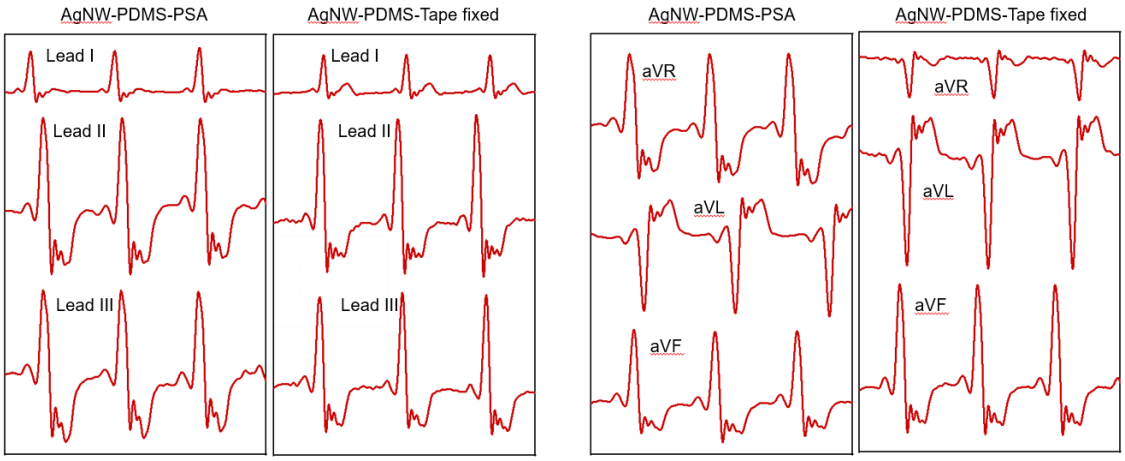

Figure 6.9 12-lead ECG (Lead I, Lead II, Lead III, aVR, aVL, aVF) signal measured from AgNW-PDMS coated with PSA compared with medical tape fixation.

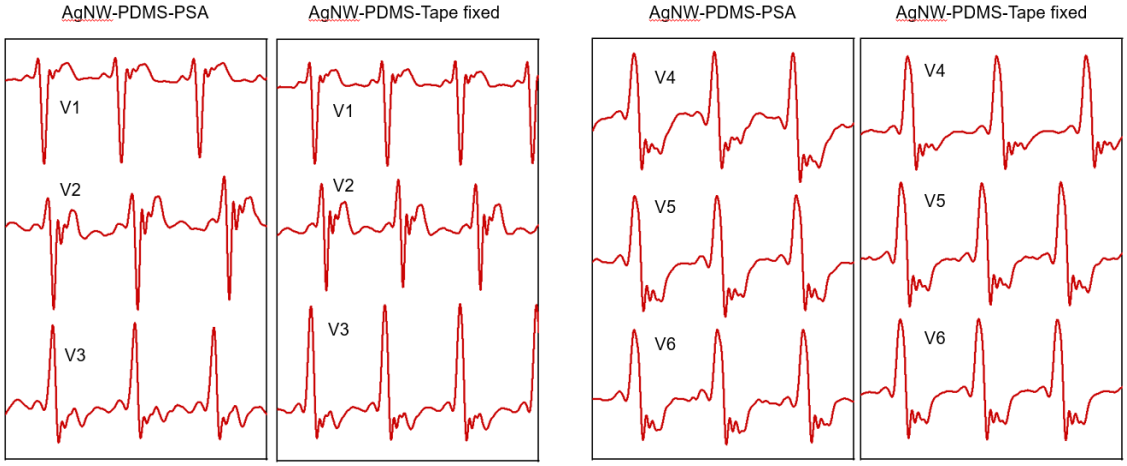

Figure 6.10 12-lead ECG (V1 – V6) signal measured from AgNW-PDMS coated with PSA compared with medical tape fixation.

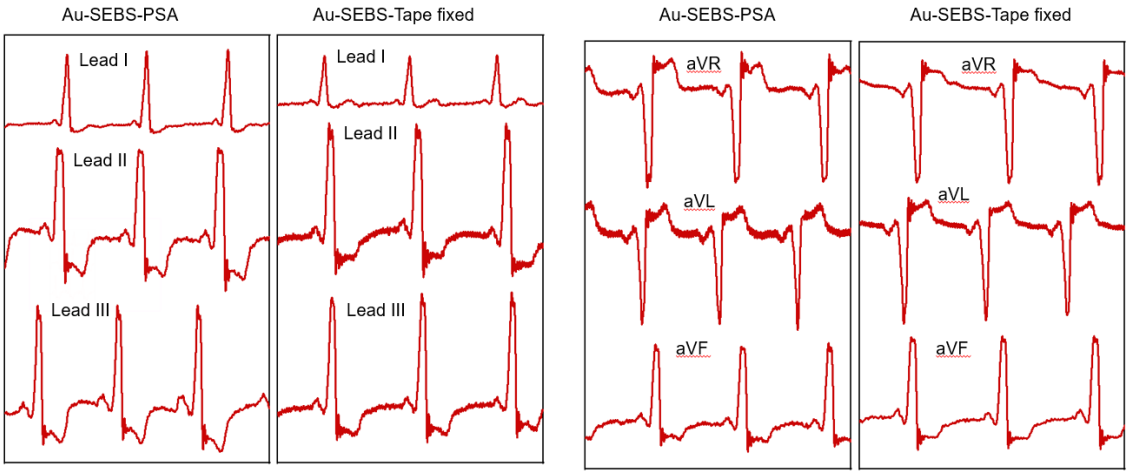

Figure 6.11 12-lead ECG (Lead I, Lead II, Lead III, aVR, aVL, aVF) signal measured from Au-SEBS coated with PSA compared with medical tape fixation.

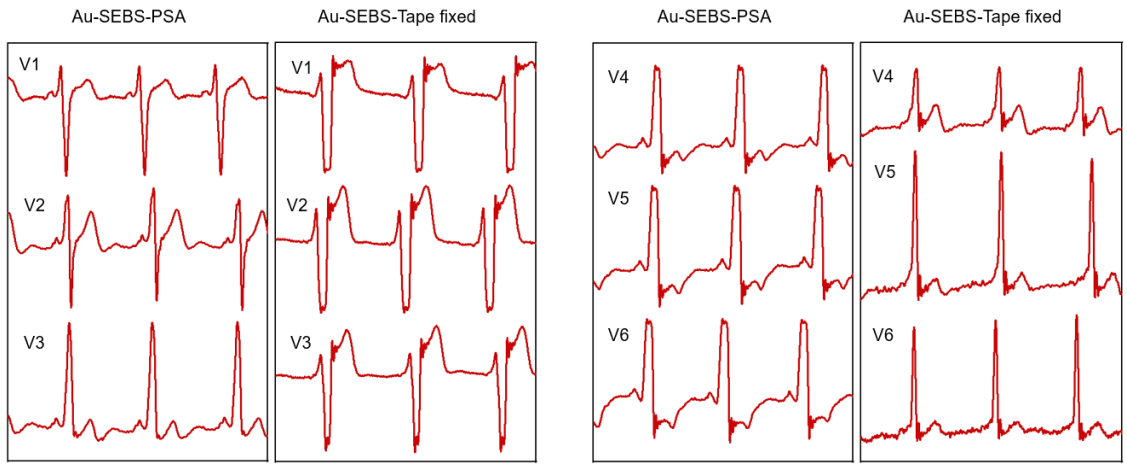

Figure 6.12 12-lead ECG (V1 – V6) signal measured from Au-SEBS coated with PSA compared with medical tape fixation.

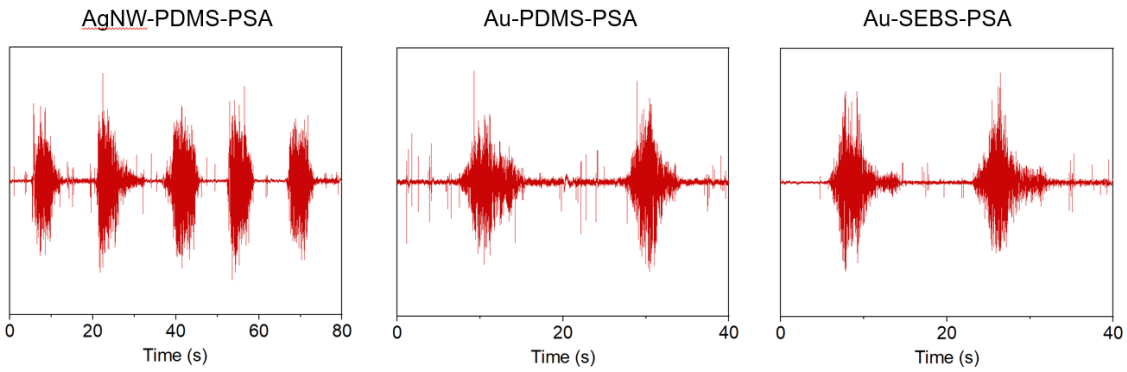

Figure 6.13 EMG signals measured from three-electrode (AgNW-PDMS, Au-PDMS, and Au-SEBS) coated by PSA.

References

[1] J. Kim, J. Park, U. Jeong, J.-W. Park, Journal of Applied Polymer Science 2016, 133.

[2] M. Ramuz, B. C.-K. Tee, J. B.-H. Tok, Z. Bao, Advanced Materials 2012, 24, 3223.

[3] Z. Liu, H. Wang, P. Huang, J. Huang, Y. Zhang, Y. Wang, M. Yu, S. Chen, D. Qi, T. Wang, Y. Jiang, G. Chen, G. Hu, W. Li, J. Yu, Y. Luo, X. J. Loh, B. Liedberg, G. Li, X. Chen, Advanced Materials 2019, 31, 1901360.

[4] N. Matsuhisa, X. Chen, Z. Bao, T. Someya, Chemical Society Reviews 2019, 48, 2946.

[5] R. R. Kisannagar, P. Jha, A. Navalkar, S. K. Maji, D. Gupta, ACS Omega 2020, 5, 10260; B. Liu, Z. Luo, W. Zhang, Q. Tu, X. Jin, Sensors and Actuators A: Physical 2016, 247, 459; A. C. Myers, H. Huang, Y. Zhu, RSC Advances 2015, 5, 11627.

[6] N. P. Shetti, A. Mishra, S. Basu, R. J. Mascarenhas, R. R. Kakarla, T. M. Aminabhavi, ACS Biomaterials Science & Engineering 2020, 6, 1823; H. Jung, J. Moon, D. Baek, J. Lee, Y. Choi, J. Hong, S. Lee, IEEE Transactions on Biomedical Engineering 2012, 59, 1472.

[7] S. K. Sinha, Y. Noh, N. Reljin, G. M. Treich, S. Hajeb-Mohammadalipour, Y. Guo, K. H. Chon, G. A. Sotzing, ACS Applied Materials & Interfaces 2017, 9, 37524; G. Li, Z. Qiu, Y. Wang, Y. Hong, Y. Wan, J. Zhang, J. Yang, Z. Wu, W. Hong, C. F. Guo, ACS Applied Materials & Interfaces 2019, 11, 10373; P. Zhao, R. Zhang, Y. Tong, X. Zhao, T. Zhang, Q. Tang, Y. Liu, ACS Applied Materials & Interfaces 2020, 12, 55083.

[8] M. D. Ho, Y. Liu, D. Dong, Y. Zhao, W. Cheng, Nano Letters 2018, 18, 3593.

[9] G. K. Menon, Advanced Drug Delivery Reviews 2002, 54, S3.

[10] Z. Liu, D. Qi, G. Hu, H. Wang, Y. Jiang, G. Chen, Y. Luo, X. J. Loh, B. Liedberg, X. Chen, Advanced Materials 2018, 30, 1704229.

[11] S. Fujii, S. Sawada, S. Nakayama, M. Kappl, K. Ueno, K. Shitajima, H. J. Butt, Y. Nakamura, Materials Horizons 2016, 3, 47.

Chapter 7

Conclusions and Recommendations

This chapter discusses the reflections on the results of the thesis. The hypotheses proposed at the beginning of the thesis are tested and reviewed. Implications of the work conducted in this thesis include the development of adhesive hydrogel materials with high mechanical, electrical, and antimicrobial properties as skin bioelectrode materials, as well as a versatile coating technique that endows non-adhesive stretchable electrodes with high conductivity and adhesiveness. Some reconnaissance studies which will be extended to the future will also be discussed. This includes a versatile bonding strategy to bond different stretchable conductors and a high-density electrode array for facial biopotential signal imaging. The design target is met, and the hypothesis is proved.

7.1 Discussion and conclusion

7.1.1 Testing hypotheses

The two hypotheses proposed previously include:

Hypothesis 1: Designing adhesive hydrogel with high electrical, mechanical, and antimicrobial can realize conformal on skin bioelectrodes for biopotential signal measurement.

Hypothesis 2: The adhesive coating of PSA on non-conductive stretchable electrodes can realize high conformability and high signal fidelity for biopotential signal measurement.

The hypotheses were proved in the experiments and results of this thesis. Firstly, adhesive hydrogel based on thermo-polymerization of PAA is developed and the optical transparency, ionic conductivity, stretchability, can be optimized by an ionic additive of KCl, making it a superior ionic conductor layer in contact with the skin. Secondly, ultrathin Au nanomesh is chemically synthesized and a transferring technique is explored to leverage the Au nanomesh on stretchable substrate working as an electronic conductor. Thirdly, antimicrobial hydrogel material for skin bioelectrode application is also synthesized through the co-assembly of silk fibroin and Fmoc-protected amino acids. Such material can make the contacting with skin bacteria-free and disrupt biofilm formation. Fourthly, a PSA coating technique is invented to solve the long-term adhesiveness issue of stretchable electrodes. The PSA coating allows non-adhesive stretchable electrodes partially coated with adhesive PSA anchoring point, with little effects on their conductivity but greatly increase their skin adhesiveness.

7.1.2 Major findings

The major findings of the thesis are summarized below:

1. An adhesive hydrogel system with optimized electrical and mechanical properties is achieved through a thermo-polymerization process. A surface functionalization method on PDMS elastomer substrate is explored to realize a strong bonding between the hydrogel and elastomer substrate. KCl is verified as the most effective ionic additive to realize high optical transparency, high ionic conductivity, high adhesiveness, and high stretchability. In addition, a stretchable Au nanomesh electronic conductor is chemically synthesized to transduce ionic current in hydrogel into the electronic current. This result shows that the synthesized adhesive hydrogel can effectively work as an electrolyte skin-contacting layer for the bioelectrodes application.

2. An antimicrobial hydrogel material is designed and fabricated with efficient gram-positive antimicrobial properties for on-skin electrode application. The hydrogel is made from the co-assembly of silk fibroin and Fmoc-protected amino acids. The assembled silk-based hydrogel is formed with very fast gelation kinetics (within two minutes). It shows promising killing efficiency against gram-positive B. subtilis. In addition, a tough, wearable, conformal, and antimicrobial hydrogel with silk fibroin and the chemical hydrogel is also presented. This result further enriches the adhesive hydrogel with an antimicrobial property that can keep the skin bacterial-free.

3. A universal and efficient adhesive coating technique is reported to comprehensively solve the adhesive issues related to most of the stretchable electrodes. The coating technique is based on PSA coating in an aqueous solution. It is independent of both stretchable conductive materials and stretchable substrate materials, making it compatible with most of the electrodes. The PSA coating works with an interesting mechanism in that the electrode surface is partially coated. The coated area works as the adhesive anchoring point to the skin, while the uncoated area works as a signal transduction pathway for measuring biopotential signals. This technique provides a facial and universal way for stretchable electrodes coating.

7.1.3 Implication of current work

The materials and devices described in this thesis have a materials innovation focus as well as scientific design. It aims to solve practical issues in skin bioelectrodes which is a widely used clinical application with materials strategy. The implication of work in this thesis includes:

1. It provides a comprehensive materials design strategy to realize desired application-oriented properties. To make this achievement, intensive materials design, characterization, and optimization are devoted to modulating the desired properties. Surface functionalization of elastomer substrate with acrylic acid monomers shows the synthesized hydrogel can maintain a strong bonding with the substrate. The chemically cross-linked hydrogel is further enriched with KCl ionic additive for improved ionic conductivity.

2. The adhesive PSA coating presents a novel and efficient solution to address the adhesive issue of most stretchable electrodes. The adhesive coating is realized by simply surface plasma treating the electrode surface and drop-casting the PSA solution. PSA would partially coat the surface of the electrode. The areas covered by PSA serve as the anchoring points for skin-electrode adhesion, while the areas uncovered by PSA are used for a biopotential signal pathway from the skin to the electrodes. Such a facile and efficient coating applies to a wide range of materials, including Au nanomesh, Au nanofilm, AgNW, CNT, conductive polymer, etc. for stretchable conductor materials, and PDMS, SEBS, ecoflex, etc. for stretchable substrate materials.

3. We have fabricated different skin-contacting materials for skin bioelectrode application. The acrylic-based material is mainly used for general purpose applications. It is easy to fabricate, highly adhesive, transparent, and the ionic conductivity can be tuned by different ionic additives. However, the acrylic-based hydrogel material is easy to dehydrate, limiting its application time. Another issue with the acrylic-based hydrogel is monomer leakage, which requires a washing process to clean the monomer residuals.

The most advantageous property of silk-based hydrogel is the antimicrobial property due to the co-assembly process with Fmoc-protected amino acids. The moisture environment from hydrogel may promote the growth of bacteria on the skin. The silk-based hydrogel can effectively prevent biofilm formation. The disadvantage of silk-based hydrogel is that Young's modulus is relatively large (> 1 MPa), rendering it not as soft as an acrylic-based hydrogel. In addition, the silk-based hydrogel also has the problem of dehydration under ambient conditions. The PSA-based material is an adhesive polymer matrix filled with conductive nanomaterials (MXene). It contains no water, so it has no dehydration issues. It is applicable for long-term uses. Its adhesive strength and conductivity can be tuned by the adhesive matrix and Mxene ratio. The disadvantage is that Young's modulus of the PSA-based material depends on the PDMS substrate (around 3 MPa). Other stretchable substrates with lower Young's modulus can be used to replace PDMS.

7.2 Future work

7.2.1 Adhesive bonding for different stretchable conductors

The PSA coating of electrodes presents a powerful yet facile way to solve the adhesion issue of most stretchable electrodes with skin. Such a novel technique can be extended to solve other bonding issues in stretchable electronics. The stretchable conductors, as mentioned earlier, are usually not adhesive, however, in many circumstances, there is a need to connect different stretchable conductors. This presents a real challenge as the stretchable conductors are not adhesive to each other. The current strategy is to use anisotropic adhesive tape to join the two conductors together. However, this method is restricted by the lack of pattern ability of the joining area and the weak bonding at the joining site. The PSA coating, when drop-casted on a plasma-treated surface, can form a thin film with some areas covered by the PSA adhesive and some other areas not covered. Apart from skin electrodes, this mechanism can also be applied to realize bonding between two stretchable conductors.

In the bonding of two stretchable conductors using PSA coating, Au nanofilm on PDMS substrate is used as a model stretchable conductor. The Au-PDMS film is firstly treated with plasma to increase its hydrophilicity. PSA is coated on the Au-PDMS using a drop-casting method, the amount of PSA is controlled to make sure the coating is thin and only wet the Au-PDMS surface. After the PSA aqueous solution is fully evaporated, another Au-PDMS film is flipped and adhered to the top of the PSA-coated area. The two Au-PDMS films are connected. The connecting area is pressed to ensure strong bonding. The electrical conductivity of the Au-PDMS stretchable film after bonding is verified using a multimeter (Figure 7.1a). Two ends of the bonded film connect with the multimeter probes. The bonded film is stretched while the resistance is recorded. The electrical connection keeps stable until 100% strain (Figure 7.1b). The increase in resistance is mostly due to the stretching of the film itself. The bonded area shows the minimal strain. This result indicates that the PSA coating is also an effective way to bond different stretchable conductors. It can be used to replace the currently used anisotropic conductive film.

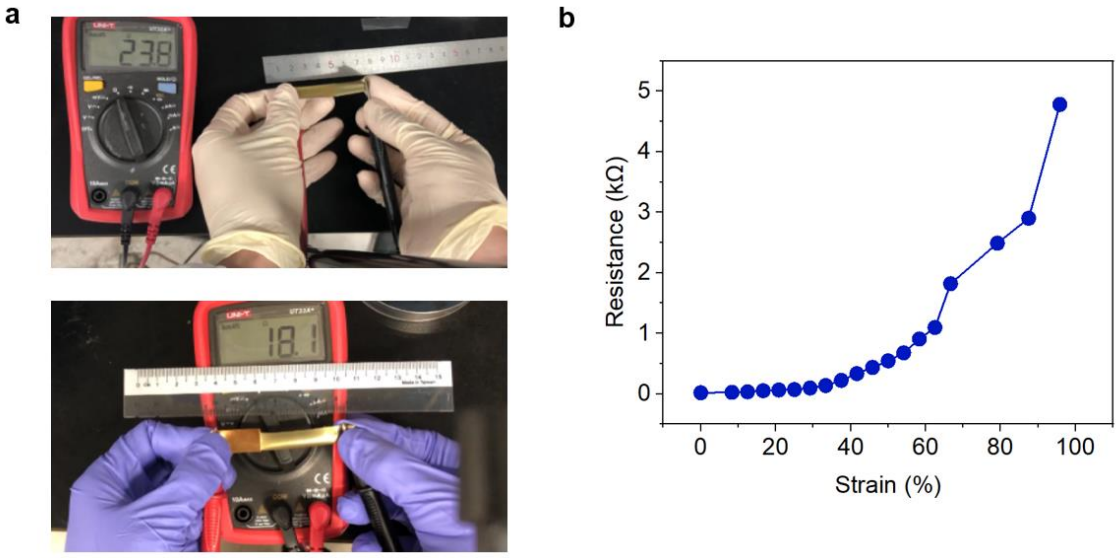

Figure 7.1 The electrical connection of two stretchable Au-PDMS conductors bonded by PSA. (a) Photograph of the bonded Au-PDMS conductor film being stretched. (b) The stretchability curve of the bonded Au-PDMS stretchable conductor.

To investigate the mechanism of the strong bonding and conductivity between two stretchable films bonded by PSA. A cross-sectional SEM image is obtained to look at the bonding area (Figure 7.2). From the low magnification SEM image, the two Au-PDMS films show an intact bonding interface. This indicates that the bonding interface is very uniform and thin. To further understand the bonding interface, high magnification SEM shows that the interface can be classified as a bonding and voids part and Ohmic contacting part. For the bonding and void part, there is oval free space partially filled with PSA bonding materials that connect the two films. For the Ohmic contacting part, the interface is very continuous, and the interface line is even hard to distinguish, indicating that the two Au films are firmly connected. The bonding and void part is important to anchoring two films together, even resisting stretching. This Ohmic contacting part is very important in ensuring the conductivity connection of the two films. During stretching, the adhesive anchoring points fix the connecting area, minimizing the strain generated at the area, while the Ohmic contacting points works as an electronic conduction pathway between the two films. Such a mechanism contributes to the high stretchability of the bonded film.

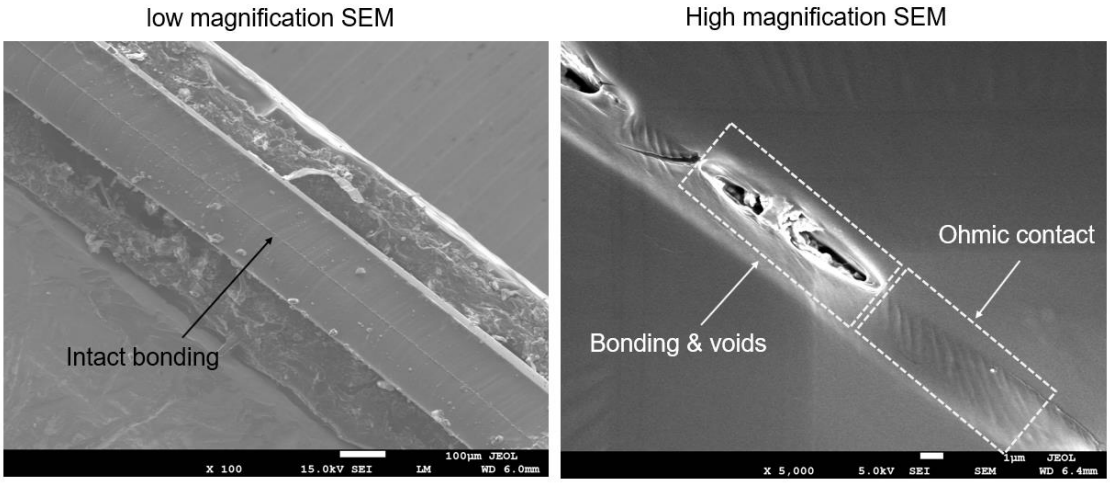

Figure 7.2 SEM image investigation of the cross-sectional contact between two Au-PDMS stretchable conductors. The low magnification image shows intact bonding between the two films. The high magnification image shows the bonding site and Ohmic contacting site. The binding site is useful for connecting two films while the Ohmic contact ensures conductivity.

The novel and facile bonding techniques based on PSA coating are meaningful to solve the difficult bonding issues between different stretchable conductors. It is also efficient to bond

stretchable conductors and non-stretchable conductors together (Figure 7.3). In the application of stretchable electronics, the sensor part in direct contact with the skin is usually made with stretchable and low Young's modulus materials, this is to ensure the signals can be measured accurately from the skin. The data acquisition part is usually made from rigid or flexible PCB, which is not stretchable. In the application, there is usually a need to connect the stretchable sensor part with the non-stretchable PCB part, and electrical conductivity is needed after the connection. A conventionally anisotropic conductive film is needed for such bonding. With the advanced technique presented here based on PSA coating, such bonding can be easily realized using the PSA technique. The connection part of the stretchable needs to be plasma treated and coated with a thin layer of PSA. Then the connection part of the stretchable sensor adheres to the connection part of the PCB. By pressing the connection part to ensure the adhesion of PSA, conductive bonding between the two connection parts is established.

Figure 7.3 Photograph of the PSA bonding between an Au-PDMS conductive film and an FFC (flexible flat cable), showing strong bonding between the two connectors.

7.2.2 High-density electrode array for facial biopotential imaging

The on-skin biopotential electrodes developed previously in this thesis are only one measuring point for each electrode. That is, to measure three points, three electrodes need to be made and attached to the skin. For the biopotential characterization of the human body, there is usually a need to give spatial-temporal information about the electrical activity[1]. In this case, multiple electrodes are needed. To measure electrical information

at a high spatial resolution, a high-density electrode array is needed for multichannel measurement[2].

The human face has rich bioelectrical information. The forehead has EEG signals which reflect the brain's electricity activity[3], the area around the eyes has rich EOG signals which are generated by the eyeball movement[4]. The cheek area has rich EMG signals which are generated from the muscle contraction during speaking or chewing[5]. The measurement of such information would provide vital information on human mental states and facial expressions. In addition, the signals obtained from the face can help realize the human-machine interface as many commands can be decoded from the facial signals. As such, the bioelectrical imaging of the human face is important.

To decipher human facial bioelectrical information, a multichannel high-density facial electrode array is fabricated, this array is made from patterned Au nanofilm on PDMS substrate. A metal mask is made from AutoCAD software. The metal mask is attached to the PDMS during thermo-evaporation of Au. An encapsulation layer is further covered on the electrode array to only allow electrode points to open. The electrode array can conformally adhere to the human face for continuous signal measurement. To realize the full wearability of the device, a customized PCB is designed and fabricated (Figure 7.4). This data acquisition PCB allows high rate and multichannel biopotential signal acquisition and wireless data transmission based on Bluetooth. The next version of the PCB would be made with the flexibility to allow wearability on the human head. This high-density face sensor array along with the wearable PCB will be further innovated in the future for bioelectrical imaging of the human face.

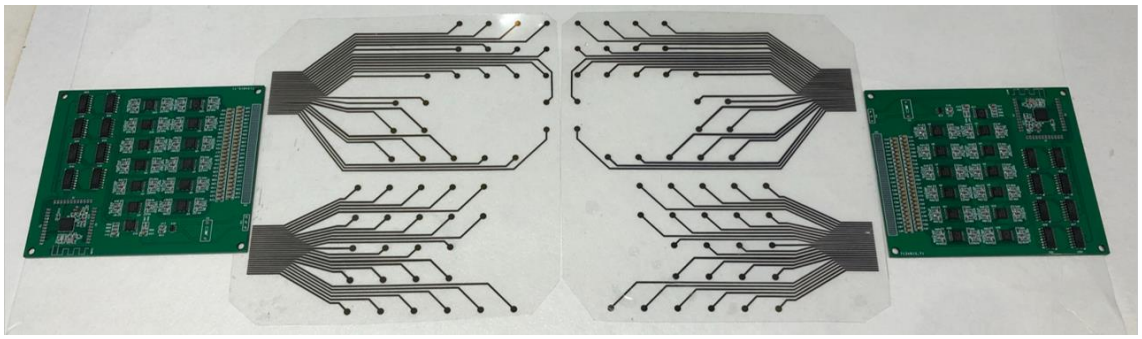

Figure 7.4 Photograph of a high-density electrode array based on Au nanofilm and PDMS with customized PCB for the multichannel biopotential signal measurement.

References

[1] J. Liu, X. Zhang, Y. Liu, M. Rodrigo, P. D. Loftus, J. Aparicio-Valenzuela, J. Zheng, T. Pong, K. J. Cyr, M. Babakhanian, J. Hasi, J. Li, Y. Jiang, C. J. Kenney, P. J. Wang, A. M. Lee, Z. Bao, Proceedings of the National Academy of Sciences 2020, 117, 14769; A. Vázquez-Guardado, Y. Yang, A. J. Bandodkar, J. A. Rogers, Nature Neuroscience 2020, 23, 1522; D.-H. Kim, J. Viventi, J. J. Amsden, J. Xiao, L. Vigeland, Y.-S. Kim, J. A. Blanco, B. Panilaitis, E. S. Frechette, D. Contreras, D. L. Kaplan, F. G. Omenetto, Y. Huang, K.-C. Hwang, M. R. Zakin, B. Litt, J. A. Rogers, Nature Materials 2010, 9, 511.

[2] W. Lee, T. Someya, Chemistry of Materials 2019, 31, 6347; H. Shim, K. Sim, F. Ershad, S. Jang, C. Yu, Journal of Materials Chemistry C 2020, 8, 10719.

[3] K. P. Gao, G. C. Shen, N. Zhao, C. P. Jiang, B. Yang, J. Q. Liu, IEEE Sensors Journal 2020, 20, 10393; G. Li, J. Wu, Y. Xia, Y. Wu, Y. Tian, J. Liu, D. Chen, Q. He, Journal of Neural Engineering 2020, 17, 026001.

[4] M. Merino, O. Rivera, I. Gómez, A. Molina, E. Dorronzoro, "A Method of EOG Signal Processing to Detect the Direction of Eye Movements", presented at *2010 First International Conference on Sensor Device Technologies and Applications*, 18-25 July 2010, 2010; S. Yathunanthan, L. U. R. Chandrasena, A. Umakanthan, V. Vasuki, S. R. Munasinghe, "Controlling a Wheelchair by Use of EOG Signal", presented at *2008 4th International Conference on Information and Automation for Sustainability*, 12-14 Dec. 2008, 2008; H. Harun, W. Mansor, "EOG signal detection for home appliances activation", presented at *2009 5th International Colloquium on Signal Processing & Its Applications*, 6-8 March 2009, 2009.

[5] L. Fraiwan, K. Lweesy, A. Al-Nemrawi, S. Addabass, R. Saifan, Medical & Biological Engineering & Computing 2011, 49, 811; A. Gruebler, K. Suzuki, IEEE Transactions on Affective Computing 2014, 5, 227.